technische universität dortmund

Universitätsmedizin Essen
Westdeutsches Protonentherapiezentrum (WPE)

Arbeit zur Erlangung des akademischen Grades eines Doktors der Naturwissenschaften der Fakultät Physik der Technischen Universität Dortmund

Nuclear Physics in Proton Therapy: New Approaches for Proton Beam Range Verification using delayed Gamma-Rays

Claus Maximilian Bäcker
geboren in Dortmund

2022

Experimentelle Physik IV
Fakultät Physik
Technische Universität Dortmund
in Zusammenarbeit mit
Westdeutsches Protonentherapiezentrum Essen
Universitätsmedizin Essen

Von der Fakultät Physik zur Veröffentlichung angenommene Dissertation zur Erlangung des akademischen Grades eines Doktors der Naturwissenschaften (Doctor rerum naturalium).

Vorsitzender der Prüfungskomission:	Prof. Dr. Christoph Lange
Erstgutachter:	Prof. Dr. Kevin Kröninger
Zweitgutachter:	PD Dr. Christian Bäumer
Vertreter der Wissenschaftlichen Mitarbeiter:	Dr. Sergiu Anghel
Abgabedatum:	03. Januar 2022
Datum der mündlichen Prüfung:	27. April 2022

Teilpublikation Einige Ergebnisse dieser Arbeit sind Bestandteil bereits veröffentlichter Beiträge. Eine Übersicht dazu befindet sich in Anhang B.

Abstract

In-vivo monitoring of the delivered dose is desirable in radiation therapy. Radionuclides generated during the proton irradiation can be used for imaging methods from nuclear medicine after the treatment session. In order to improve these techniques, this work focuses on three different aspects of nuclear physics from basic nuclear physics measurements to a clinical validation. The most relevant nuclear interaction is the production of ^{11}C from carbon as this nuclear interaction is used as a monitor reaction for the measurement of several other radionuclides. Furthermore, this is one of the relevant residuals produced from the tissue nuclei. As the data from the literature scatter by about 15%, a new reference cross section value of (68 ± 3) mb at 97 MeV is determined from the cross sections measured in different settings. In a second part, the activation of iodine during proton irradiation is investigated. Several radionuclides are produced from iodine which decay by the emission of positrons and can potentially be used for PET imaging subsequent to the fractional treatment. In the last step, the activation of titanium implants is investigated. A benchmarking test including MC simulations is performed which study reveals the limited applicability of PET imaging with implants for field verification in proton therapy.

Kurzfassung

Die Überwachung der applizierten Dosisverteilung in der Strahlentherapie kann zur Optimierung der Therapie genutzt werden. Während der Protonenbestrahlung erzeugte Radionuklide können nach der Behandlungssitzung zur Bildgebung mit Methoden aus der Nuklearmedizin verwendet werden. Die vorliegende Arbeit untersucht drei verschiedene kernphysikalische Aspekte von der Untersuchung von Kernreaktionen hin zu einer klinischen Validierung, um diese Techniken zu verbessern. Zunächst wird die Produktion von ^{11}C aus Kohlenstoff untersucht, da diese Reaktion in der Kernphysik als Monitorreaktion verwendet wird. Die Literaturwerte der Wirkungsquerschnitte variieren um bis zu 15%. Außerdem stellt diese Reaktion eine wichtige Produktion von Radionukliden in menschlichem Gewebe dar. Als neuer Referenzwert kann (68 ± 3) mb bei einer Energie von 97 MeV bestimmt werden. In einem weiteren Schritt wird die Aktivierung von Iod untersucht. Da viele Positronenemitter bei der Bestrahlung von Iod produziert werden, kann die Aktivierung von Iod zur PET Bildgebung verwendet werden. Als letztes wird die Aktivierung von Titanimplantaten betrachtet. Dazu wird dazu ein Sensitivitätstest inklusive der Aktivitätsvorhersage durchgeführt, der die beschränkten Einsatzmöglichkeiten der PET Bildgebung zur Feldverifikation in der Protonentherapie aufzeigt.

Contents

1 Introduction and motivation

Proton and ion beam therapy has been developed at nuclear physics research centers in the 1950s as an alternative method of radiotherapy compared with so-called conventional radiotherapy with high energy photons or gamma-rays [1]. Since the first experimental therapy with protons, the number of patients increased nearly exponentially [2]. Radiation therapy makes use of the dose deposition of high energy particles in tissue which subsequently leads to irreversible deoxyribonucleic acid (DNA) damage by several physical, chemical, and biological processes. Proton therapy is considered to be superior compared to conventional radiation therapy because of the favorable depth dose distribution [3, 4].

In general, a limitation in radiation therapy is the control of the correct delivery of the fractional dose [5]. The therapeutic effect can be studied weeks and months after the treatment with additional imaging, but this method does not provide any direct information about the delivered dose distribution. With image guidance, anatomic changes in the patient geometry can be detected, and a re-planning process can be initiated, if medically indicated. However, this decision is based on treatment planning algorithms. These algorithms, calculated with the initial imaging or the additional ones during the treatment, are all affected by the same uncertainty between calculated and applied dose distribution. For proton therapy, the estimation of the stopping power from the X-ray computed tomography (CT) imaging dominates the uncertainty in the calculation of the proton beam range [6]. Due to the different types of interactions, an empiric model is used to estimate the stopping power from the X-ray attenuation. To account for the uncertainties, a safety margin is used to ensure the coverage of the complete target volume. However, in modern techniques of high-conformal radiotherapy an accurate delivery of the fractional dose is crucial for the therapeutic outcome [4, 5].

Proton beam therapy is superior compared to conventional photon therapy considering the potential of dose monitoring, because nuclear interactions can be used to monitor the dose delivery in-vivo. Two basic concepts have been developed in the past which utilize nuclear interactions in the tissue [3, 4]. The monitoring of prompt photon radiation up to 10 MeV from nuclear interactions in the patient's tissue during patient treatment, so-called on-line method [7], the latter one is based on imaging the produced activity after dose delivery is completed [8, 9]. In contrast

to diagnostic positron emission tomography (PET), the activity in the patient is a by-product from the treatment session and no radioactive drug is needed.

This work focuses on the physics for PET-based dose verification in proton therapy. The concept is to measure the proton induced β^+ activity distribution in the patient once a treatment session has been completed and to compare the measured activity distribution with a Monte-Carlo (MC) simulation of the expected distribution based on the treatment plan [3, 8]. It has been observed that the produced activity distributions are disturbed by several biological transport processes, like blood flow, metabolism, and diffusion, which are commonly referred to as biological wash-out [8]. To avoid the disturbance, the PET scan has to be performed in a timely manner, which requires a PET system in the treatment room for the clinical practice. As clinical PET systems are mainly implemented as hybrid imaging systems with an CT scanner, these systems cannot be moved between different treatment rooms because of their size. For multi-room proton therapy centers, the imaging systems have to be installed in a dedicated room. In consequence, a solution has to be implemented to avoid the disturbance by the biological wash-out. Therefore, implanted markers have been suggested as one possible solution in the literature [10–13]. The different measurements for this work combine basic and applied nuclear physics investigations on the improvement of the post-fractional PET imaging.

After a brief introduction in the physics and techniques of proton therapy in Chapter 2 and the low-level gamma-ray spectrometry in Chapter 3, several aspects of nuclear physics for proton beam field verification are discussed in this work. In Chapter 4, the $^{\text{nat}}\text{C(p,x)}^{11}\text{C}$ activation cross section is discussed in detail. On the one hand, carbon is one of the most relevant nuclides in biological molecules, on the other hand, several other cross sections have been measured relative to this cross section. However, two distinct trends of the $^{\text{nat}}\text{C(p,x)}^{11}\text{C}$ excitation function have been measured over the last 70 years. These two trends of cross sections are roughly 15% apart and the difference persists in the most recent publications. To achieve clinically needed accuracy, the activation of carbon is reviewed as one part of the presented studies. In a second part, the activation of caesium iodine (CsI) is discussed in Chapter 5. Iodine is a contrast agent for several applications in medicine and many positron emitters are produced from iodine during proton bombardment. The possible application of the activation of iodine in proton therapy is investigated in this work. The last step is the activation of titanium implants in proton therapy. Markers or surgical implants made of titanium are not subject to transport processes in the human tissue. Thus, the biological wash-out can be avoided by using implants for proton beam field verification, as it has already been proposed in the literature. In Chapter 6, the clinical application of the activation of titanium implants and PET imaging is investigated further. The results and their impact on clinical application in proton therapy are summarized in Chapter 7.

2 Physics and techniques in proton therapy

2.1 Interaction of protons with matter

2.1.1 Physics processes

The interaction processes of protons with matter can be separated in different types, electromagnetic interactions with the electrons or nuclei and nuclear reactions [14, 15]. The first one is the interaction of protons with the electrons in the target atoms. The latter ones are interactions with the target nuclei. The excitation processes dominate the overall energy depositions and contribute to the majority of the dose deposition. In general, the averaged energy deposition per path length and density $\frac{1}{\rho}\frac{\mathrm{d}E}{\mathrm{d}x}$ is described by the Bethe–Bloch-equation

$$-\frac{1}{\rho}\frac{\mathrm{d}E}{\mathrm{d}x} = \frac{\mathrm{e}^4 \mathrm{N_A}}{4\pi\epsilon_0^2 \mathrm{m_e} {\mathrm{c_0}}^2}\frac{Z}{A}\frac{1}{\beta^2}\left(\ln\left(\frac{2\mathrm{m_e}\gamma^2\beta^2}{{\mathrm{c_0}}^2 I}\right) - \beta^2 - \frac{\delta(\beta\gamma)}{2} - \frac{C(\beta\gamma, I)}{Z}\right), \quad (2.1)$$

with the natural constants: the electron mass $\mathrm{m_e}$, the velocity of light $\mathrm{c_0}$, the elementary charge e, the vacuum permittivity ϵ_0, and Avogadro's constant $\mathrm{N_A}$; the material parameters: the mean excitation energy I of the target material, the atomic number Z, and the mass number A; and the relativistic parameters $\beta = {}^{v}/_{\mathrm{c_0}}$ and $\gamma = {}^{1}/_{\sqrt{(1-\beta^2)}}$. The two corrections ${}^{\delta(\beta\gamma)}/_{2}$, density correction, and ${}^{C(\beta\gamma, I)}/_{Z}$, shell correction, are empiric corrections depending on the particle energy and mean excitation energy. More general, the Bethe–Bloch-equation is valid for energy deposited in matter by heavy charged particles [16–18]. The resulting energy loss is displayed in Figure 2.1. The kinetic energy of therapeutic used protons is up to about 250 MeV which corresponds to $\beta\gamma < 0.6$. In this energy domain, the energy loss is proportional to ${}^{1}/_{\beta^2}$. This characteristic leads to the depth dose distribution with a sharp peak close to end of range of the proton beam, which is commonly known as Bragg peak [3]. The advantages of the special dose distribution compared to radiotherapy with photons are discussed in the Chapters 2.1.2 and 2.2.2 respectively, where a depth dose curve is shown.

In proton therapy, the energy of the proton beam is not used to characterize the proton beam as it is the exact energy of the proton beam is not easily measurable. Therefore, in clinical context, the proton beams are characterized by the depth in

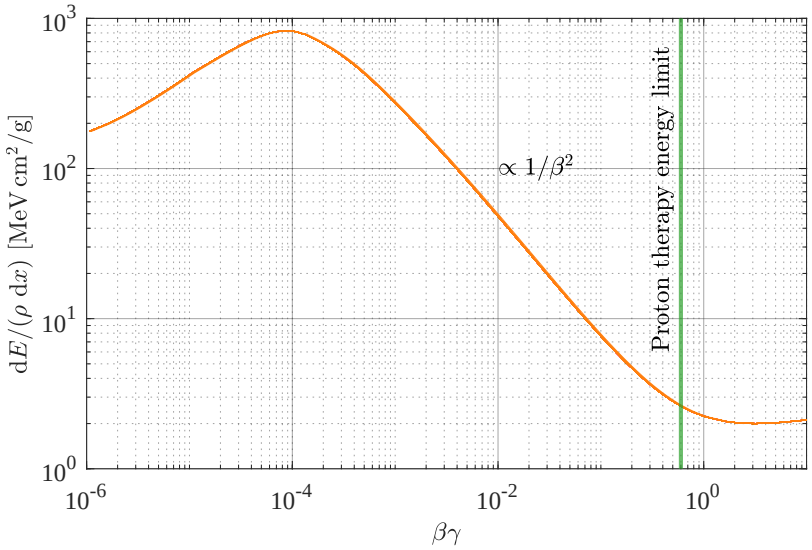

Figure 2.1: Energy loss of energy protons in matter. The relevant energy range for proton therapy is $\beta\gamma < 0.6$ (green line). The energy loss is proportional to $1/\beta^2$ in this energy range. The data are taken from [19].

water where depth dose curve has dropped to 80% of maximal deposited dose. This is known as the range of the proton beam called R80. This depth is associated with the point, where the proton fluence has dropped to approximately 50% of the initial fluence.

Albeit small impact on dose deposition, nuclear reactions contribute to the energy loss of high energy protons. These nuclear reactions can be grouped in different categories, like nuclear fusion, nuclear excitation and nuclear fission. The latter processes will be discussed further during the presented studies, especially those, which produce radioactive residual nuclei. These nuclear fission leads to radioactivity produced in the patient during the therapy. This radioactivity can subsequently be used for treatment field verification [8, 20].

In order to quantify the energy dependent interaction probability for each interaction process, the cross section σ can be introduced and calculated with the formula

$$\sigma = \frac{M_T F_{\mathrm{sample}} N_{\mathrm{reaction}}}{\mathrm{N_A} m_{\mathrm{sample}} N_{\mathrm{proton}}}, \tag{2.2}$$

which can be derived from the quotient of the initial protons, interacted protons, initial target nuclei, and converted nuclei. In conclusion, the cross section is

calculated with the area of the sample F_{sample}, its mass m_{sample} and molar mass M_T, the number of reactions N_{reaction}, and the number of incident protons N_{proton}. The common scale of cross sections for reactions discussed in the presented study is $1\,\text{mb} = 1 \times 10^{-27}\,\text{cm}$. The cross section can be visualized as a virtual target area of the nuclei. However, it does not correspond to any physical size of the atoms. To summarize multiple interactions, it is possible to sum up cross sections for different reactions.

For completeness, the elastic scattering induced by the Coulomb field of the target nuclei should be mentioned. As the protons can be deflected from their initial path by several Coulomb interactions, this is also known as multiple Coulomb scattering. As a result of the several scattering interactions, the path length of the proton is longer than the range projected on the initial beam path and the lateral beam shape increases with depth in a target.

All the interactions are statistical processes. Since several 1×10^9 protons are delivered in a single proton field, the initial sharp energy distribution becomes a wider spectrum with target depth which is called energy straggling. Furthermore, the multiple scattering processes lead to a lateral broadened beam width.

2.1.2 Biological effectiveness

To determine the applied radiation dose, the absorbed dose D

$$D = \frac{\mathrm{d}E}{\mathrm{d}m} \tag{2.3}$$

which describes the deposited energy $\mathrm{d}E$ per mass $\mathrm{d}m$ is used. The energy dose is called physical dose in the context of proton therapy as well to separate from the therapeutic effective dose.

Compared to photon irradiation, proton irradiation has a higher biological effectiveness of the radiation. In the several studies in the literature, proton irradiation results on average in a 10% larger biological damage compared to conventional photon irradiation with the same physical dose [21, 22]. Therefore, the relative biological effectiveness (RBE) is introduced to compare the different treatment techniques in radiation therapy. In detail, this effect is still under investigation and the exact value of the relative biological effectiveness varies between 0.9 and 2.1 along the different studies [6, 21, 22]. Current clinical studies point out, that value of 1.1 is the best estimate of the RBE. All present studies point out, that there might be an increase of the biological effects to the end of the proton beam range and that this corresponds to the increasing energy deposition per unit of length

along the path of the particle which is called linear energy transfer (LET). However, the exact modeling is still not clear.

To separate the biological dose and the physical dose, the biological effective dose is measured in the unit of 1 Gy(RBE) [6]. Treatment fields planned with a clinical treatment planning system (TPS) are given in 1 Gy(RBE) in this thesis. Several further definitions of the dose can be used for example in radiation protection. The dose is prescribed by a physician in radiation therapy and assigned to a specified target volume [6]. The dose absorbed in water is the commonly used objective in radiation therapy as it is the common method to measure the applied dose [23].

2.2 Techniques in proton therapy

2.2.1 Accelerators for proton therapy

Two different concepts of accelerators have been introduced over the years in ion beam therapy [14]. However, these basic concepts have been developed further, and the several treatment machines differ in the technical implementation. Only the basic concepts are summarized in this chapter and the implementation at the West German Proton Therapy Centre Essen (WPE) is discussed in detail.

One method is the setup of a linear accelerator with a synchrotron. The protons are pre-accelerated in the linear accelerator and transferred into the synchrotron, a circular beam line with controllable magnets. To reach proton energies for patient treatment, the protons are accelerated further in the synchrotron. Therefore, a radio-frequency (RF) unit is placed in the beam line and the magnetic field of the beam line has to be adjusted. As a consequence, it is necessary to start with a new acceleration process, if the beam energy needs to be changed. Furthermore, the diameter of a synchrotron for proton therapy is more than 5 m and the synchrotron requires more space compared to a cyclotron. The advantage of synchrotron-based treatment systems is the possibility to change the particle type. As a result, the system is not limited to one particle type like protons. C, He or other ions can be accelerated by the system. Only different linear accelerators are necessary and can be installed at the same synchrotron. This provides more treatment options.

Isochronous cyclotrons are more compact with diameter of less than 10 m for the therapeutic used proton beams. The protons are injected in the center of the cyclotron. An alternating electric field between two electrodes, so-called Dees, accelerates the particles in the cyclotron. With 180° turns, enforced by a magnetic field perpendicular to the beam plane, the particles describe a spiral-like trajectory through the cyclotron. The alternating electric field has a fixed frequency of

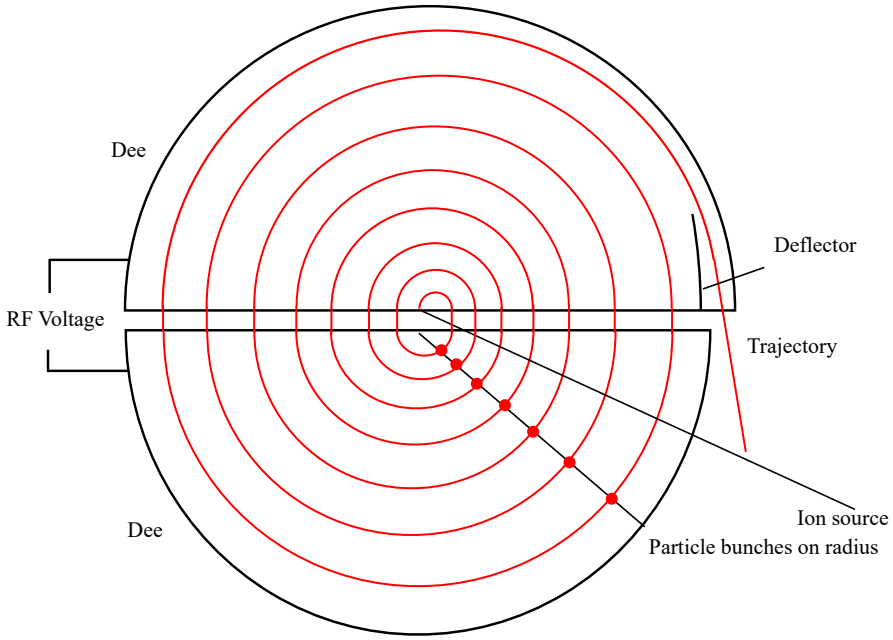

Figure 2.2: General setup of a cyclotron to accelerate proton beams. The magnetic field in the cyclotron would face into the drawing layer. Image adapted from [24].

several 10 MHz up to 100 MHz, which depends on the treatment machine, and a power of several 10 kW. After a defined number of rounds in the cyclotron, associated with the defined energy, the beam is extracted from the cyclotron with an additional electromagnetic field. A schematic drawing of a cyclotron is shown in Figure 2.2 [14].

For energy ranges of therapeutic energies up to 250 MeV, the constructions of cyclotrons have to consider relativistic effects. In isochronous cyclotrons, the magnetic field is increased to the outside of the cyclotron by concave surface of the insides of the Dees. This results in de-focusing of the beam in the cyclotron. Additional edges in the surface of the Dees are used to focus the beam again.

As a cyclotron has a fixed energy of about 250 MeV, which is the maximum energy for clinical patient treatment, the energy has to be reduced for tumors with shallow depth. Therefore, a wedge is inserted in the beam line to reduce the beam energy down to energies of about 60 MeV. Each position of the wedge is associated with a dedicated energy, defined by the residual range in water of the proton beam. An energy filter system with a magnetic field and a slit collimator reduces the energy

spread of the beam enlarged by the wedge. This system is called degrader. Compared to a synchrotron, the change of the beam energy is faster as not a complete new acceleration process needs to be initiated

2.2.2 Proton beam delivery modes

The physics of proton interactions with matter result in the depth dose distribution shown in Figure 2.3 for a mono-energetic proton beam. This depth dose curve is commonly known as Bragg peak curve. The advantage compared to photon beams which deliver a depth dose distribution described mainly with an exponential fit, is the sharp distal fall-off and low entrance dose. To treat clinical extended volumes, multiple Bragg peak curves have to be superposed, to achieve a high dose plateau at the distal end of the depth dose distribution which is known as a spread-out Bragg peak (SOBP).

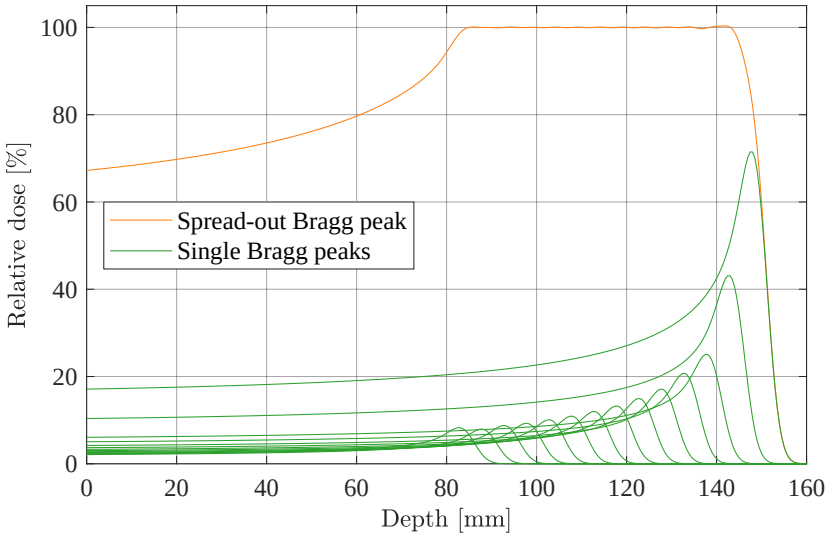

Figure 2.3: Depth dose curve of a SOBP (orange) delivered by the superposition of several quasi-monoenergetic proton beams (green) with decreasing energy and weights. The script to create the figure is based on [25].

Different treatment modes are used in clinical practice to deliver proton fields. In general, these modes are divided in passive scattering and active scanning. One of the passive modes is the so-called double scattering (DS). The proton field is broadened by scatter foils up to several 10 cm diameter. A second scatterer in the

beam flattens the lateral dose distribution. The lateral irregular shape of the target volume is formed by a patient specific aperture made of brass. The beam energy is chosen depending on the depth of the distal end of the target volume. To form a conformal field at the distal end, a patient specific polymethyl methacrylate (PMMA) compensator is mounted downstream of the aperture. Thus, the irregular depth of the distal end of the target can be irradiated with the same energy. A homogenous dose distribution is achieved with a modulator wheel with increasing thickness, which is spinning with some 100 rotations per minute and each depth is irradiated several times. In result, the dose is delivered in all three dimensions simultaneously and very robust against motion within the irradiated volume during the field delivery.

The uniform scanning (US) treatment mode differs in the absence of a second scatterer and resulting in smaller lateral beam size without a homogenous lateral dose distribution. Therefore, the beam is scanned several times across the lateral field size. Instead of the fast-spinning modulator wheel, the wheel is moved stepwise and the homogenous depth distribution is formed by irradiating several layers with decreasing dose per layer. Commonly, the layers are irradiated from the highest to the lowest energy. Apertures and compensators are used as for DS. Just for completeness, for small treatment fields like for treatment of eye tumors, homogenous lateral dose distributions can be formed with only one scatterer.

The active pencil beam scanning (PBS) differs in several aspects [26]. The beam profile is not manipulated in the nozzle. The lateral field distribution is formed with two independent scanning magnet pairs which steer the beam within the planned target area. Complex shapes can be irradiated with this technique, even holes can be in the irradiated area. Furthermore, the range of the beam is not manipulated in the nozzle. For each selected range, the energy of the proton beam is adjusted with the degrader. A homogenous dose distribution in beam direction is formed by adding several layers with decreasing relative weights. Large PMMA blocks, so-called range shifters (RSs), can be placed between the beam exit and the patient, if the minimal required range of the proton beam is smaller than the lowest possible range the treatment machine can deliver. Typically, a set of different thicknesses is commissioned for each beam line and thinnest possible is chosen for the treatment field to reduce the scattering in the RS. In order to make this delivery mode more robust against movement of the target, the repainting techniques have been introduced. In this case, each layer is irradiated several times, to avoid under dosage in moving targets. Furthermore, apertures can be used in PBS to achieve a sharper lateral penumbra which reduces the dose in organs at risk OARs [27].

The proton fields can be delivered with fixed beam lines, mostly implemented as horizontal beam lines, or a beam line can be mounted on a gantry system. With a gantry, which can be rotated 360° around the patient, nearly every geometry

for the irradiation is possible. As the beam line needs several magnets for beam alignment and focusing, such a gantry weighs about 100 t. The beam delivery is monitored with several ionization chambers to measure the delivered dose and the lateral position of the delivered treatment field.

2.3 Positron Emission Tomography for proton beam range verification

2.3.1 Positron Emission Tomography

The basic concept of positron emission tomography (PET) is to visualize the activity distribution of radionuclides which decay by the emission of a positron. The positrons emitted during the β^+-decay are stopped in the surrounding tissue and annihilate with an electron emitting two 511 keV photons back-to-back. The two photons are observed in a detector ring placed around the patient. Modern PET-scanner feature multiple detector rings to increase the sensitive area which can be obtained in parallel without moving the patient through the detector ring [28].

If two photons are detected within a coincidence time, the annihilation takes place along a line connecting the two detectors, referred to as a line of response (LOR). The general concept of PET is shown in Figure 2.4. Then, the activity distribution can be reconstructed from the intersections of multiple LORs. As the activity distribution may lead to multiple intersections which can occur randomly, further improvements are necessary. This can be done by reconstruction algorithms or with the timing information from the two photons reaching the detector. This method is called time of flight (ToF)-PET. Nowadays, the time resolution is about 100 ps which results in a spatial resolution of about 3 cm along the LOR [28, 29]. The current research on detector development aims to set up a system with a time resolution in the order of 10 ps. This time resolution would enable a so-called reconstruction-free PET as no further algorithms have to be used for the image reconstructions because a spatial resolution of about 3 mm would be below the residual positron range. This is the lower limit of the spatial resolution because the range of positrons in human tissue between 3 and 7 mm mean range for the relevant radionuclides is the offset between production and annihilation location of the positron [30, 31].

As the spatial resolution of 3 cm is not sufficient for diagnostic applications, further data processing and image reconstruction is necessary. Several reconstruction algorithms have been introduced over the past years. The commonly used algorithm is the ordered subset expectation maximization (OSEM), a simplified maximum likelihood expectation maximization (MLEM) algorithm. For the OSEM the set

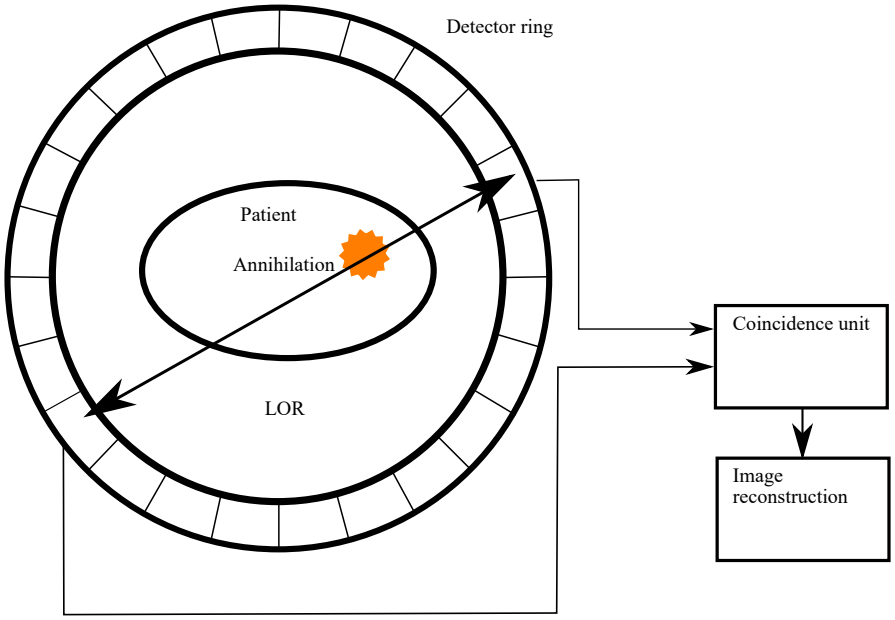

Figure 2.4: General concept of PET. The Line of response (LOR) is shown as an example. The coincidence unit features a discriminator and timing unit to improve the image quality. The image reconstruction is done on a computer.

of all LORs is split in multiple sets of data which cover the different equidistant angular parts of the detector ring. This accelerates the reconstruction compared to the MLEM for clinical practice. The MLEM method is an iterative algorithm. In each step, the most probable activity distribution (estimation maximization) which leads to the obtained LORs is estimated. In order to find the most probable image, the logarithm of the likelihood function is maximized as the derivative is set to be zero. With this condition, a new estimation of the image can be calculated. In clinical practice, the number of reconstruction steps is chosen in the settings. The MLEM-based algorithms seem to be superior for this application as they are more robust against noise which is important for low activity images like the ones after activation during treatment [32].

In modern PET scanners, scintillation detectors with silicon photomultipliers (SiPMs) are used for the photon detection. The scintillators, like lutetium oxy-orthosilicate, Lu_2SiO_5, convert the high energy annihilation photons in a light signal which is subsequently converted into a charge signal by the SiPM. This signal can be processed by the read-out electronics [28, 29].

In clinical practice, PET is used to visualize metabolic processes in the patient. A biological molecule is doped with a radionuclide and administered either intravenously or orally. The molecule follows the metabolic processes in patient while the radioactive decay is ongoing. After a pre-defined time, the activity distribution is measured with the PET to identify hyper- or hypodense areas which for example indicate tumor locations or under-supplied tissue. A commonly used molecule for PET imaging to visualize the glucose metabolism is fluorodeoxyglucose (FDG), glucose which is doped with ^{18}F [31].

For diagnostic applications, PET is combined with a second imaging modality like conventional X-ray computed tomography (CT) or magnetic resonance imaging (MRI) to overlay the metabolic information with the anatomic information from the second modality [28, 29, 33]. In addition, the information from the imaging can be used for attenuation and scatter correction of the reconstructed PET images. The attenuation and scattering of X-rays in the patient can be used to correct for the scattering and attenuation of the annihilation photons which are used for the PET imaging. This improves the image comparability of high and low density regions, as the photons in the high density regions are scattered and attenuated more compared to low density regions.

2.3.2 Application of PET for proton beam range verification

In contrast to diagnostic PET imaging, PET imaging for radiotherapeutic treatment monitoring makes use of the radioactivation of irradiated matter produced during proton irradiation. The produced distribution and types of radionuclides depend on the irradiated material [15]. As the main contribution to the dose are ionization processes, the produced activity distribution and the planned dose distribution do not have any direct dependence because the production of radionuclides is caused by

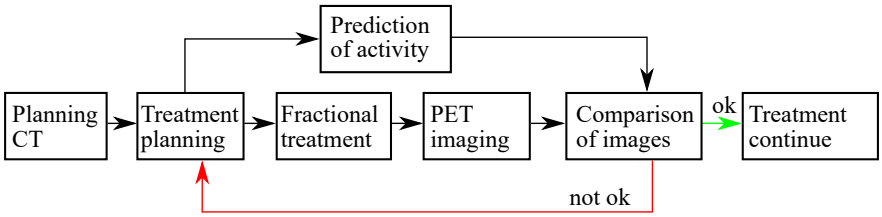

Figure 2.5: Possible clinical workflow of the implementation of PET imaging for fractional dose monitoring. The PET imaging would be done for each treatment plan during the overall treatment.

nuclear interactions [3, 8]. In consequence, the activity has to be predicted using MC simulations of the treatment plan. As a result, the predicted and measured activity can be compared. From the comparison of both activity distributions, potential improvements of the treatment plan can be developed as deviations between the predicted and observed activity distribution would be caused by a different irradiation of the proton field as expected from the treatment planning. A potential reason might be anatomic changes in the patient, delivery uncertainties of the treatment machine or uncertainties in the estimation of proton interactions from CT imaging. The process is summarized in Figure 2.5.

However, the benefit of PET imaging for range verification is limited. The activated tissue and biological molecules are subjected to many transport processes like metabolism or diffusion. In result, the produced activity distribution is not only decreasing due to the radioactive decay. One possible solution is to keep the time between irradiation and imaging as short as possible and place the imaging system in the treatment room [9]. As the imaging system is not portable, multi-room centers would need to equip each beam line with a dedicated imaging system if this method were to be implemented in their clinical work flow.

As PET imaging is performed after the irradiation is finished, all these methods are called off-line range verification. Additionally, so-called on-line methods have been developed, mainly based on the prompt gamma-rays, photons emitted during the nuclear interactions of the protons with the target nuclei. With the properties of the photons like their energy up to 10 MeV, the position of the proton beam in the patients can be estimated. On-line corrections of the treatment plan during the fractional treatment might be possible using these techniques. However, all these techniques have not been introduced in clinical routine as the limitations currently dominate the potential clinical advantages.

Therefore, implants have been proposed to overcome limitations of PET imaging for range verification as implants are not subjected to any transport processes [10, 11]. The advantages of various implants have been discussed for proton beam range verification in the literature. In addition, prior to this work, the potential use of titanium implants from surgical resections has been investigated. Based on these results, further investigations are presented in this work [12, 13].

2.4 The West German Proton Therapy Centre Essen

Today, the West German Proton Therapy Centre Essen (WPE) is the largest proton therapy center in Germany. The WPE proton treatment machine is a 230 MeV isochronous cyclotron from IBA (IBA Proton Therapy, Louvain-La-Neuve, Belgium)

implemented in a Proteus Plus system with four treatment rooms and five clinical beam lines. The beam lines allow for the different treatment modes for clinical patient treatment. Three treatment rooms are equipped with a gantry which can be rotated 360° around the patient, so-called gantry treatment rooms (GTRs). One additional room, the fixed-beam treatment room (FBTR) features conventional beam line, comparable to the beam lines in the GTR which is fixed to a horizontal beam direction and a dedicated beam line for eye treatment which feature a special treatment mode with high dose rates and low ranges. The proton treatment system is shown in Figure 2.6.

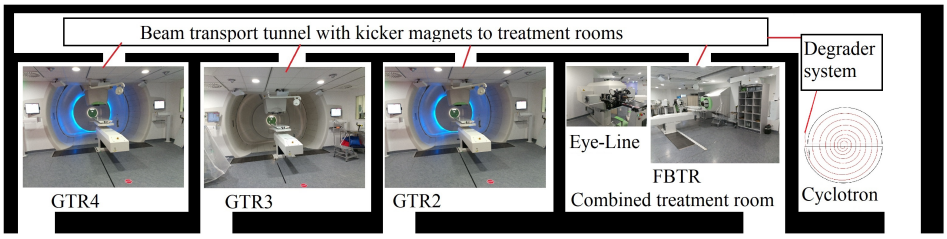

Figure 2.6: The proton therapy machine at the WPE. The 230 MeV cyclotron and the degrader with the energy selection system and the beam line are shown as sketch. The treatment rooms are represented with photos.

The degrader system mounted at the cyclotron exit can deliver proton energies between 100 MeV and 226.7 MeV which correspond to R80 of 7.7 cm and 32 cm in water [19]. Lower residual range for patient treatment can be achieved with PMMA range shifter (RS) mounted on the nozzle exit. For the different treatment rooms, two or three RS with defined water equivalent thicknesses can be used for treatment with PBS.

All experiments presented in this work are performed in FBTR or GTR4. This decision is based on several reasons. Firstly, both beam lines operate in PBS treatment mode. The PBS has the advantage of less production of secondary particles like neutrons which results in more accurate results for the measurement of activation cross sections [24, 34]. Furthermore, for MC simulations, PBS treatment fields can be implemented easier than simulations of passively scattered treatment fields. Secondly, for these two beam lines, the number of protons per dose has been determined prior to the presented studies using a Faraday cup (FC) [34, 35]. In result, the number of protons for each field can be calculated with an accuracy of about 1%. Each of the beam lines feature a set of ionization chambers, so-called monitor chambers, to verify the delivered dose distribution. The delivered dose is internally measured in so-called monitor unit (MU).

3 Measurement of radioactivity

3.1 Physics basics

3.1.1 Radioactivity and decay modes

Radionuclides can be produced during cosmic processes like supernovae or by high energy particle beams or cosmic rays during nuclear reactions. Depending on the number of protons and neutrons in the nucleus, nucleons can be emitted from the nucleus or converted into each other. A general model of the energy levels is shown in Figure 3.1 [36]. The dimensions are not to scale. This model is one of the models for nuclear processes developed over time which can be used to understand radioactive decay. However, different nuclear models might be used for other purposes. For

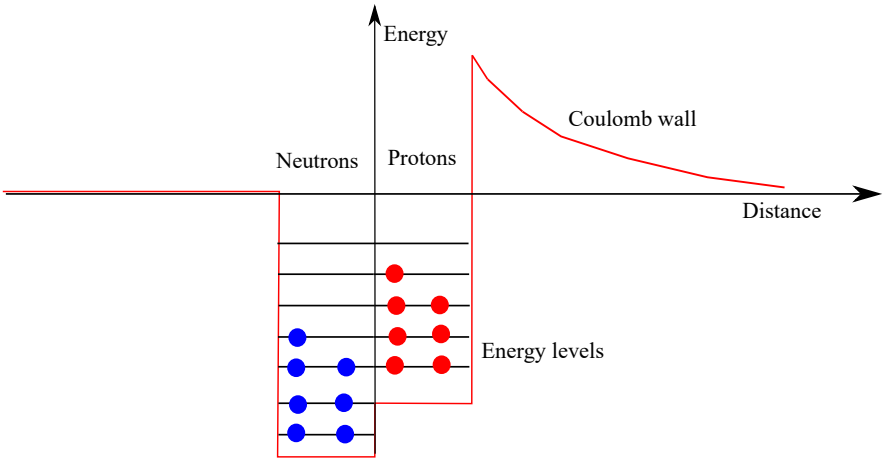

Figure 3.1: Energy levels in a nucleus with the Coulomb wall for the protons. The dimensions of the energy levels are not to scale.

unstable nuclei, it is observed, that the number of decays per time is proportional to the number of residual nuclei N. This differential equation is solved by the decay equation

$$N = N_0 \exp(-\lambda t), \tag{3.1}$$

where N_0 is the number of initial nuclei, t is the time of observation and $\lambda = \ln(2)/T_{1/2}$ is the decay constant calculated with the half-life $T_{1/2}$. The derivative $^{dN}/_{dt}$ is the activity A.

During the α-decay, a ^{4}He nucleus is emitted from the nucleus, resulting in a new nuclide, which differs in the atomic number by four and the charge of the nucleus by two. The α-decay is only possible for heavy nuclides as the energy levels above the vacuum level have to be filled by protons and neutrons. A pair of two protons and neutrons can tunnel through the barrier visualized in Figure 3.1. Once the α-particle is outside from the barrier, it is accelerated in the Coulomb field of the residual nucleus up to several MeV. The range of α-particles in matter is up to several cm in air depending on the density [19].

For applications discussed in this work, the β-decay is more relevant. The β-decay can be divided into the β^+-decay and the β^--decay. The first decay mediated by the weak interaction is the conversion of a proton into a neutron by the emission of a positron and an electron neutrino. In contrast, the β^--decay is the decay of a neutron into a proton associated with the emission of an electron and an electron anti-neutrino. The energy level criteria is according to the one for the β^+-decay but the binding energy of the neutron is higher compared to the proton.

As two particles are emitted during the β-decay the energy spectrum of the positron or electron is continuous with a maximum energy associated with the difference of the energy levels of the protons and neutrons. The produced positron is stopped in the matter around the radionuclide and subsequently it annihilates with an electron from the matter. As a result, two photons with an energy of 511 keV, which corresponds to the mass of the positron and electron, are emitted in opposite direction. Three photons are emitted from the annihilation in the case the electron and the positron have the same spin for spin conservation. The two 511 keV photons can either be measured during gamma-ray spectrometry of a sample or during PET imaging [28, 29]. As the photons do not have any information about the initial decay, the radionuclides can only be identified by the half-life of the initial decay.

During the electron capture, an inner electron is captured from the lowest energy levels and the conversion of a proton in a neutron. During this process an electron neutrino is emitted. As the process is similar to the β^+-decay, both decay modes can be competing to each other for some radionuclides. Furthermore, some radionuclides can only decay by the electron capture because the β-decay is prohibited by the energy conservation.

The most interesting process for the gamma-ray spectrometry is the γ-transition. This process is not a decay as the nucleus is not changed regarding the number of protons and neutrons. A photon is emitted, if a proton or neutron is changing the

energy level to a lower one. The specific energy difference is emitted with the photon. As a consequence the energy of the emitted photon is specific for the radionuclide [37, 38]. However, radionuclides with similar proton and neutron numbers have similar energy levels which might not be differed by the experimental setup due to the limited energy resolution of the detector system [38]. During one process, multiple single transitions may occur which results in multiple photons emitted during the process. Some of the photons not contribute to all transitions of a nucleus, which is represented by an emission probability less than one. The number of expected photons over time for each energy can be calculated from the activity.

The γ-transition is following one of the other processes described above [37]. As a result, other decays can be measured indirectly using gamma-ray spectrometry. Additionally, the nucleus can excited by radiation, like proton beams or gamma-rays or during nuclear reactions. The typical radionuclides produced during nuclear reaction have only short half-lifes and the photons are emitted within several ms after the reaction and commonly known as prompt gamma-rays. As the energy levels shown in Figure 3.1 are specific for the different nuclei, the energy of the emitted photons is specific for the radionuclide. However, nuclei with similar number of protons and neutrons have similar energy levels and in consequence, it is more difficult to separate them with the energy of the emitted photons [37].

3.1.2 Interactions of gamma-rays with matter

In the energy range between 10 keV and 10 MeV, three different interactions of gamma-rays with matter are dominant in the different energy intervals. In Figure 3.2, the different mass attenuation coefficients μ/ρ are shown for the interactions in germanium [39]. Germanium is chosen as the exemplary material as the Dortmund Low Background Facility (DLB) features a high-purity germanium (HPGe)-detector [40]. The high atomic number of germanium increases the reaction probability and thus the detection efficiency.

For low energies up to about 100 keV, the photo effect is dominant. During the photo effect, the photon is absorbed by an electron which is subsequently emitted from the atom. The residual energy of the electron is the energy of the incident photon E_γ reduced by the binding energy of the electron E_{bin}. The energy threshold for this interaction is given by the binding energy of the electron [41]. The kinetic energy of the electron E_{kin} can be calculated as

$$E_{\text{kin}} = E_\gamma - E_{\text{bin}}. \tag{3.2}$$

A more detailed investigation of the photo effect reveals, that the highest interaction probability is expected with the electron with the highest possible binding energy.

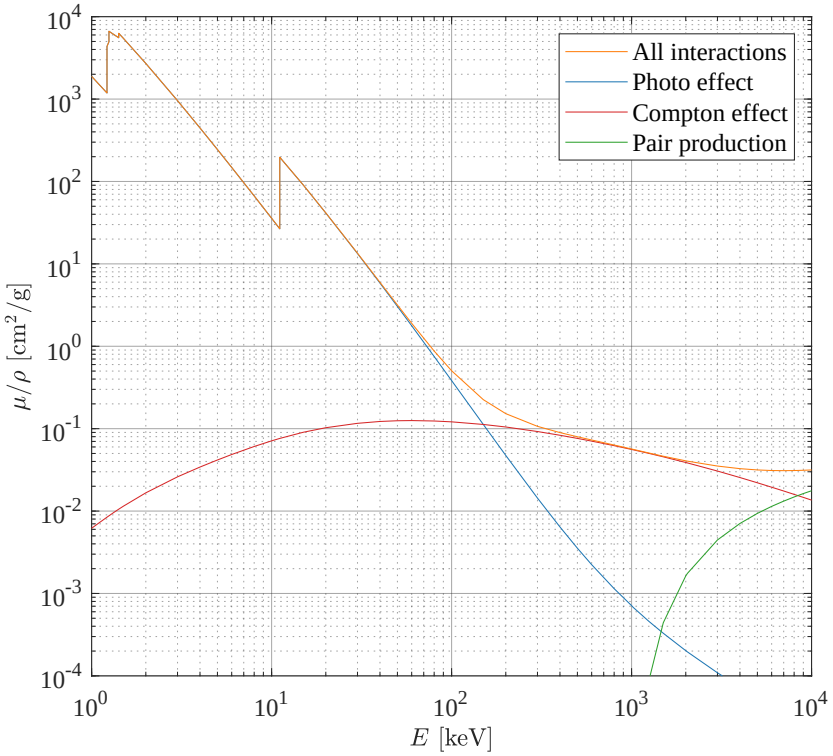

Figure 3.2: Mass attenuation coefficients for the three interactions photo effect, Compton effect and pair production in germanium depending on the photon energy. The sum of all three interactions is shown as well. Data taken from the XCOM database [39].

Characteristic edges in the attenuation coefficient can be observed at the corresponding energies for the deeper bounded electrons, as more processes contribute to the interactions. The electron is subsequently stopped in the surrounding matter.

The Compton effect describes the scattering of a photon and weak bounded electron [42]. From the momentum conservation, the commonly known Compton formula can be derived

$$\Delta\lambda = \lambda_{\mathrm{C,e}}(1 - \cos(\phi)) \tag{3.3}$$

which describes the change of the wavelength of the scattered photon. In the equation, the Compton wavelength of the electron is $\lambda_{\mathrm{C,e}} = {}^{\mathrm{h}}/_{\mathrm{m_e c_0}}$ and ϕ is the scattering angle of the photon. It can be calculated, that the energy transfer to the electron is maximized for $\phi = 180°$ which means, that the photon is emitted in the

opposite direction after the interaction. Furthermore, the energy transfer on the electron E'_e is derived from the momentum conservation as

$$E'_e = \frac{E_\gamma(1-\cos(\phi))}{m_e {c_0}^2 + E_\gamma(1-\cos(\phi))}. \tag{3.4}$$

The last relevant interaction in the range of decay photons up to 10 MeV in case of excited states is the pair production. From a photon with an energy above 1022 keV, a pair of an electron and a positron can be produced in the Coulomb field of a nucleus which is necessary for momentum conservation. The lower energy limit is caused by the mass of the electron positron pair. As described for the β^+ decay, the positron is subsequently stopped in the matter and annihilates with an electron by the production of a pair of two new 511 keV photons. These two photons have to be considered as they can possibly leave a sensitive detector volume. The pair production is a significant effect above several MeV and the dominant effect above 10 MeV.

3.2 Gamma-ray spectrometry

3.2.1 Detectors in gamma-ray spectrometry

Two different detector systems are used for gamma-ray spectrometry [38]. While scintillation detectors convert the deposited energy from the gamma-rays to visible light or ultra-violet light, semi-conductor detectors convert the deposited energy in an electric signal. While scintillation detectors are fast, semi-conductor detectors have a higher energy resolution and are used for high precision measurements. The DLB features a semi-conductor to achieve a high energy resolution for radio-purity measurements [40, 43].

The principle concept of semiconductor detectors is the p/n diode. In the sensitive crystal volume of the diode, the deposited energy is converted in a charge pulse. The charge is proportional to the deposited energy in the detector which allows for the energy measurement. The charge can be measured as current in the detector diode. In the first step of signal processing, the charge pulse is converted in a voltage signal. To do this, the amplifier features an integrator circuit with a capacitor. The signal is now a voltage signal which is proportional to the initially deposited energy. As the capacitor is charged by the current in the detector and subsequently discharged, in this time period no further signal can be processed by the read-out system. This time is the dead time of the detector system. To prevent a new signal processed during discharging of the capacitor, a pile-up rejection (PUR) is used to detected

a second signal from the detector in the signal processing phase and discards the incoming signal.

The second step of signal processing is the conversion in digital format with an analog digital converter (ADC). A multi-channel analyzer (MCA) with 8192 channels is used at the DLB. The range of voltage signals appearing in the measurement range of the DLB is split in 8192 channels and the pulse from the amplifier is counted in one of the channels depending on the pulse height. The resulting spectrum of the measurement in divided in 8192 channels with an equidistant resolution over the complete energy range. The initial deposited energy is proportional to the channel number of the MCA [38, 40, 43, 44].

3.2.2 Gamma-ray spectra

In Figure 3.3, a gamma-ray spectrum of the potassium isotope ^{40}K is shown. During the decay of ^{40}K a photon with a characteristic energy of 1461 keV is emitted [37]. This results in a sharp peak visible at 1461 keV, the so-called full energy peak (FEP) which represents all photons, which deposit their complete energy in the sensitive detector volume. The energy can be deposited within one or more of the interactions listed in Chapter 3.1.2. Two more peaks can be identified in the spectrum at 511 and 1022 keV lower energies compared to the FEP. The entries in the peaks are caused if one or both of the annihilation photons leave the sensitive detector volume without interactions after a positron was produced during pair production by the initial photon. As the peaks are associated with the escape of one or both annihilation photons, they are named single escape peak (SEP) and double escape peak (DEP). In the shown spectrum, the peaks can be identified at 950 keV (SEP) and 439 keV (DEP). As the pair production is only possible for photon energies above 1022 keV, only these peaks come with a SEP and DEP.

The second component of the spectrum is the Compton continuum up to 1244 keV. The sharp edge at this energy is given by the maximum energy transfer during the Compton interaction according to Equation (3.4). Entries in the spectrum between the Compton continuum and the FEP can only be caused by multiple Compton interactions and the photon leaves the sensitive detector volume after the interactions. In the energy range of the Compton continuum a fourth peak is visible. This peak has a larger width compared to the other peaks. In the shown spectrum, the peak is located at 217 keV. This energy is the residual energy after a Compton interaction of a 1461 keV photon with a scattering angle of 180°. The peak is induced by photons which are back scattered from the shielding and reach the detector volume afterwards.

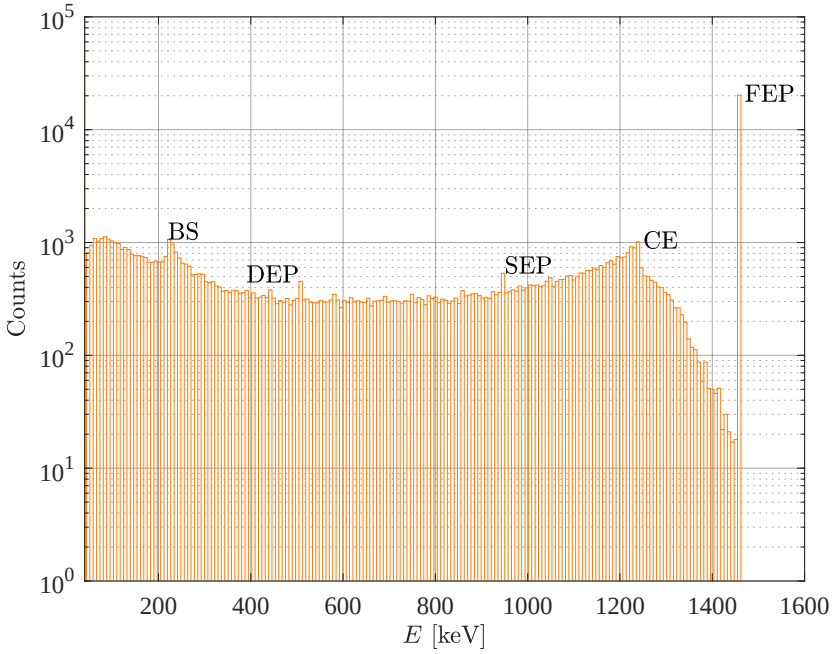

Figure 3.3: Exemplary simulated gamma-ray spectrum of a ^{40}K source. The full energy peak (FEP), the single and double escape peaks (SEP and DEP), the Compton edge (CE), and the back scatter peaks from photons back-scattered in the detector shielding are visible in the spectrum.

Samples with multiple radionuclides lead to multiple peaks with different intensities. Depending on the intensities of the single FEPs, some peaks can be dominant compared to the background from peaks with higher energies or might be invisible. Invisible peaks might be covered by the Compton continuum of peaks at higher energies. The visibility depends on the emission probability and activities of the peak compared to the intensity of peaks at higher energy. Even coincidences of more than one initial decay photons are possible. The probability depends on the activity of the sample and the time resolution of the used detector system.

The first step of the analysis of a gamma-ray spectrum is to assign all peaks to the radionuclides in the sample. In addition, the background spectrum of the detector system may disturb the measured spectrum further [40, 43]. As a result, peaks with decay rates close to the background activity might not be visible in the spectrum. The shown spectrum is obtained by a MC simulation [45, 46]. If the activity of the sample is close to the detection limit, a long measurement time is necessary to identify the peaks in the spectrum. For activated samples from irradiations, the

half-life of the radionuclides are relevant and it might not be possible to observe the radionuclides in the spectrum.

3.2.3 Determination of the activity from gamma-ray spectra

Once, the radionuclides are identified in the gamma-ray spectra, the activity can be calculated. Therefore, two steps are required. At first, the net count rate, the count rate subtracted by any background entries in the spectrum, of each peak is determined. Secondly, the activity has to be calculated from the net count rate.

Two different standardized protocols have been developed to determine the net count rate of each peak in the past. The latter one, DIN ISO 11929:2011 is used in the present work [47]. Both protocols describe the estimation of the background which is subtracted from the peak count rate. The background can either be induced by the Compton continuum from other peaks from the sample under study at higher energies or from radioactivity in the shielding material or the cosmic or environmental radiation [40]. Furthermore, peaks appear at different energies without a sample in the detector system in the background spectrum of the detector system. These peaks stem from environmental activity or cosmic rays [44, 48]. Especially in samples with activities at the level of the environmental radioactivity, the net count rate of the peaks in the background spectrum has to be subtracted from the net count rate in measurement spectrum, as the activity might be over-estimated due to the background activity.

The second step is the calculation of the activity from the net count rate. To do this, different effects have to be taken into account. At first, the emission probability, which is a radionuclide specific constant for each decay energy and describes the probability of emission of the corresponding photon during the decay needs to be considered. As different energy levels can be part of the decay process, the emission of different photons with different energies can be part of the decay. As a second effect, not all emitted photons reach the sensitive volume of the detector. The solid angle compared to the complete coverage of the sample with the sensitive detector volumes considers the loss of photons which are emitted in different directions and do not hit the detector. At last, the sensitive volume of the detector is limited. As a consequence, the detection efficiency is limited, as the interaction probability of the photons with the detector material is limited. In summary, the activity A can be calculated from the net count rate Z with

$$A = \frac{Z}{\Omega \epsilon Q} = \frac{Z}{fep}, \tag{3.5}$$

with the solid angle Ω, the efficiency Q and the emission probability ϵ. The product of all three factors is called full energy peak efficiency fep. The fep can be calculated from calibration measurements or, as implemented for the DLB, estimated with MC simulations [40, 43].

A special case is the annihilation peak (AP) which is induced by one of the photons from the electron positron annihilation. In contrast to the characteristic energy of other peaks, the energy of 511 keV is not specific for a single radionuclide. Thus, the analysis of the half-life is mandatory for this peak to verify the radionuclide in the peak. Furthermore, this peak has some special properties compared to the other peaks. While the width of the gamma-peaks is mainly given by the energy resolution of the detection system, the width of the AP is broadened by various other physical properties. The momentum of the positron is nearly zero during the annihilation process, but a residual momentum of the positron leads to an energy distribution of the annihilation photons, which is called Doppler broadening [49, 50]. Furthermore, a positronium, an electron positron bound state can be formed prior to the annihilation process. Depending on the spin of both particles, a third photon is emitted because of the conservation of the spin.

In consequence, the determination of the width of gamma peaks described in the protocols is not valid for the AP. A width of several keV is observed for this peak. For a correct analysis of the peak, the broadened width has to be taken into account. During a pre-study, this method has been verified with a ^{22}Na source [51]. The radionuclide ^{22}Na decays by the emission of a positron and has characteristic photon decay energy of 1275 keV as well [37]. For other radionuclides like ^{11}C or ^{18}F which decay only by the emission of a positron, the AP has to be analyzed [37].

3.3 The Dortmund Low Background Facility

The Dortmund Low Background Facility (DLB) is a low-level gamma-ray spectrometry laboratory at TU Dortmund University [40, 48]. The detector system is placed at the ground level and the laboratory is easily accessible. As a result, a massive outer shielding and special shielding design including an active veto system yield to a low net count rate which is comparable to net count rates achieved by natural shielding by placing the detector system below the ground level [40].

The complete arrangement of the DLB is shown in Figure 3.4. The outer shielding consists of about 320 t of barite-concrete and 43 t of cast-iron. The iron parts are placed directly above the lead castle housing the detector. The concrete modules are arranged to have a shielding between 1 and 1.5 m on all sides around the detector. All in all, the outer shielding corresponds to 10 m of water equivalent shielding

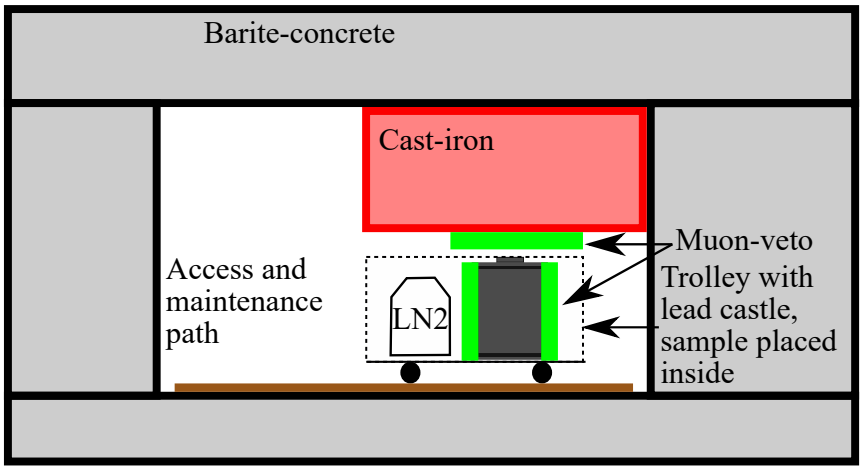

Figure 3.4: Shielding setup of the DLB with the barite-concrete (light gray boxes), cast-iron (red) and the inner shielding (lead castle, dark gray) in the center. The lateral parts of the muon veto (green) are not shown. The liquid nitrogen dewar (LN2) and the lead castle can be moved to the maintenance path to remove the plug from the top side to reach the sample chamber. The dimensions are not to scale.

which is a low amount of shielding compared to other low-background facilities [40, 43]. The water equivalent thickness of the detector shielding is used to compare the different low background facilities in terms of shielding. While most of the cosmic rays are stopped, the hard cosmic radiation, mainly cosmic muons, are not stopped in the shielding and can still reach the detector. To reduce the muon induced background, an active muon-veto covers the lead castle. The muon-veto itself consists of an arrangement of scintillation detectors with a photo multiplier read-out system. Once, a muon is detected in the veto system, the measurement is paused for a short time such that the muon is not detected in the gamma-ray detector [44, 48].

The room in the outer shielding is set up as clean room to prevent any dust entering the shielding which potentially contain radioactive impurities. A multi-layer lead castle covers the detector itself inside. The several layers differ by the contamination of the lead with the radioactive ^{210}Pb. As a result, the ^{210}Pb in the background spectrum is reduced. The inner chamber of the lead castle is covered with high purity copper manufactured by electrolysis to avoid any radioactive impurities in the copper. The sample chamber itself is closed by a lead plug from the top. The

volume of the residual measurement chamber is 1 L [40]. The inner shielding is called lead castle and reduces the background induced by natural radioactivity. As neutrons are produced in interactions of cosmic rays with matter, these should not reach the detector [40, 43]. Therefore, a layer of boron-loaded polyethylene (BPE) is placed between the several layers of lead to moderate the neutrons and subsequently stop the neutrons in the inner lead layers.

The high-purity germanium (HPGe) detector crystal itself is protected from any mechanical damage by an aluminum end-cap. The detector crystal itself is germanium detector of about 1.2 kg (Canberra Semiconductor NV, Olen, Belgium). The measurement samples are placed in a sample box or plastic bag depending on their physical properties (powder, liquids, solids). The latter one is used in the context of the presented work. This should avoid any contamination of the measurement volume with radioactive sample material. The samples are commonly placed directly on the center of the end-cap.

To calculate the full energy peak efficiency introduced in Chapter 3.2.3, a MC model of the geometry of the complete arrangement has been developed [43]. For the measurement of the samples, only the inner shielding is simulated for performance reasons as the back scatter of radiation from the sample in the outer shielding is negligible. The complete model is implemented in the Geant4 framework VENOM [45, 46]. Therefore, a model of the DLB has been developed and implemented in Geometry Description Markup Language (GDML) [52].

As the DLB has been built for radio-purity research in the context of the Cadmium Zinc Telluride 0-Neutrino Double-Beta Research Apparatus (COBRA) experiment to choose material for the experimental setup, the DLB is designed for the measurement of activities below the natural radioactivity and for radionuclides of long half-lifes [40, 43]. As a consequence, the activity is supposed to be constant during the measurement time. These prerequisites are not met for the measurement of radio-activated samples from proton therapy. Firstly, for the context of this work, short-lived radionuclides are from interest and the activity is not constant during the measurement. Secondly, the activities are higher than the natural activity. However, some changes in the evaluation and adjustment in the process of the data acquisition have been implemented to allow measurements of samples with high activities [24, 34].

The correction of the decay of the radionuclide during the measurement can be derived from the mean value theorem, which states that the numbers of decayed nuclei during the measurement can be represented by a mean value

$$A_{\mathrm{meas}} T_{\mathrm{Life}} = \int_{t_1}^{t_1+T_{\mathrm{Life}}} A_0 \exp\left(-\lambda t\right) \mathrm{d}t. \tag{3.6}$$

In the equation, A_{meas} is the measured activity according to the ISO reference [47], T_{Life} is the life time of the measurement, the active time of the data acquisition. The decay corrected activity A_0 can be calculated with the equation, λ is the decay constant of the radionuclide and t_1 is the effective start time of the measurement. The effective start time is calculated with the half of the irradiation time, the half of the dead time in the measurement and the time between irradiation and start of the measurement. For some radionuclides, the dead time can be reduced, if the first time of the data acquisition is neglected for the evaluation. This reduces the uncertainty, as a constant dead time rate during the measurement allows to split the dead time half at the beginning and half at the end of the measurement. For that case, this time has to be added to t_1. Finally, the decay corrected activity is calculated as:

$$A_0 = \frac{A_{\mathrm{meas}} \lambda T_{\mathrm{Life}} \exp(\lambda t_1)}{1 - \exp(-\lambda T_{\mathrm{Life}})}. \tag{3.7}$$

The second optimization of the measurement protocol is to exploit the time resolution of the setup. Depending on the half-life of the radionuclides in the sample, the measurement is split in several intervals between 2 min to 1 h. To reduce the uncertainty of the measurement, the dead time is reduced to 1 s per interval which is the time resolution of the electronic read-out system. The first intervals of the measurement are neglected, if the dead time is more than 1 s per interval to reduce the dead time in the measurement. Together with the possible time resolution of the read-out electronics, which is limited to the system time of the MCA to 1 s, the systematic uncertainties have been estimated as

$$\Delta t_1 = \frac{1\,\mathrm{s}}{\sqrt{12}} \quad \text{and} \quad \Delta T_{\mathrm{Life}} = \frac{n_{\mathrm{Int}} 1\,\mathrm{s}}{\sqrt{12}}, \tag{3.8}$$

where n_{Int} is the number of intervals used in the analysis. The $\sqrt{12}$ is given by the fact, that the uncertainty represents the maximum range of the uncertainties to calculate the standard deviation from the uniform distribution. Together with the systematic uncertainty of the measured activity, which has been estimated as 3% with a uniform distribution during the characterization of the detector system, the systematic uncertainty of the decay-corrected activity can be calculated [24, 34].

At last, it has to be mentioned that a peak can originate from more than one radionuclide. An analysis of the half-life is necessary for the peaks in the gamma-ray spectra to identify their origin. For the case of more than one radionuclide contributing to a single peak, different time windows of the measurements can be identified from the measurement, in which one or the other radionuclide is dominant in the peak. Based on this information, the analysis of the activity can be performed.

4 Experimental consolidation of the $^{nat}C(p,x)^{11}C$-cross section

The determination of activation cross sections has been a field of nuclear physics since the 1950s [53, 54]. One of the frequently discussed reactions is the $^{nat}C(p,x)^{11}C$ reaction, as it has been used as a monitor reaction for the proton fluence estimation for many other cross section studies in nuclear physics experiments. As a consequence, many other cross sections have been measured relative to this reaction [55]. However, the measured cross sections for the $^{nat}C(p,x)^{11}C$ reaction vary by about 15% between the different literature sources independent from the proton energy [56]. The measured and published cross section data from the past have been collected in the EXchange FORmat for experimental numerical nuclear reaction data (EXFOR) database, aiming to provide a complete overview on the cross section data [56].

Today, the $^{nat}C(p,x)^{11}C$ reaction is one of the reactions which are back in interest in context of proton therapy research [34, 57–59]. Nuclear interactions are not the main contributor to dose deposition, but they can be used for post-fractional field verification [3, 8]. As ^{11}C with a half-life of 20.36 min [37] is the positron emitter with the largest half-life produced from biological molecules, the production of ^{11}C is back in interest [60]. Furthermore, if the activation of other elements is used, like described in Chapter 6, the cross sections from the literature may need to be re-evaluated carefully. As many other cross sections have been measured relative to the $^{nat}C(p,x)^{11}C$ cross section, the uncertainties translate directly in the uncertainties of the further cross section measurements. To predict activities accurately for field verification in proton therapy, an accurate knowledge of the absolute cross sections is crucial. The absolute activity is needed for verification of absolute delivered dose, while the range of the proton beam can be compared with relative activity distributions. The measurement of activation cross sections is the basic nuclear physics part to improve field verification in proton therapy.

As the discussed 15% difference still persists in the latest publications, a joint study is set up to evaluate the possible cause of this difference aiming to determine a new reference cross section for this reaction which can be used to normalize the known cross section data. The presented experimental study is one part of the joint study [61].

Two different excitation functions for the ^{11}C production from natural carbon have been published prior to this study. One set of experiments has been performed using gamma-ray spectrometry at the DLB subsequently to the activation at the WPE [34, 58]. The second experimental study features a setup which is placed directly in the proton beam line [59]. Both experimental setups come with different conditions which are investigated in the joint study.

The presented study investigates the different irradiation parameters with the setup of the target irradiation at the WPE and the subsequent measurement at the DLB. Some of the experimental parameters, the target size and the field size, as long as the field size is larger than the target area, have been investigated prior to this study and have been excluded to be the cause of a 15% variation in the measured cross sections. The further experimental parameters are investigated to complete all potential influences.

4.1 Experimental setup

4.1.1 Estimation of the lateral beam profile

Two different methods have been used to irradiate a target for subsequent cross section determination. A scanned proton field which is larger than the target area can be used on the one hand, and a single pencil beam spot on the other hand. For the scanned field activation, the target is irradiated with a field size which is four times the size of the target itself. It has a nominal size of 5 cm × 5 cm. For fields of this size, lateral effects can be neglected [62].

For the activations with one single pencil beam, lateral effects can occur, like a loss of protons as some of the protons are scattered in the components of the nozzle, like the vacuum window or monitor chambers, or the air itself. As a consequence, a low dose envelope can be observed surrounding the beam spot [63, 64]. A target with infinite dimensions would be the favorable setup for the activation with one single pencil beam, as the loss of protons would be prevented by this setup. However, this cannot be implemented in the experiment. The loss of protons depending on the target size is estimated, to correct later for the proton loss.

To determine the beam profile for the chosen experimental setup a new set of measurements is performed for this study. The measurements are performed at the same beam line (FBTR) with an IBA Universal Nozzle (IBA Proton Therapy, Louvain-La-Neuve, Belgium) with an IBA Lynx PT detector (IBA Dosimetry, Schwarzenbruck, Germany). The Lynx PT detector features a scintillation detector. The light of the detector is observed with a charge-coupled device (CCD) detector

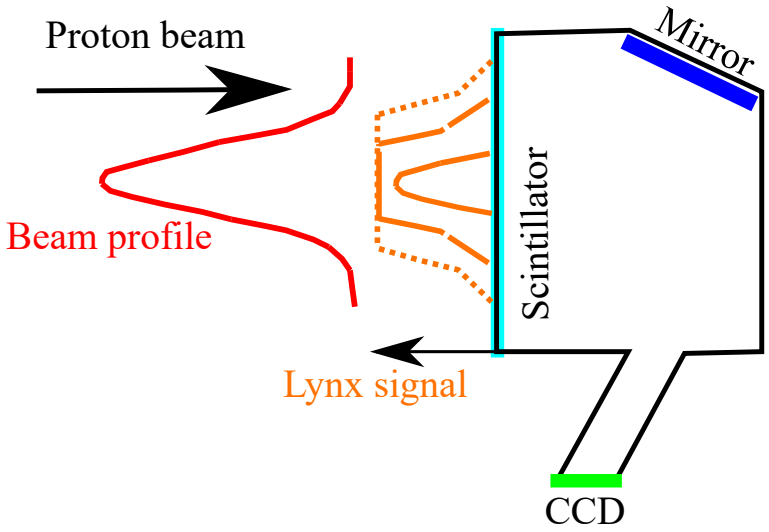

Figure 4.1: General setup of the Lynx PT detector with scintillator, mirror, and CCD sensor. The proton beam is delivered from the left-hand side (red beam profile). The box of the detector is closed avoid stray light from the treatment room. The signal of the scintillator is visualized in the schematic for all three measurements (orange solid, dashed, and dotted line with increasing proton fluence).

via a mirror. The general setup of the detector arrangement is shown in Figure 4.1. The lateral resolution of the detector is 0.5 mm with a sensitive area of 30 cm × 30 cm [65]. The scintillator plane is aligned at the isocenter plane, as it is done for the targets as well. As the dynamic range of the scintillator is limited to about two orders of magnitude, but a resolution of the fluence down to one permille of the maximum intensity is required, the so-called pair magnification method has been introduced to estimate the lateral beam profile of a single pencil beam including the lateral dose envelope by Lin et al. [66, 67]. The method has been optimized for the setup at the WPE prior to this work [68]. In a first step, a beam intensity is chosen, where the maximum signal of the detector is between 60 and 80% of the maximal possible signal. For the chosen beam energy of 100 MeV, 15 MU correspond to the target signal of the detector system. In the second step, additional images of the scintillation light are taken with 150 MU and 1500 MU. As a consequence, these additional images have a saturated area in the center of the beam spot. In the

analysis, the three measurements are rescaled by their inverse fluence ratios and the saturated areas in the images are substituted by the measurements with the lower beam intensity.

4.1.2 Gamma-ray spectrometry of activated graphite targets

During the prior work, different parameters have already been excluded as the cause for the systematic 15% difference of the different measured cross sections: the target size, the field size (as long as it is larger than the target), the target density and the number of initial protons [34]. However, the 15% difference persists in the recent publications. Table 4.1 provides an overview on the differences between the two experimental methods from the literature. The first experimental method has been developed in Essen and Dortmund [34] and is used in the further studies and the second one has been developed at the GSI Darmstadt [59]. This experimental setup can be taken to several irradiation facilities.

Table 4.1: Overview of the systematic differences between both experimental methods developed in Dortmund/Essen [34] and by the GSI group [59].

Parameter	Dortmund/Essen method	GSI method
irradiation technique	scanned field	single spot
target size	small target	large target
target density	low density	high density
target thickness	thin targets	thick targets
target alignment	perpendicular to beam	tilted by 45°
activity measurement	gamma-ray spectrometer	in-beam coincidence unit
number of protons	Faraday cup	ionization chamber

One possible reason for the discrepancy would be a systematic error in the measurement of the activity by one of the two experimental setups. This can be excluded by two different methods. The first one is the measurement of a calibrated radioactive point source, the second one the measurement of the same activated target with both setups. These two measurements are the first investigation performed in the study to check for possible systematic differences. A ^{22}Na (Eckert und Ziegler Nuclitec GmbH, Braunschweig, Germany) source is used to check the calibration of both experimental setups. It is observed, that the two methods of measuring the activity result in the same absolute activity within their experimental uncertainties [61]. The activities measured for the sample with both methods are $A_0^{\mathrm{GSI}} = (11.1 \pm 0.7)\,\mathrm{kBq}$ and $A_0^{\mathrm{Dortmund/Essen}} = (11.7 \pm 0.4)\,\mathrm{kBq}$.

As a consequence, one of the other parameters from the table might be the cause of the systematic difference of the 15% variation in the absolute cross sections. As the comparison of methods to measure the number of protons has been analyzed in the past [35], the first five parameters of Table 4.1 are investigated in the presented study by varying the parameters. Therefore, the parameters used in the GSI method are transferred to the Dortmund/Essen method. All the presented measurements are performed by irradiating the targets at the WPE and a subsequent gamma-ray spectrometry measurement at the DLB because targets activated by a single pencil beam can by analyzed at the DLB as well. With the in-beam coincidence unit featuring scintillation detectors close to the target at the beam line, scanned fields would irradiate the detectors as well.

Two different target materials from the same supplier are used for the set of activations, the one used in the Dortmund/Essen method and the one from the GSI method. The target materials from SGL Carbon (Wiesbaden, Germany) differ in their density: a density of $1.8\,\mathrm{g/cm^3}$ for the GSI target and $0.9\,\mathrm{g/cm^3}$ for the Dortmund/Essen target, respectively. The targets from the GSI are produced from a large solid and different thicknesses can be produced directly. For thick targets from

Table 4.2: Overview of the experiments performed for the investigation of the parameters. The ID is to identify the targets in the results section. (1) indicates that the result is taken from the prior study [34]. (2) is the irradiation performed during the joint experiment with both experimental studies [61].

ID	target material	z [mm]	ρ [g/cm^3]	lateral size [cm^2]	irradiation
A(1)	Dortmund/Essen	1.05	0.9	2.5×2.5	scanned
B	GSI	1.05	1.8	2.5×2.5	scanned
C	GSI	3.0	1.8	2.5×2.5	scanned
D	GSI	5.0	1.8	2.5×2.5	scanned
E	Dortmund/Essen	1.0	0.9	2.5×2.5	spot
F	Dortmund/Essen	1.0	0.9	2.5×2.5	spot
G	GSI	1.0	1.8	2.5×2.5	spot
H	GSI	3.0	1.8	2.5×2.5	spot
I	GSI	5.0	1.8	2.5×2.5	spot
K(2)	GSI	7.1	1.8	8.0×8.0	spot, tilted
L	Dortmund/Essen	15.2	0.9	7.5×7.5	spot

the Dortmund/Essen targets, a foil stack of multiple foils with a thickness of about 1 mm is used. The target material delivered to Dortmund/Essen has been analyzed by the supplier regarding any impurities. The potential impurities are below 0.001% in the analyzed part of the target [69]. The different single experimental parameters

for the irradiations can be taken from Table 4.2. To compare the different targets with the same thickness z and different densities ρ, the areal density $z\rho$ is introduced to be a representative of the number of target nuclei per target area. For a constant cross section, which is the expectation from the theoretical model of the cross section, the number of reactions should increase linear with the areal density for the same number of protons.

The targets are placed at the isocenter plane of the FBTR beam line and are supported by low-density foam from the back- and bottom-side. The low-density foam is removed after the irradiation and because of the low-density the proton scattering by the foam is assumed to be negligible. The targets which are irradiated with a scanned field are irradiated with a field of a full-width half-maximum of 5.25 cm × 5.25 cm with 1120.67 MU. This corresponds to a proton fluence Φ of $(3.32 \pm 0.04) \times 10^9/\text{cm}^2$. The targets irradiated with a single spot of a dose of 61.40 MU. This equals $(5.01 \pm 0.06) \times 10^9$ protons in the complete beam spot. Subsequently to the irradiation, each target sheet is brought to the DLB. The transport of 35 km lasts about 40 min. This time of decay has to be corrected for calculating the initial produced activity from the measured one [24, 34]. At the DLB, the target is placed in a plastic bag and directly on top of the detector end-cap. The side facing to the beam nozzle during the irradiation is the side of the target facing to the detector surface during the measurement.

This is a relevant part of the experiment, as the produced activity in the target increases with the depth in the target. This is caused by the energy loss of the protons in the target and the increasing cross section with decreasing energy [19, 56, 61]. The activity is not homogenous in the target which has to be considered for the estimation of the full energy peak efficiency by MC simulations. Therefore, the targets are divided in several slices with an increasing weight in the simulation depending on the increasing cross section. The weights represent the relative activation levels of the different slices of the target. The increase of the activation level has been estimated in a separate study [61]. Furthermore, the non-constant activation profile for the single spot activation has to be considered. The beam profile is used for the modeling of the activation profile. Therefore, multiple concentric cylinders are overlaid to approximate the Gaussian beam profile. For the tilted target, these circular profiles have to be tilted as well. As the geometry of the target and the DLB is implemented in GDML it is easily possible to generate these profiles with subtractions and intersections of the different shapes.

For the two different irradiation methods, two different equations to calculate the cross section σ have been derived in the single prior studies from Equation (2.2). For the scanned field activation [34], the cross section is calculated from the initial

activity A_0 with

$$\sigma = \frac{M_T A_0}{\mathrm{N_A} m_T \Phi_{\mathrm{proton}} \lambda}, \tag{4.1}$$

with the target mass m_T and molar mass M_T, the proton fluence Φ_{proton}, the Avogadro constant $\mathrm{N_A}$, and the decay constant λ of ^{11}C which is calculated from the half-life of 20.36 min [37] $\lambda = 567.3 \times 10^{-6}$/s. With the substitutions

$$\Phi_{\mathrm{proton}} = \frac{N}{F_T} \quad \text{and} \quad n = \frac{m_T \mathrm{N_A}}{M_T} \tag{4.2}$$

with the target area F_T, Equation (4.1) can be converted in

$$\sigma = \frac{A_0}{z \frac{n}{V} N \lambda} \tag{4.3}$$

with the target thickness z, the number of protons impinging the target N and the particle density of the target material n/V, which is used for the single spot activations [59]. The easily accessible representatives of the three objectives number of protons, number of reactions and number of target nuclei are used for the calculation of the cross section for the different irradiation methods.

The experimental uncertainties of the experimental setup have been investigated and discussed on detail in the past [34, 59]. The incident number of protons has been measured with a Faraday cup (FC) prior to the activation study [34]. The experimental uncertainties of this measurement including the reproducibility of the treatment machine have been estimated as 1.1%. Additionally, a second contribution stems from the activity measurement with the DLB setup. The uncertainty of the measured activity is 1.7% [43]. Additionally, the time for the decay correction has an uncertainty as described in Equation (3.8) in Chapter 3.3. The last contribution is given by the target itself. The target mass is measured with an accuracy of 0.01 g. All in all, the experimental uncertainties sum up to 2.4% which is a low uncertainty compared to many data from the literature [34, 56]. Additionally, a statistical uncertainty from the count rate during the gamma-ray spectrometry has to be added to the overall uncertainty [47]. The experimental procedure at the DLB has been optimized to reduce the experimental uncertainties as described in Chapter 3.3.

As the activation profile for non-uniformly activated samples is only an approximation with discrete steps, the simulations for the full energy peak efficiency are a further possible source of uncertainties. To estimate the uncertainties, different levels and activity distributions in one sample are simulated. As a result, for targets with a thickness of more than 1 mm (all samples except A, B, E, F, G) an additional uncertainty is of 1% is added to the overall uncertainty. The analogous principle is

performed for the single spot activations with the lateral beam profile. For these samples, an additional uncertainty of 1% is estimated as well. In summary, the overall uncertainty is 2.6% if one of the corrections for the non-homogenous activation profile needs to be applied and 2.8% for the samples with both corrections [61].

4.1.3 PET measurements of activated graphite targets

To validate the experimental results, a PET scanner is used for two more activation studies on graphite. Therefore, the two different targets are scanned in the Siemens Biograph Vision ToF-PET system (Siemens Healthineers, Erlangen, Germany). The calibration of the PET scanner has been validated with the same calibrated ^{22}Na source prior to the experiments which has been used for the validation of the setups in Chapter 4.1.2 [61, 70]. The deviation of 5% from the calibration certificate of the source is within the clinical tolerances of PET imaging [33] and is used as a systematic uncertainty of the absolute activity for the subsequent activation studies.

The first experiment can demonstrate the comparability of the irradiation of a stack and a thin foil. With the independent system for the estimation of the activity, it is possible to identify a possible issue affecting both systems from the experiments described in Chapter 4.1.2. Furthermore, the irradiation setup is more comparable to the ones from the past, where a stack of targets has been irradiated with one shot and the targets have been analyzed separately to obtain the energy dependence of the activation cross section [57]. This experiment is the activation of a graphite foil stack of 10 cm height. The foil stack has a lateral size of 2.5 cm × 2.5 cm. The stack is irradiated with a scanned proton field of 130 MeV. At a depth of 3.7 cm, the residual energy has an average of 100 MeV [19].

The second experiment is to compare the activation profile with the profile of the pencil beam spot. Therefore, a target of 5.0 cm × 5.0 cm is irradiated with one single pencil beam. The target has four different thicknesses. Each quarter of the target has a different thickness of one, three, five, and seven single target sheets from the Dortmund/Essen target material. The lateral profile of the pencil beam spot can be observed by PET imaging. However, this image is a superposition of the beam profile, the range of the positrons and the point spread function (PSF) of the PET scanner. In consequence, the results of this irradiation are not used for a cross section calculation. The target is irradiated with proton field of 100 MeV. To increase the efficiency, the target is placed in a PMMA absorber for the PET scan in which the positrons from the decay can annihilate.

Both PET scans last 2 h after the proton irradiation. In contrast to the clinical workflow of PET imaging, the CT is not acquired prior but subsequently to the PET acquisition. The data of the PET are acquired in list mode and the reconstruction of several images over time allow to cross check the half-life of the activity to verify the sensitivity to ^{11}C. A protocol for the radionuclide ^{22}Na with a half-life of 2.602 a [37] is used to avoid the implemented correction for a decay during the image acquisition of the PET system. As a consequence the emission probability is not applied correctly in the PET images as the one from ^{22}Na is used. Therefore, all absolute activities have to be corrected with ratio the emission probabilities of ^{22}Na and ^{11}C.

The OSEM reconstruction based on the ToF information is chosen for the reconstruction of the acquired PET images as it is discussed in Chapter 2.3.1 and recommended in the literature [32]. For the calibration of the absolute activity, several reconstruction algorithms have been investigated. All of the chosen algorithms are within the clinical acceptable tolerances [70]. The OSEM algorithm is used as suggested in the literature for post-fractional imaging [32].

4.2 Measurement analysis and results

4.2.1 Lateral beam profile of a single pencil beam

The evaluation of the lateral beam profile is required prior to the cross section measurements for the single spot activations to calculate the number of protons missing the targets. In a first step, the three acquired images have to be corrected for their individual beam center. This is necessary, as the positioning of the beam is centered during every beam request with the monitor chambers in the nozzle. As a result, small deviations for the three single measurements are expected to be visible. Once, this correction is done, the super-positioning of the three profiles is possible. Therefore, the three measurements are normalized with their individual weight in monitor units. The saturated areas in each image are substituted by the corresponding part of the image with the lower monitor units. An image with a large dynamic range of the individual beam spot is generated by this method [66, 67].

A double Gaussian distribution

$$f(x,y) = \alpha_1 \mathrm{e}^{-\beta_1\left((x-x_0)^2+(y-y_0)^2\right)} + \alpha_2 \mathrm{e}^{-\beta_2\left((x-x_0)^2+(y-y_0)^2\right)}, \tag{4.4}$$

with the parameters α_1, α_2, β_1, β_2, x_0, and y_0 and the image coordinates x and y is fitted to the overall beam profile. In the equation, α_1 and α_2 describe the weights of

the two components of the double Gaussian distribution and β_1 and β_2 contain the corresponding standard deviations of the beam profile. The parameters x_0 and y_0 represent a potential shift from the image center of the spot profile which becomes relevant, if the image coordinate system is not aligned with the beam coordinate system.

The distribution in Equation (4.4) is restricted by two conditions. Firstly, the shift of both Gaussian distributions is assumed to be the same. Secondly, a forced symmetry of the beam spot is forced by taking the same width in x- and y-direction. These conditions are correlated with the assumptions, that all scattering components in the nozzle are symmetric around the beam center and symmetric beam production and transport through the beam line. In clinical practice a symmetric beam spot shape is assumed in the TPS. However, the measured beam spot has a slight deviation between the width in x and y direction, but this difference is very low. The two assumptions reduce the number of free parameters for the fit.

The acquired and super-positioned beam profile is shown in Figure 4.2. The distribution from Equation (4.4) is fitted to the data. The results of the fit are collected in Table 4.3. From the parameters β_1 and β_2, the corresponding standard deviations σ (note σ represents the standard deviation of the Gaussian distribution in this section) are calculated with

$$\sigma_1 = \frac{1}{2\sqrt{2\beta_1}} = (7.8057 \pm 0.0027)\,\text{mm} \text{ and } \sigma_2 = \frac{1}{2\sqrt{2\beta_2}} = (13.21 \pm 0.04)\,\text{mm}.$$

With the two results, the lateral profile of the activation used for the MC simulation can be calculated. The result for σ_1 is close to the clinical used value in the TPS for a beam energy of 100 MeV at the FBTR beam line. However, a small deviation is expected, as the clinical TPS models the lateral beam profile using a single Gaussian distribution. The beam profile is normalized to the maximum of the measured profile. The sum of α_1 and α_2 is 99.29%.

In Figure 4.2, a characteristic step is visible in the beam profile at a very low intensity at about 0.01% of the maximum intensity. To understand the cause of this step, further investigations are performed to exclude an origin in the beam profile. This step can be observed with a second Lynx PT detector as well. Interestingly, if the Lynx PT is rotated by 180° around the beam axis, the step remains at the same position in the image coordinates, but the beam coordinates are rotated by 180° against the image coordinates. A beam specific issue can be excluded as the origin of this abnormal observation. A last possibility for the origin is the read-out electronics of the CCD sensor or a two-column sensor layout. However, the asymmetry has a very low intensity and the asymmetry is not visible in the fitted beam profile, which is caused by the model from Equation (4.4). In conclusion, this does not affect

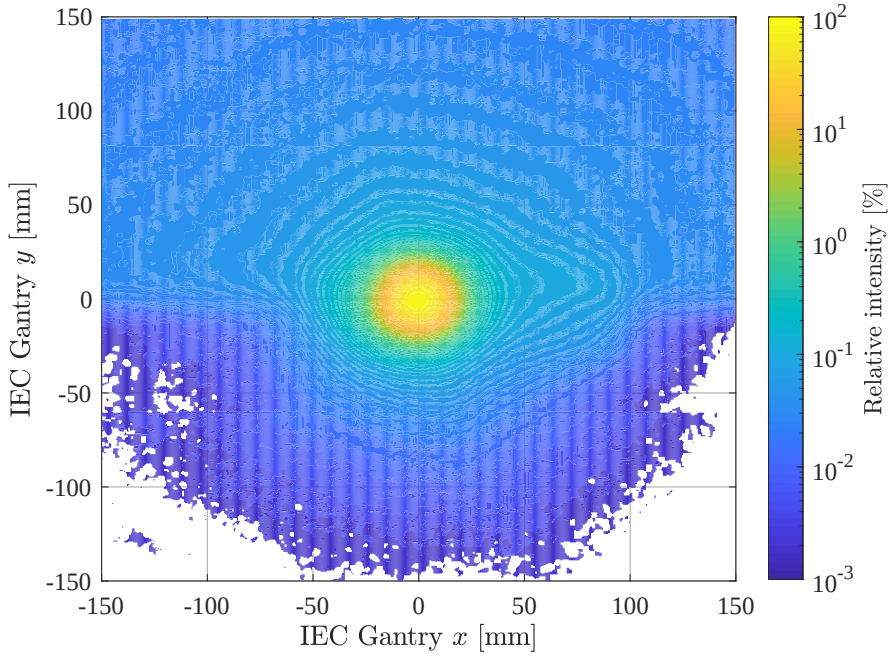

Figure 4.2: 2D profile of the single pencil beam spot measured with the Lynx PT detector. The image artifact on the level of 0.01% of the maximum intensity is visible as a step.

the usability of the results for the beam profile corrections for the activation cross section calculation.

To apply corrections for the protons missing the target for the different target sizes from Table 4.2, the integrals of the beam profile over the target areas are compared with the integral over the complete beam spot. The complete beam spot contains all protons which are counted in the monitor chambers and the scintillator size of 30 cm × 30 cm of the Lynx PT is assumed to contain all protons. To calculate the integral of the beam spot over the target, the beam profile is restricted to the size of the target. The relative number of protons hitting the target is the ratio between the integral restricted to target size and the integral of the complete beam spot. In Table 4.4, the relative number of protons missing the targets is listed for the different target sizes. For the tilted target, the projected size of the target on a surface perpendicular to the beam direction is used for the mask. To calculate the number of protons hitting the target from the number of protons in the complete beam spot which is measured by the monitor chambers, this correction needs to be applied.

Table 4.3: Parameters of the double Gaussian distribution according to Equation (4.4) fitted to the measured beam profile.

parameter	fit result
α_1 [%]	93.39 ± 0.04
α_2 [%]	5.90 ± 0.04
β_1 [10^{-3} pixel]	2.0516 ± 0.0007
β_2 [10^{-3} pixel]	0.7168 ± 0.0021
x_0 [pixel]	299.3956 ± 0.0008
y_0 [pixel]	299.7813 ± 0.0008

Table 4.4: List of correction for the loss of protons during single spot activations by protons not hitting the target. Note: The target K is tilted against the beam axis by 45° which results in more protons missing the target.

lateral size	affected IDs	correction [%]
2.5×2.5	E, F, G, H, I	28.0
7.5×7.5	L	0.9
8.0×8.0	K	1.5

4.2.2 Calculation of the activation cross section

The acquired gamma-ray spectra at the DLB are analyzed all in the same way. At first, the net peak content of the AP is calculated over time. As described in Chapter 3, all radionuclides which decay by the emission of a positron may contribute to the peak, a half-life analysis of the net peak content is used to verify, that the peak is assigned to the radionuclide under study, ^{11}C. No other radionuclide contributing to the AP is expected to be visible after 40 min of transport in graphite, as the radionuclide ^{10}C with a half-life of 19.31 s [37] is not visible in the spectrum any more. However, as impurities from other radionuclides have been found in other target materials in the past [24], this additional check is able to identify impurities on a relevant level. For all samples, the half-life fits to the one from the literature. An exemplary decay curve is shown in Figure 4.3. This decay curve is measured during the joint experiment with both experimental setups from Table 4.1 (sample K) [61]. To compare both setups, the count rate is converted to the corresponding activity, which is not necessary to verify the half-life. This conversion enables the direct comparison of both setups and it is visible, that both setups measure the same activity. The shown exponential fit to the data from the DLB describes the data of the in-beam setup as well. However, the fast decay of ^{10}C can be observed with the

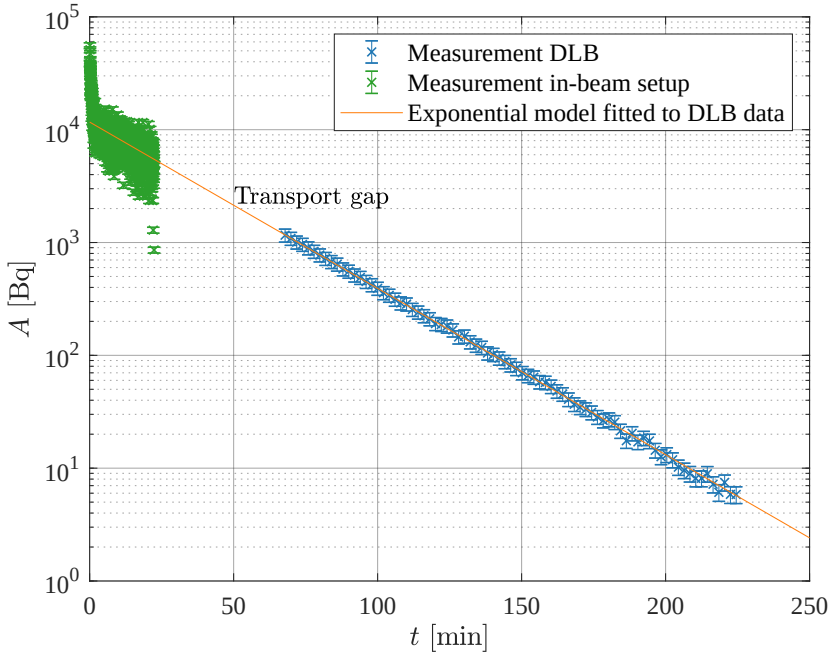

Figure 4.3: Activity over time for the target irradiated during the joint experiment. The fitted model from the DLB data matches with the activity from the in-beam setup as well. The time gap between both measurements is the time for the transport of the target.

in-beam setup and these data are not described by the fit [59, 61].

An exemplary gamma-ray spectrum is shown in Figure 4.4. In addition to the AP, two more peaks can be identified in the spectrum. The one at 477 keV is caused by the radionuclide ^{7}Be. This radionuclide has a half-life of 53.22 d [37]. Together with the lower production cross section by a factor of four, the activity in the samples is low and the statistical uncertainty of the results is on the 10%-level for the measurement time of several days. As this excitation function has been measured in detail in the past [34, 58], this peak is not evaluated further during this study. Furthermore, this radionuclide cannot be observed with the in-beam setup as the in-beam setup measures the coincidence of the two annihilation photon and ^{7}Be is not a positron emitter. A third dominant peak is visible at 682 keV. This is the coincidence of the AP and the corresponding backscatter peak. Those coincidences appear in spectra of samples with high activities and lead to errors in the calculation of the activity from the FEP. To avoid those errors and reduce the experimental uncertainties, only data are used for the analysis, once the dead time

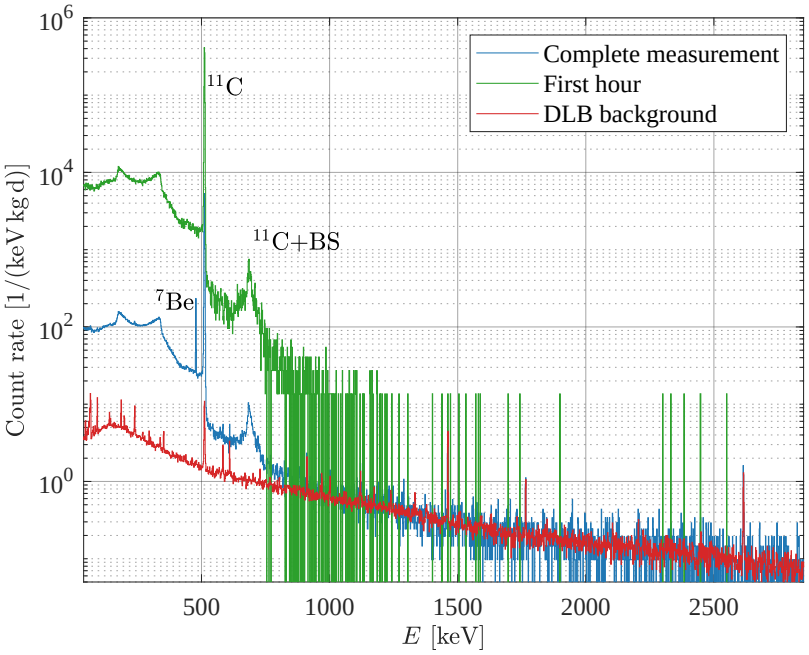

Figure 4.4: Gamma-ray spectrum for different time intervals of an activated graphite sample. The first 1 h (green) show a relatively high activity and a coincidence peak of the AP from ^{11}C and the corresponding back scatter peak (BS) is visible in the spectrum. In a long-term measurement (blue) the peak from ^{7}Be is visible as well. The background spectrum (red) is shown for comparison.

in a 2 min interval of data acquisition has reached the lowest possible level of 1 s, as described in Chapter 3.3 [24, 34]. It has been shown in prior studies, that the data of 1 h of measurement is sufficient to reach a statistical uncertainty below the level of the systematic uncertainties for sample which reach the 1 s dead time limit during the measurement time [34, 58].

With the data of 1 h, the activity is calculated from the net count rate subsequently. Therefore, the evaluation of each peak is performed as described in Chapter 3.2.3 according to DIN:ISO 11929:2011 [47]. For the analysis of the AP, the described validated adjustments of the peak width has to be done, compare Chapter 3.2.3. The validation has been done with the ^{22}Na source prior to the measurements [34, 51]. The measured activity is an averaged result, as described in Chapter 3.3. Once the measured activity is calculated, the decay correction between the irradiation and the start time of the analysis as well as the one for the decay during the measurement period is applied. As the last step the measured cross section can be calculated

according the Equations (4.1) or (4.3). The measured cross sections are collected with their corresponding initial activities in Table 4.5. The data for the calculation described here can be found in Chapter A.1.

Table 4.5: Initial decay corrected activity A_0 for each target and the measured activation cross section calculated from the activity. For completeness, the areal density $z\rho$ is added to the data. (1) indicates that the result is taken from the prior study. (2a) is the irradiation performed during the joint experiment with both experimental studies and (2b) is the cross section calculated with the in-beam setup.

ID	$z\rho$ [g/cm]	A_0 [kBq]	measured σ [mb]
A(1)	0.099	3.94 $\pm$ 0.07	70.2 $\pm$ 1.7
B	0.180	7.71 $\pm$ 0.14	70.4 $\pm$ 1.5
C	0.540	22.0 $\pm$ 0.4	67.4 $\pm$ 1.6
D	0.900	37.1 $\pm$ 0.7	69.1 $\pm$ 1.6
E	0.099	0.758 $\pm$ 0.017	69.7 $\pm$ 1.7
F	0.099	0.755 $\pm$ 0.016	69.4 $\pm$ 1.7
G	0.180	1.388 $\pm$ 0.029	68.6 $\pm$ 1.8
H	0.540	4.08 $\pm$ 0.10	67.3 $\pm$ 1.7
I	0.900	6.92 $\pm$ 0.16	68.4 $\pm$ 1.8
K(2a)	1.278	11.7 $\pm$ 0.4	64.7 $\pm$ 1.7
K(2b)	1.278	11.1 $\pm$ 0.7	61.5 $\pm$ 7.0
L	1.424	12.7 $\pm$ 0.4	66.6 $\pm$ 1.7

With the analogous principle of decay correction, the PET measurement of the activated foil stack is evaluated. However, this method differs in the estimation of the measured activity. A volume of interest (VOI) is placed around the point in 3.7 cm depth on the central axis of the foil stack. This is the depth, in which the medium residual energy of the protons is 100 MeV. The lateral dimensions of the VOI are chosen with the lateral profile of the activity distribution measured with the PET scanner. While the real activation is homogenous in the lateral direction, the PET image is not constant. This is caused by the general limitation of PET imaging. The image represents not the activity distribution at the origin of the positrons but the distribution of the annihilations of the positrons. As a result, the PET image of a point source is smeared by the range spectrum of the positrons. As the target stack is activated over the complete area, positrons emitted close to the edges can potentially leave the target material before they stop and annihilate. A smeared activity distribution is observed close to the target edges. In the middle of the target stack, an equilibrium of the positrons which enter or leave the volume can be assumed, as the emittance is supposed to be homogenous in all directions.

This results in a flat profile of the obtained activity in the middle of the stack, as the width of the target is larger than the range of the positrons.

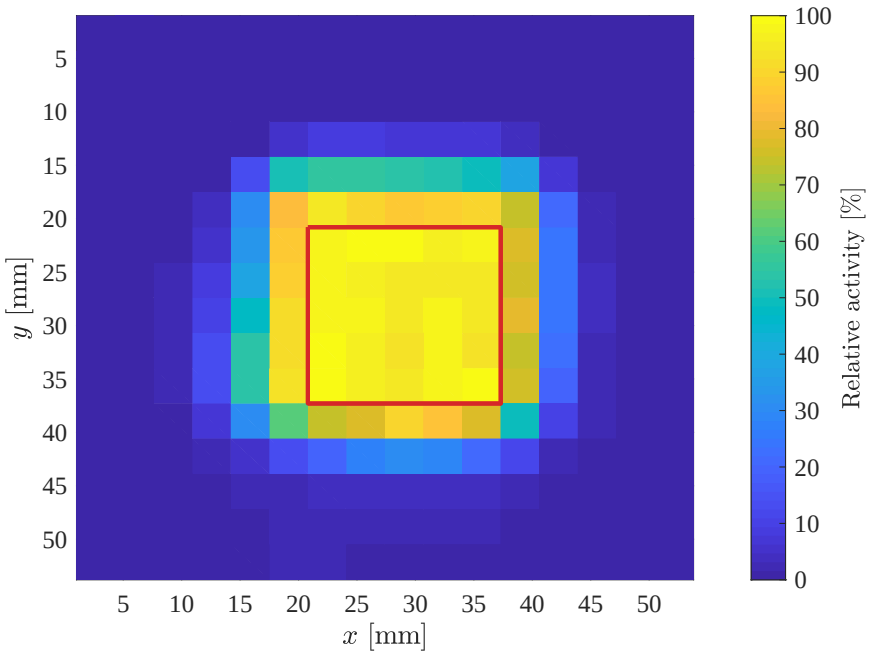

Figure 4.5: Relative activity distribution in 3.7 cm depth in the graphite stack. From the image, the lateral dimensions of the VOI is derived. The lateral dimensions of the VOI are shown in red.

The VOI dimensions are chosen as 16.5 mm × 16.5 mm in the lateral dimensions which is the homogenous area of the activity profile and 8.2 mm in beam direction. The lateral activity profile in 3.7 cm depth is shown in Figure 4.5. The activity concentration is integrated over the VOI and subsequently, the known decay correction is applied on the measured value. Finally, the cross section is calculated as (69.8 ± 3.6) mb. The uncertainty of this cross sections contains the uncertainty of the activation from the PET of 5% [33, 61, 70] and the 1.1% from the FC measurement which affects all result. The measured cross section is shown in Figure 4.6 together with the cross sections from Table 4.5. It is visible, that all measured cross sections are in agreement within their uncertainties and accumulate around one unified value.

With all the measured cross sections, the average cross section can be estimated. The weighted mean of (68 ± 3) mb represents all cross sections measured with the different targets and experimental setups. The weighted mean takes the different

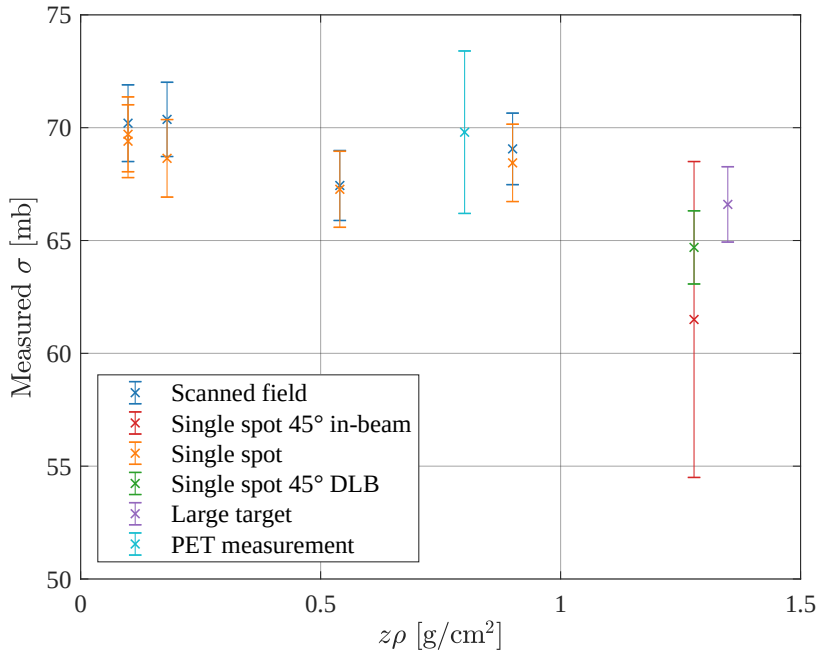

Figure 4.6: Visualization of all measured cross sections with the different targets and experimental setups. It is visible, that all cross sections agree within their individual uncertainties.

experimental uncertainties of the different methods of measuring the initial activity into account which directly translates in the experimental uncertainty of the derived cross section. To estimate the energy, the energy loss of the protons in the different targets from Table 4.5 is calculated with the stopping power for protons from the database [19]. The medium energy and the energy spread are taken as the energy and its uncertainty. The proton energy for this cross section is estimated as (97 ± 3) MeV.

At last, the consistency of the measurement can be checked with an additional approach. As already mentioned, the areal density $z\rho$ represents the number of target nuclei per area and thus the number of reactions per proton should increase linear with increasing $z\rho$. To check the consistency of the initial activities measured at the DLB which represent the number of reactions, the hypothesis of the linear increase is shown in Figure 4.7. It is indeed visible, that the measured data are consistent with a linear fit. Furthermore, the slope of the curve contains the cross section for the reaction under study together with some constants according to the Equations (4.1) to (4.3). From the shown fit, a cross section of (67.0 ± 1.7) mb

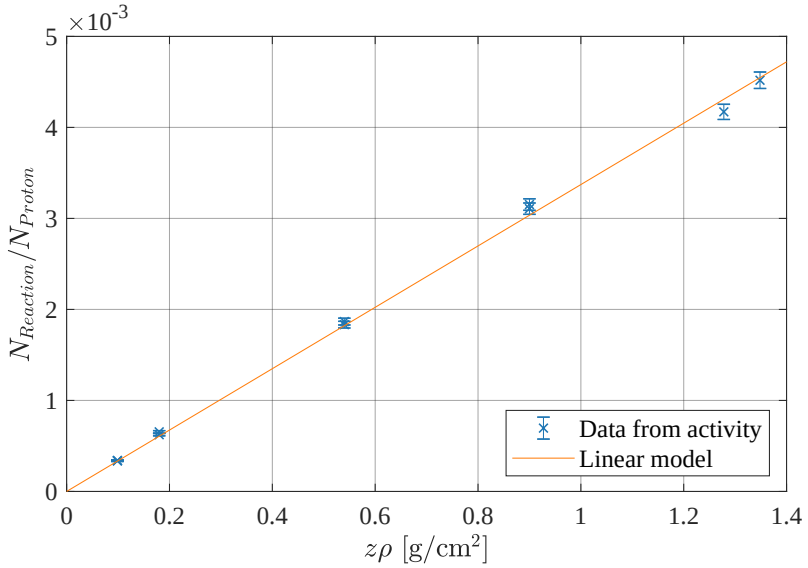

Figure 4.7: Linear increase of the number of reactions per proton $N_{\text{Reaction}}/N_{\text{Proton}}$ with the areal density $z\rho$. The linear model fits to the experimental data within their uncertainties.

is calculated. As this cross section is in agreement with the weighted mean, it is concluded, that all measurements are consistent. However, only the data calculated from the measurements at the DLB are taken for the fit to achieve the same conditions for all data.

4.2.3 Activation profile measurement with PET

Two different tests are performed to compare the activation profile with the fluence profile of one single spot and the increasing activity with target thickness. The analysis is done with the PET measurement of the target with four different thicknesses. The first test is the linear increase of the activity with the increasing target thickness. The thickness of one, three, five, and seven foils correspond to 1.05 mm, 3.15 mm, 5.25 mm and 7.35 mm. A VOI is placed in each quadrant of the target and the activity in the VOI is used as the representative of the activity in the part of the target. The thickness of the VOIs varies with the thickness of the sample in each quadrant. All four VOIs are shown with the matched PET/CT in Figure 4.8.

The activity is calculated for each VOI and the results are summarized in Table 4.6. The increase of the activity in each VOI is shown in Figure 4.9. It can be derived,

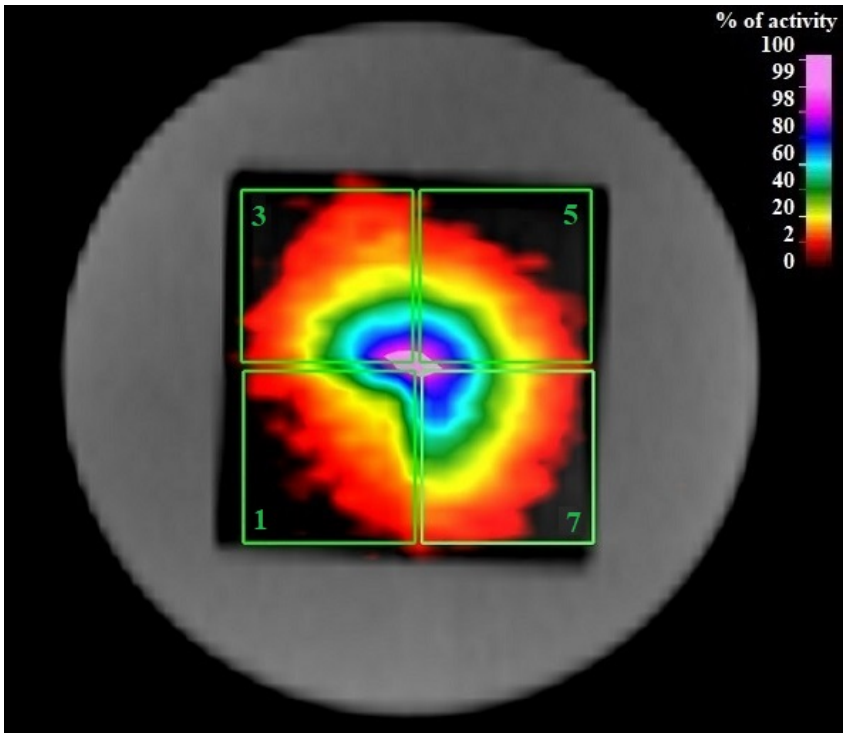

Figure 4.8: Four VOIs in the activity distribution measured in the PET overlaid with the CT. Numbers indicate the number of sheets in each quadrant.

that a large uncertainty might be associated with this method. In the visualization of the VOIs is visible, that the beam spot might not hit the target at the target center. The target is aligned by X-ray imaging at the beam line. However, the co-linearity of the proton beam compared to the X-ray imaging is limited with an uncertainty of 0.5 mm. Additionally, the steps of the targets are difficult to identify in the planar X-ray images which may result in a positioning uncertainty of the target. Furthermore, the VOIs are close to each other. As already described in

Table 4.6: Activities in the different VOIs with their volume V and thickness z.

number of sheets	z [mm]	V [mL]	A [Bq]
1	1.05	3.23	559.15
3	3.15	5.05	1984.65
5	5.25	6.47	2435.66
7	7.35	9.20	3373.15

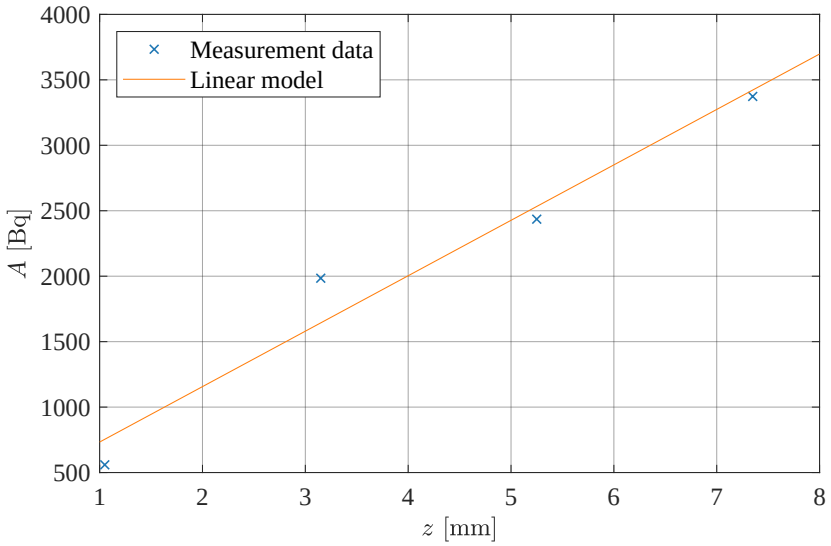

Figure 4.9: Increasing activity with the target thickness in the different VOIs. A linear model is fitted to the data.

Chapter 2.3.1, the positron production and annihilation is not at the same place and the latter one is imaged, but the first one is the relevant information for this study. This results in a smeared distribution is explained in Chapter 4.2.2. The deviations from the fit are in agreement with the assumptions in Chapter 4.2.2. An increasing activity with the target thickness which is not on the linear scale as the target thickness is assumed because of the energy loss in the targets. Due to the several aspects which have an impact on the measurement results, it is not possible to estimate the experimental uncertainties of the activity in each VOI.

A comparison of one quadrant of the acquired spot profile measured using the Lynx PT detector, see Chapter 4.2.1, and from the PET measurement is shown in Figure 4.10. The same lateral dimensions are chosen from the profiles. The uncertainty of the co-linearity is visible in Figure 4.10, as the beam spot is not symmetric which indicates a small shift. The asymmetric shape can be induced by the steps in the target as well. The PET image is a convolution of the spot profile, the spectrum of the positron range which corresponds with the energy spectrum of the positrons from the Fermi function [71] and of the PSF of the imaging system. As a result, the PET image is a smeared spot profile. Additionally, at the edges of the quadrant, an overlap with the other three activation profiles is expected in the activity distribution due to the different target thicknesses. This is not expected for the spot profile measured with the Lynx PT detector.

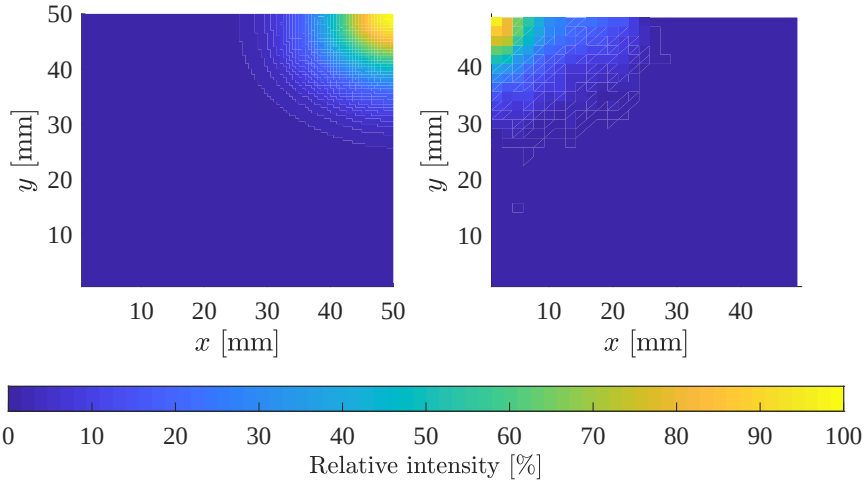

Figure 4.10: Fluence profile of the pencil beam spot (left) and the activation profile from the PET measurement (right). One single quadrant is shown from each profile for comparison.

The uncertainty of the co-linearity and the sample alignment can be derived from the asymmetry in x and y direction of the activity profile shown in the right panel. The spot profile seems to be shifted to the left-hand side of the image. In comparison, the spot profile from the Lynx PT measurement is centered, which is derived from the fit results shown in Table 4.3 in Chapter 4.2.1. Furthermore, the advantage of the pair magnification method with its large dynamic range is visible in the left panel. The spot profile is shown with a width of 20 mm with the clear circular shape while the activity profile becomes noisy in the low signal area. Additionally, the pixel sizes of both images differ by a factor of about three. As the Lynx PT detector has a lateral pixel spacing of 0.5 mm the one of the PET and the chosen reconstruction is about 1.6 mm.

All in all, the activity profile is comparable to the spot profile, which is the main objective of this measurement together with the linear increase of the activity with sample thickness. It is possible to derive a similarity between the activation profile and the spot profile acquired with the Lynx PT. However, it is not possible to derive the exact spot parameters from the lateral activity distribution. This is caused by the low activity in the outer area of the beam spot and asymmetry caused by the steps in the target. With a homogenous target activated with a relatively high number of protons, it might be possible to use the activity measured with a PET scanner to estimate the beam profile with one irradiation over a large dynamic range. A

systematic step as for the Lynx PT detector might not be visible as the homogeneity of the PET scanner can be investigated and corrected with homogeneous radioactive volume. However, the spatial resolution of the PET scanner needs to be measured prior to the experiment as well.

4.3 Discussion of the new reference value

A detailed look on the data measured with the in-beam setup at the WPE and in prior measurements reveals a systematic difference between both results [59]. The difference is covered by the uncertainties of the experimental methods, but it needs to be investigated further. As already mentioned in Chapter 4.1.2, the number of protons per monitor unit has been measured with a FC at the WPE prior to the performed experiments [34, 35]. In contrast, the second study with the in-beam setup has been performed at irradiation facilities prior to the presented study, where the number of protons has been calculated from measurements with an ionization chamber (IC) [59]. Despite this, a new reference cross section is derived from the data with the different measurements and the additional results. It is demonstrated, that the results are consistent between the different measurements and the uncertainties for the measurement methods have been investigated in detail in the past [34].

A detailed literature study reveals that the number of protons can be measured by two different methods. The direct measurement with a FC or the measurement of the absorbed dose with an IC and the subsequent calculation of the corresponding number of protons with the stopping power of the material are used during the experiments [35]. The latter method has been used in referenced work with in-beam setup. The inverse calculation can be used obtain the absorbed dose with the FC measurement. A more detailed study of the literature reveals furthermore a 3% difference between the both methods to determine the absorbed dose has been measured independent from the beam energy [72–75].

At the WPE, a comparative study with a FC and IC has been performed prior to this work. This 3% difference has been obtained as well [35]. Unfortunately, it is still not clear, which results are more reliable. Estimations of the uncertainties for the different methods range between approximately 1.1% for the FC as mentioned in Chapter 4.1.2 and about 2% for the IC based dosimetry following the dosimetry protocol International Atomic Energy Agency (IAEA) TRS-398 protocol for clinical dosimetry [23]. The solutions for the systematic difference is still of interest in proton therapy research [72, 76, 77]. The different FCs used in the studies have been compared in different studies [72]. Furthermore, the beam quality corrections

for ICs which are deduced from MC simulations have been reviewed over time [78]. However, this difference still persists in the latest investigations. The presented study demonstrates that the solution of this systematic difference will subsequently remove the last open issue of the ^{11}C cross section for the production from natural carbon. For now, a potential deviation is covered by the increased systematic uncertainty of the new reference cross section which can be used for further benchmarking of MC codes [79].

The IC based dosimetry has become clinical practice in proton therapy over time [23]. This is associated with several reasons. The different models of FCs developed over time differ in their setup featuring magnetic and electric fields to improve the performance and the setup of a FC is more complex [72]. The IC based dosimetry is much easier to handle in clinical routine work and its commercial availability and calibration possibilities at standard laboratories are the main advantages for the clinical routine work. These aspects improve comparability of different radiation therapy centers, and enable clinical studies across the different centers [72, 80].

However, there are some reasons, to rely on the FC measurements for nuclear physics experiments. A first reason is the usage of FC based proton beam monitoring for activation studies in the past [53, 81, 82]. The FC has been used in the first experiments aiming the measurement of nuclear activation cross sections of carbon and have subsequently been substituted by carbon activation monitor foils [55]. As a consequence, many other cross sections have been measured relative to the cross section of the production of ^{11}C from natural carbon. Furthermore, the charge which can be converted in the number protons with the elementary charge is the measured objective during the FC measurement. In contrast, the IC based method uses calculations with the stopping power of the used material [35]. An additional uncertainty is introduced by the stopping power.

The new reference cross section of (68 ± 3) mb is calculated from the measured cross sections at a proton beam energy of (97 ± 3) MeV. The energy value is chosen from the energy loss in the different targets and covers the proton beam energy within the targets. For comparison with cross sections from previous studies an energy spread is supposed to be comparable in the same energy range. At first, two further publications from the past, interestingly the oldest ones, have measured a cross section similar to the ones measured for the thinnest targets of about 70 mb [53, 54]. A small decrease of the measured cross sections with increasing $z\rho$ comes with increasing experimental uncertainties and as shown with the additional PET measurement this effect might be an artifact of the different corrections which need to be applied. As a result, it should be mentioned, that the thinnest possible targets should be used for cross section measurements. However, the thickness of the targets

is a tradeoff of the useability and expected count rate on the one and the influence of the target on the beam on the other hand.

The current gold standard for the $^{nat}C(p,x)^{11}C$ cross section of Kavanagh et al. [81] at an energy of 98 MeV is in agreement with the lower curve of the cross sections listed in the data base which proposes a cross section of (63.3 ± 0.3) mb. This value has been confirmed by several other groups over time. However, a detailed analysis of the literature reveals, that not all of the prior studies have measured the absolute cross sections. Many of the studies used a relative measurement at one single energy to normalize the cross sections on this reference energy. As a result, the agreement with one of the different curves is given by the experimental method itself. In conclusion only a small number of studies have worked on absolute cross section measurements.

Interestingly, in the energy range around 100 MeV only two of the measurements from the past have measured absolute cross sections [54, 81]. All further studies have been performed with a normalization on one of the two prior studies. The most recent experiments aimed to investigate the absolute cross sections [34, 57–59].

The prior gold standard with the used proton energy motivates the used energy in this study. The treatment machine of the WPE with its 230 MeV cyclotron and the degrader system is limited to 100 MeV minimal incident beam energy. Additional absorbers upstream of the target might be used to reduce the energy further, but two objectives reject the use of these absorbers. The beam properties are changed in the absorber and the precise beam characteristics from the clinical work cannot assumed for the measurements. Furthermore, the beam is degraded in thicker targets as well. Thus, the energy spread of the beam increases in the target depth. Additionally, the profile is broadened by multiple scattering reactions. All in all, this method would be associated with an increasing uncertainty for the beam energy and cross section itself.

The cross sections in the energy range from 85 MeV to 115 MeV are shown in Figure 4.11 [34, 53, 54, 56, 59, 81–84]. The different experimental uncertainties for the studies over time are visible as well as the agreement of the reference cross section with the upper curve of the cross section data from the literature. With this new reference cross section, the complete excitation function can be rescaled on the new reference value [61]. As many literature data refer to the same reference cross section from Kavanagh et al. [81] a rescale is easily possible.

As already mentioned, many other cross section data which have been measured relative to the carbon activation need to be rescaled as well, as the carbon activation has been used to determine the number of incident protons [55]. Moreover, the study reveals limitations of thick targets for cross section measurements. Thus, the prior

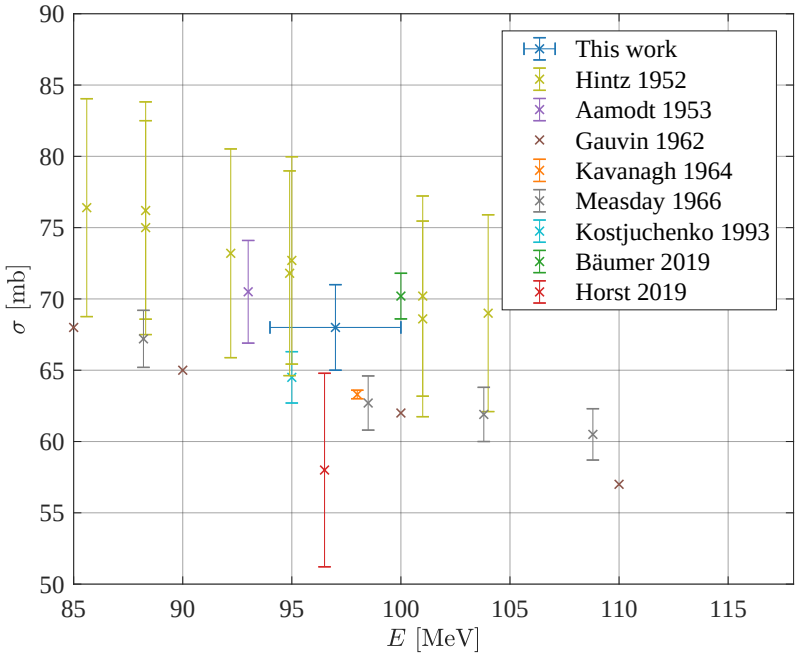

Figure 4.11: The proposed reference cross section is compared to the several data from the literature. Further values can be found in the literature, but they are below or above the shown energy range [34, 53, 54, 56, 59, 81–84].

studies featuring so-called foil stacks to measure the cross sections at different energies with one single irradiation might be re-evaluated regarding potential increasing uncertainties with the depth in the foil stack [57]. For application in clinical proton therapy, the production of ^{11}C is relevant if post-fractional PET imaging is implemented for in-vivo dose verification [3, 8]. A correct implementation of the cross sections in the simulation of the expected activity distribution is crucial if the absolute dose and not only the range is an objective of the treatment verification. Therefore, the first measurements of the complete excitation function in the therapeutic energy range are investigated [85].

5 Determination of activation cross sections for contrast agents

In order to increase the signal of post-fractional PET images, contrast agents with high cross section at the end of the beam range might be useful for field verification. Common contrast agents for conventional CT are iodine based pharmaceutical drugs which are used to increase the X-ray attenuation in specific tissues [86]. As there are many positron emitters produced from iodine with high cross sections at the 1 b-level [37], and several further radionuclides emitting gamma-rays are produced during proton beam irradiation, the activation of iodine by high-energy proton beams is investigated. The iodine nuclei with high cross sections in the target area would potentially increase the PET signal. Targeting of the contrast agent to specific structures would allow for monitoring of these structures. Basic physics investigations on the activation of iodine are discussed in this chapter. This measurement is necessary to estimate the potential clinical application. However, further physics, medical and bio-chemical investigations might be necessary to comment on the overall clinical applicability. From physics point of view, detailed measurements of activation cross sections from iodine might be necessary for the clinical application as discussed for the $^{nat}C(p,x)^{11}C$-cross section in Chapter 4.

5.1 Experimental setup

To simplify the handling of the target, caesium iodine (CsI) is used as target material. CsI is a powder and for the handling of the target material, it has to be collected in a closed cavity. Therefore, the CsI powder is filled in a 3d-printed sample holder designed by D. Sánchez-Parcerisa et al. [87]. The sample holder is shown in Figure 5.1. The cavity of the target holder has a lateral size of (29.49 ± 0.05) mm $\times$ (30.15 ± 0.05) mm and a thickness of (1.99 ± 0.05) mm and is filled with (4.716 ± 0.001) g of CsI. Then, the cavity is sealed airtight with a plug.

The study is part of a joint experiment and the analysis of the gamma-ray spectrum of activated CsI sample is discussed in this chapter. The target is irradiated in the FBTR at the WPE with a scanned PBS field of 5.25 cm $\times$ 5.25 cm which is discussed in Chapter 4.1.2. In the concept of the joint experiment, the incident

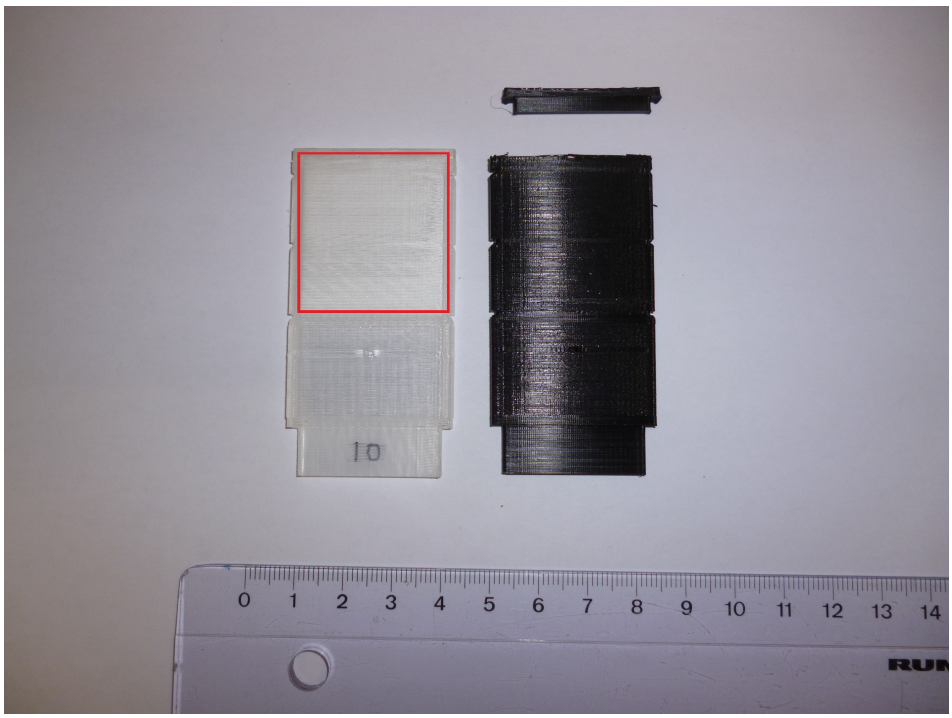

Figure 5.1: 3d-printed sample holder. Filled target holder (white, left) with the filled cavity (upper ²/₃ of the holder, red box) and reprinted target holder to measure and visualize the geometry (black) with plug [87]. A ruler is shown for comparison.

beam energy is 200 MeV for the target which is measured with the setup in the beam line and in the DLB. During the joint experiment several targets are irradiated and the activation is observed with a four detector setup directly at the beam line. Therefore, the targets are placed at the isocenter in the center of the four detectors perpendicular to the beam axis [87, 88]. Subsequently to the irradiation with 20 MU ($\Phi = (9.80 \pm 0.10) \times 10^7/\mathrm{cm}^2$), the activation is measured with the in-beam setup. After the data acquisition, the target is brought to the DLB.

At the DLB, the target is placed directly on top of the detector end-cap with the irradiated area parallel to the detector surface. A time-resolved gamma-ray spectrometry measurement is performed over 19 d. The time resolution depends on the time after the irradiation and ranges between 2 min for the first day and 1 h after three days, which allows for a decay analysis of the identified gamma-ray peaks. This is crucial, as many radionuclides with similar gamma-ray energies are expected to be produced during the irradiation.

5.2 Gamma-ray analysis and determination of activities

Compared to the activated graphite sheets presented in Chapter 4, a large number of peaks are visible in the gamma-ray spectra measured over the measurement time. The several gamma-ray peaks have to be assigned to the various radionuclides produced in the target material. Therefore, an iterative process is necessary, because many radionuclides with similar energy levels are produced during the proton irradiation. At first, potential candidates are assigned to the peak energy and an exponential model is fitted to the net count rate over time to verify the half-life of the radionuclide. Second, the various other gamma-ray energies of the candidate nuclide are checked regarding their visibility in the spectrum in comparison to their emission probability [37]. A gamma-ray energy with a higher or similar emission probability compared to the peak under investigation has to be visible in the gamma-ray spectrum as well, to confirm the candidate nuclide. The gamma-ray spectra acquired over time are shown in Figure 5.2.

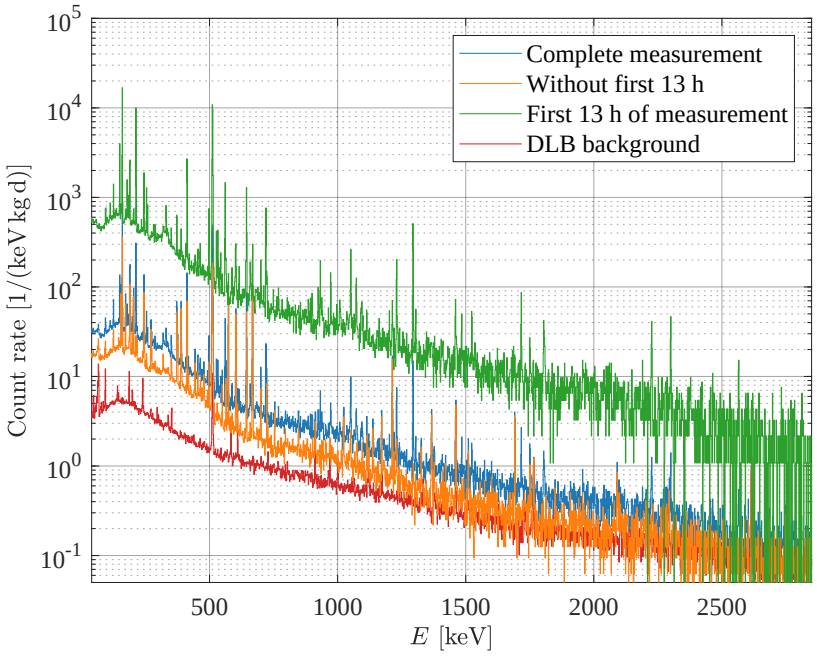

Figure 5.2: Gamma-ray spectra for different time intervals of the activated CsI sample. The first 13 h (green) show a relatively high activity. The measurement without these first hours (orange) reaches the background level (red) for energies above 1500 keV.

However, not all peaks in the spectrum are full energy peaks. For all peaks with an energy above 1022 keV, SEPs and DEPs can be identified in the spectrum. In addition, coincidence peaks can be found in the spectrum. These peaks can be observed, if more than one photon deposits its complete energy in the active detector volume within the time resolution of the detector and read-out system. As the DLB is designed for radio-purity research [40], samples analyzed with the detector system have relatively low activities compared to samples produced during proton irradiation. This results in more coincidence events in activated samples than in radio-purity research samples.

Table 5.1: Energy peaks in the gamma-ray spectrum used for the analysis of each radionuclide, the exact values of the energies are taken from the database [37]. The half-life added to the table is the one used from the literature [37]. (1) indicates radionuclides contributing to the annihilation peak (AP).

radionuclide	$T_{1/2}$	E_γ [keV]
^{128}Ba	(2.43 ± 0.05) d	273.44
^{131}Ba	(11.5 ± 0.06) d	123.804, 216.088, 496.321
^{131m}Ba	(14.6 ± 0.02) min	108.45
^{125}Cs(1)	(46.7 ± 0.1) min	526.0
^{127}Cs(1)	(6.25 ± 0.1) h	287.16, 462.31, 587.01
^{129}Cs(1)	(32.06 ± 0.06) h	371.918
^{119}I(1)	(19.1 ± 0.4) min	257.52
^{121}I(1)	(2.12 ± 0.01) h	212.20, 532.08
^{123}I	(13.2235 ± 0.0019) h	158.97
^{124}I(1)	(4.176 ± 0.0003) d	602.73, 722.78, 1690.96
^{126}I(1)	(12.93 ± 0.05) d	388.633
^{116}Sb(1)	(15.8 ± 0.8) min	931.84, 1293.558
^{116m}Sb	(60.3 ± 0.6) min	383.0
^{117}Te(1)	(62 ± 2) min	719.7, 923.9, 1716.4, 2300.0
^{119}Te(1)	(16.05 ± 0.05) h	644.01, 699.85, 1413.19, 1749.65
^{119m}Te(1)	(4.70 ± 0.04) d	270.53, 153.59, 912.60, 1212.73
^{121}Te	(19.17 ± 0.04) d	573.139
^{121m}Te(1)	(164.2 ± 0.8) d	293.99
^{123m}Te	(119.2 ± 0.1) d	159.0
^{122}Xe	(20.1 ± 0.1) h	350.065
^{123}Xe(1)	(2.08 ± 0.02) h	899.6, 1093.4, 1113.1
^{125}Xe(1)	(16.9 ± 0.2) h	188.418, 243.378

Once the peaks are assigned to the radionuclides, the activities of the radionuclides can be determined from the net count rate according to the ISO norm [47], as

described in Chapter 3.2.3. If more than one gamma peak is assigned to the radionuclide, the final activity is calculated by averaging of the single activities determined for each peak [43, 47]. For some of the radionuclides, the activities calculated from the single peaks do not match within their uncertainties. This appears for radionuclides which are not dominant in one of the peaks. All analyzed radionuclides are summarized in Table 5.1 with their gamma-ray energies used for the analysis. For 22 radionuclides, activities can be estimated from one or more corresponding peaks. A number of these radionuclides decay by the emission by a positron as an additional decay mode and they are interesting for proton beam range verification with PET. However, for four of the radionuclides, only upper limits can be estimated from the net count rates of peaks. These radionuclides are discussed separately.

For 18 of the radionuclides, activities can be determined, and the decay-corrected activities are summarized in Table 5.2. The half-lifes of the radionuclides range from about 15 min to 120 d. Thus, the selection of an appropriate time interval from the

Table 5.2: Calculated initial activities A_0 for the radionuclides with the gamma-ray energies used for the analysis. The uncertainties of the activity are separated in the systematic (first) and statistical (second). The half-life added to the table is the one used from the literature [37].

radionuclide	$T_{1/2}$			A_0 [Bq]		
^{128}Ba	(2.43	± 0.05	) d	0.073	± 0.002	± 0.010
^{131}Ba	(11.5	± 0.06	) d	0.0156	± 0.0003	± 0.0010
^{125}Cs	(46.7	± 0.1	) min	13.0	± 0.3	± 1.2
^{127}Cs	(6.25	± 0.1	) h	2.66	± 0.05	± 0.20
^{129}Cs	(32.06	± 0.06	) h	0.77	± 0.02	± 0.05
^{119}I	(19.1	± 0.4	) min	33.4	± 0.6	± 2.6
^{121}I	(2.12	± 0.01	) h	12.1	± 0.21	± 0.13
^{123}I	(13.2235	± 0.0019	) h	4.77	± 0.09	± 0.04
^{124}I	(4.176	± 0.0003	) d	0.163	± 0.003	± 0.006
^{126}I	(12.93	± 0.05	) d	0.0628	± 0.0012	± 0.0025
^{116}Sb	(15.8	± 0.8	) min	95	± 2	± 7
^{117}Te	(62	± 2	) min	10.2	± 0.2	± 0.5
^{119}Te	(16.05	± 0.05	) h	1.164	± 0.021	± 0.025
^{121}Te	(19.17	± 0.04	) d	0.0579	± 0.0011	± 0.0021
^{123m}Te	(119.2	± 0.1	) d	0.002 60	± 0.000 05	± 0.000 23
^{122}Xe	(20.1	± 0.1	) h	0.72	± 0.02	± 0.07
^{123}Xe	(2.08	± 0.02	) h	6.2	± 0.2	± 1.4
^{125}Xe	(16.9	± 0.2	) h	1.81	± 0.03	± 0.03

measurement is necessary, to determine the activities correctly, as peaks might be contributed by more than one radionuclide. As the emission probability of the several peaks are very different and for some radionuclides the net count rates are very low, the statistical uncertainties of the activity dominates the overall uncertainty for some radionuclides, as ^{125}Cs. The statistical uncertainties range between the 1%-level for ^{123}I and 10% for several radionuclides like ^{125}Cs. This is associated with several reasons: Firstly, the low number of incident protons compared to the measurements from Chapter 4 result in a lower number of produced residual nuclei. The number of protons is motivated by the expected activity at the end of the irradiation and the optimal performance of the in-beam measurement setup mentioned in Chapter 5.1. Since the DLB is a low-level gamma-ray spectrometry laboratory, it is possible to analyze samples with low activities. For the graphite activation, the experimental parameters have been chosen to reduce the experimental uncertainties [24]. Secondly, the optimization is not possible for all observed reactions at the same time, due to the large number of radionuclides with very different activation cross sections [56].

For the four radionuclides collected in Table 5.3, the determination of the activity results in an upper detection limit with a 95% confidence level. All these radionuclides are meta-stable states and are mainly identified by their excited level and the emission of the corresponding gamma-rays. As the activities are upper limits, the decay is not corrected and no initial activity is calculated for these radionuclides. As the activities are low compared to other radionuclides, these radionuclides will not have any clinical relevance.

Table 5.3: Obtained activities A_{meas} for the radionuclides with the gamma-ray energies used for the analysis. The half-life added to the table is the one used from the literature [37].

radionuclide	$T_{1/2}$	$A_{\text{meas}}^{\text{UL}}$ [Bq]
$^{131\text{m}}$Ba	(14.6 $\pm$ 0.02) min	0.203
$^{116\text{m}}$Sb	(60.3 $\pm$ 0.6) min	0.0204
$^{119\text{m}}$Te	(4.70 $\pm$ 0.04) d	0.004 98
$^{121\text{m}}$Te	(164.2 $\pm$ 0.8) d	0.000 211

In addition to the radionuclides listed in Tables 5.2 and 5.3, more radionuclides can be identified in the gamma-ray spectrum. The two radionuclides ^{132}Cs and $^{120\text{m}}$I are identified with their half-life in the peaks. However, they are not dominant in the peaks. Other radionuclides contribute to the peaks and their decay overlap with the decay of these two radionuclides. As a consequence, the determination of the activity from the net count rate will result in an error. Furthermore, there might be further radionuclides in the gamma-ray spectra which cannot be identified during

the analysis. Additionally, the two radionuclides ^{120}I and ^{127}Xe are identified in one or more gamma-ray peaks by their half-life as a potentially dominant radionuclide. However, during the quantitative analysis of the net peak count rate it is not possible to find a valid activity by averaging the activity with all relevant peaks. This might be caused by the same reason as for ^{132}Cs and ^{120m}I as one of the other radionuclides in the sample might contribute to the peak as well. Due to the number of radionuclides and those with similar gamma-ray energies and half-lifes other radionuclides may overlap in the decay curve of the peaks associated with the decay of ^{120}I and ^{127}Xe. In conclusion, it cannot be identified which of the peaks result in the correct estimation of the activity and in result no analysis of the activity is performed. It can be noted, that these radionuclides are produced during the irradiation.

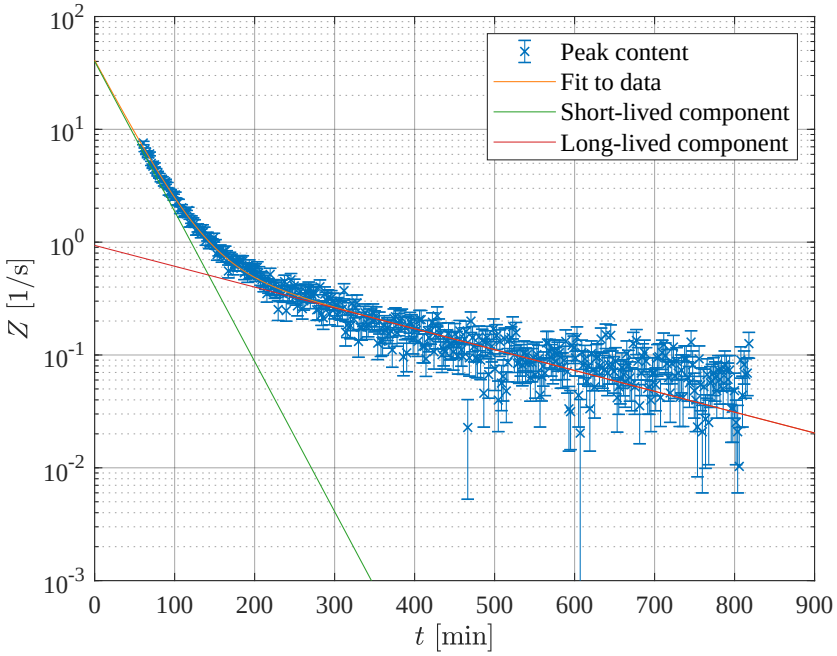

Figure 5.3: Decay rate analysis of the annihilation peak for the activated CsI sample. Only the first measurement interval, the first 13 h is shown. A short- and a long-lived component is fitted to the decay rate over time.

The annihilation peak (AP) at 511 keV would be interesting for PET imaging, a half-life analysis of the count rate in the AP over time is shown in Figure 5.3. A model with two exponential decays is fitted to the data of the first 13 h of the measurement. A short-lived component with a half-life of 23 min and a long-lived

with a half-life of 2.7 h can be fitted to the data. Furthermore, a very long-lived component might be visible in the data starting 600 min after the irradiation. This might be induced by the long-lived radionuclides in the sample. While the short-lived component competes with the decay of the ^{11}C produced from tissue activation, the long-lived radionuclides can be investigated regarding their potential application for field verification. As it is visible, a further long-lived component is underlying the decay and needs to be evaluated regarding a perturbation of the produced activity by the one from prior treatment sessions.

In contrast to the analysis of the ^{11}C-production cross section, investigated in detail in Chapter 4, the AP is not analyzed for this sample. This decision is caused by multiple reasons, which all lead to the conclusion, that an analysis will not provide any further information regarding the question of the usage of iodine as contrast agent for activation in proton therapy. In detail, several radionuclides with similar half-lifes are produced from iodine and caesium during the proton irradiation. Furthermore, all of these radionuclides will have low activities as the number of protons is chosen relatively low compared to the activations performed in Chapter 4. In summary, only radionuclides with additional gamma-ray emissions can be discussed here. These radionuclides are highlighted in Table 5.1.

5.3 Discussion of the activation of CsI

The radionuclides identified in the gamma-ray spectra which decay by the emission of positrons are already marked in Table 5.1. From this list of radionuclides not all radionuclides can be produced from iodine by proton irradiation. As 100% of the natural iodine consists of the nuclide ^{127}I, it can be decided by the number of protons and neutrons in the residual nuclei which of the identified radionuclides potentially can be produced from iodine. This is used as a first decision category [37]. The list of radionuclides is collected in Table 5.4. In addition, ^{120}I is added to the table. For this radionuclide, it is not possible to determine an activity from the gamma-ray spectrum. The two xenon nuclides ^{123}Xe and ^{125}Xe can potentially be produced from ^{127}I by proton capture. The cross section for proton capture at an incident proton energy of 200 MeV for these reaction is taken from the EXFOR database. While the production cross section of ^{125}Xe scatters between 10 mb and 50 mb among the different literature sources, the data for ^{123}Xe are sparser [56]. The cross sections for the productions from caesium are in the same range. However, the production from caesium seems to be more probable as the production is not limited to the capture of proton, and subsequent emission of one or more neutrons. For this work, it is not possible to separate the productions from iodine and caesium. The analogous investigations can be done for the other radionuclides.

Table 5.4: Overview on the radionuclides which can potentially be produced from iodine and subsequent decay by the emission of a positron.

element	radionuclides
I	^{119}I, ^{120}I, ^{121}I, ^{124}I, ^{126}I
Sb	^{116}Sb
Te	^{117}Te, $^{119(m)}$Te, ^{121m}Te
Xe	^{123}Xe, ^{125}Xe

For the two radionuclides ^{120}I and ^{119}Te, the cross sections listed in the data base are in the same magnitude. However, some of the cross sections are associated with relatively large uncertainties [56]. Furthermore, for ^{121}I, the cross sections from the production from iodine scatter, which results in the consequence, that it is not possible to decide if the once for the production from iodine are larger or not. The three radionuclides ^{124}I, ^{126}I, and ^{121}Te have production cross sections which are larger by a factor of 10 for the production from iodine compared to the one from caesium. At last, for the radionuclides ^{119}I, ^{116}Sb, and ^{117}Te no data can be found in the database at the energy of interest. Furthermore, in the database it is not differed between the ground state and the meta-stable state, which leads to further uncertainties for the interpretation of the literature data.

Prior to the transfer of iodine as a contrast agent for field verification, different limitations have to be investigated. At first, the uptake in the tissue in the irradiated part of the body and the surrounding tissue has to be investigated further. As it is commonly used for other contrast agents or radio-pharmaceutic drugs, iodine-doped bio-molecules seem to be the favorable implementation. Once, the iodine contrast agent is absorbed in the cells, it needs to stay for the needed time window in the cells without a significant transport. This would avoid the biological wash-out known from the literature for the tissue activation [8]. It is shown in Chapter 6 that the tissue activation covers the implant activation for about 2 h. Except of the half-life of ^{119}I with about (19.1 ± 0.4) min [37], the physical half-life of the iodine radionuclides would be large enough under the condition that the biological half-life is large enough as well. The short-lived radionuclides may compete with the decay of ^{11}C produced from the tissue nuclei. However, the long-lived radionuclides might be helpful for the clinical application, as it is discussed further in Chapter 6. As the longest half-life of the iodine radionuclide ^{126}I is (12.93 ± 0.05) d [37], the iodine should not be kept too long in the cells. As a radiotherapy treatment mostly features 30 treatment sessions with five sessions per week, more radioactive iodine would accumulate in the cells over time. This limits the potential of iodine activations as field verifications for plan adaptions during a treatment over several weeks.

Furthermore, the thyroid is the organ for the iodine metabolism in the physiological processes [89]. Therefore, an iodine storage is kept in the thyroid. As the thyroid is a potential radio-sensitive organ, it should be avoided, that the radio-activated iodine is stored in the thyroid subsequent to the removal by the metabolism from the irradiated tissue. In civil protection, iodine drugs are given to the people in case of an incident at a nuclear power plant [90]. This should avoid the uptake of radioactive iodine from the power plant because enough iodine is kept in the thyroid prior to the potential exposure to the radioactive iodine. The potential cause of secondary thyroid malignancies has to be investigated prior to any clinical application of iodine as a contrast agent.

As already discussed, the cross section data in the database are sparse for some reactions [56]. During this work, no cross section data can be added to the database. In general, the calculation of cross section using gamma-ray spectrometry subsequently to proton irradiation is complex and limited to a small number of produced radionuclides if a target consists of more than one element, like CsI or BN in the literature [91]. For this purpose, it is not possible to separate the radionuclides by their origin during the production process. Many of the radionuclides identified in the spectra can be produced from caesium or iodine. Due to the number of protons and neutrons in the target nuclei (caesium has a higher Z than iodine) all radionuclides produced from iodine can potentially be produced from caesium as well. To overcome this limitation, a substitution of the caesium by potassium or sodium might be helpful for cross section measurements, as many of the radionuclides cannot be produced from the relatively low-Z atoms potassium or sodium as a number of proton captures per target nucleus are necessary.

Even for a pure iodine target, gamma-ray spectrometry would be difficult for the cross section determination as the spectrum for pure iodine target would contain many peaks as well. Other methods to quantify the number of produced residual nuclei would potentially be favorable, like chemical separation methods, which have been used in the past as well. A method without a potential perturbation of residuals with similar properties is crucial for accurate measurements of the activation cross sections on iodine.

With the current situation of the data at higher energies for proton therapy, a validation and benchmarking procedure for the iodine-based field verification is necessary including all clinically applied techniques. An exemplary benchmarking procedure for titanium implants is described in Chapter 6. However, this method has to be adapted to the properties of the contrast agent-based method of field verification.

6 Activation of titanium implants in proton therapy

In clinical proton therapy, an accurate treatment planning and patient irradiation is required to use the advantages given by the depth dose distribution discussed in Chapter 2. In order to monitor the treatment fields during and subsequent to the treatment, different techniques have been developed in the past [3, 4]. However, for the PET imaging to visualize the activation of the tissue for treatment monitoring, the limitation of the biological transport processes has been observed in the past [8].

In order to overcome the limitation of off-line (out-of-room) post-fractional PET imaging for treatment verification, implanted markers have been proposed to be a possible solution [10, 11]. As implanted markers keep their position in the patient over time, the produced activity is not subjected to the biological wash-out. The nuclei in the implants do not participate the metabolism.

In a gamma-ray spectrometry measurement of an activated titanium sheet, a dominant peak which stems from the electron positron annihilation is identified and associated to the several radionuclides emitting positrons during the decay process [13, 92]. A half-life analysis of this peak reveals a short-lived component (green curve) and a long-lived component (red curve) in the decay as shown in Figure 6.1. While the decay of the short-lived component is competing with radionuclides produced from tissue nuclei, the long-lived component would contribute to long-lived signal in post-fractional PET imaging. While the count rate in the peak from the annihilation process becomes dominated by the long-lived component about 2 h after the irradiation, where the short-lived component reached approximately 1% from the overall signal. This time would be shifted to a later point in real scenarios, as the tissue activation would suppress the signal from implant activation for the first time after the irradiation as the tissue activation results in a higher activity compared to the phantom activation.

In the first proof-of-principle studies, a slanted angle phantom was irradiated with relatively high dose of 30 Gy and subsequently analyzed in a small animal PET [12, 93]. As these settings are far away from clinical requirements, the expressiveness of the study is limited. Several phantoms were irradiated with doses more comparable to clinical settings, which are about 2 Gy(RBE) as fractional dose [70, 94]. The study

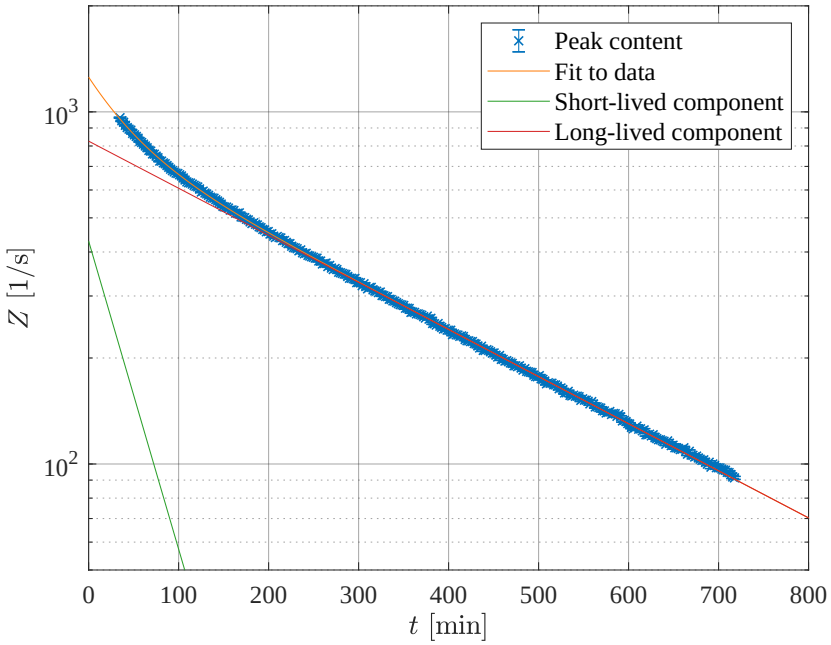

Figure 6.1: Count rate in the AP in the gamma-ray spectrum of an activated titanium foil. A double exponential decay curve (orange) featuring two different half-lifes is fitted to the data (blue). The short-lived component (green) is competing with the tissue activation, while the long-lived component (red) would lead to a signal which is only sensitive to the implant activation. Further analysis of the data from [92].

features an anthropomorphic phantom and a phantom consisting of five PMMA slices with titanium implants, which is discussed in detail in Chapter 6.1 and called slice phantom.

All prior studies investigated the general possibility of the use of titanium implants. Ongoing from the results, the sensitivity of the proposed method is investigated further in this study. The study is divided in two different steps: At first, the sensitivity of the method is evaluated with the slice phantom. In a second part, a multi-field irradiation is tested in a more clinical setup with an anthropomorphic phantom. To quantify the sensitivity of the method, two main objectives are investigated. The sensitivity is meant to be the range accuracy and the verification of the absolute dose. According to the commonly used uncertainties in proton therapy, the range sensitivity should be able to detect deviations of 2 mm as the commonly used safety margin for head irradiation is 3 mm and an absolute dose

verification of 3% would be favorable for radiotherapy treatments [6]. The tests are called pre-clinical validation.

6.1 Development of the slice phantom

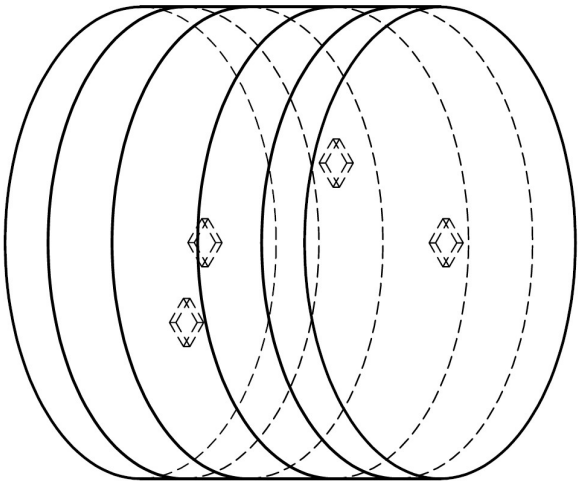

Figure 6.2: Part of the technical drawing of the slice phantom with the five PMMA slices and four titanium inserts. The complete technical drawing is shown in Figure A.7. The proton field is applied from the left-hand side.

The detailed development of the phantom has been performed during a Master thesis project [70]. This phantom is called "slice phantom" in this study and the cylindrical geometry can represent the simplified geometry of a human head. The slice phantom is shown in Figure 6.2 and consists of five disks of PMMA with a diameter of 18 cm and are manufactured from the raw material which is clinically used for the range compensators for US and DS patient treatment at WPE. The five discs have thicknesses of each two of 2 cm and 3 cm and a fifth one of 4 cm. The thickest one is the center disk and the other disks are arranged with decreasing thickness from the center to the outside. Four of the five disks feature cavities for small titanium tiles with lateral dimensions of about 13 mm × 13 mm and a thickness of 3 mm. The implants are placed with a distance of 1.5 cm in both directions along the implants from the central axis with the closest corner of the square. The distance between the implants should avoid an influence from one implant among each other. The cavities for the implants are placed in the upstream surface of the second to fifth disk of the phantom.

Because of the simple geometry, this phantom is favorable for use in simple MC simulations and is used for the further investigations in the presented study. In contrast, due to the geometry of the phantom, it is limited to the irradiation from the top (or bottom) side of the cylinder. The cylindrical shape is caused by the one of the raw material. Furthermore, the parallel surfaces allow for reproducible alignment on the treatment table.

6.2 Setup of a pre-clinical validation

The study which is presented in this chapter can be understood as a pre-clinical validation. The test is more a pre-clinical test as only phantoms are used in the study. Furthermore, the tests should investigate the several potential applications of the radioactivation of titanium implants. The comparability of pure titanium and titanium alloys has been shown in a previous study [13].

6.2.1 Experimental investigations with the slice phantom

The general objective of this study is the investigation of the possibility to identify deviations between treatment plan and field delivery. An initial treatment plan is varied in the range of the proton beam and the delivered dose to investigate these two main objectives. As already for the cross section and activation measurements in Chapters 4 and 5, the PBS irradiation technique is chosen for these measurements.

To perform the test, the clinical workflow for treatment planning is performed with the phantom. A planning CT is acquired with the clinically used Philips Bigbore CT system (Philips Medical Systems, Hamburg, Germany). The clinical settings for CT scans of heads is used for imaging. The reconstructed images are loaded in the clinical TPS RayStation Version 10B (RaySearch Laboratories, Stockholm, Sweden) [95]. The PMMA of the phantom is not consistent with the clinically used CT calibration curve [96] and the images contain artifacts from the sharp edges of the titanium implants. The phantom itself and the implants are contoured with their exact dimensions. With the accurate knowledge of the dimensions of the phantom, it is possible to have a digital model of the phantom. Subsequently, the CT values are overwritten with their densities. In consequence, the artifacts in the images do not disturb the predicted dose distribution.

The definition of the target volume in clinical practice is to define the clinical target volume (CTV) which is the known tumor volume from the imaging and further information on the tumor type. To account for the different uncertainties a safety margin is used to define the planning target volume (PTV) as an expansion of the

CTV. This method ensures to deliver the necessary dose to the whole tumor volume. For the current study, it is easier to define the PTV first and create the CTV as the contraction of the PTV. The PTV covers the projections of all four implants on the lateral field shape. In beam direction, the PTV is created with dimensions that the proton beam is stopped upstream of the last implant and the second implant is not in the plateau area of the dose distribution. According to the WPE standard, the CTV is a contracted volume of the PTV with a uniform contraction of 3 mm.

The treatment plan for the phantom has one irradiation field directing on one of the circular surfaces of the cylindrical shape of the phantom. The thinnest possible clinically used RS with a water equivalent thickness (WET) of 25 mm is used for

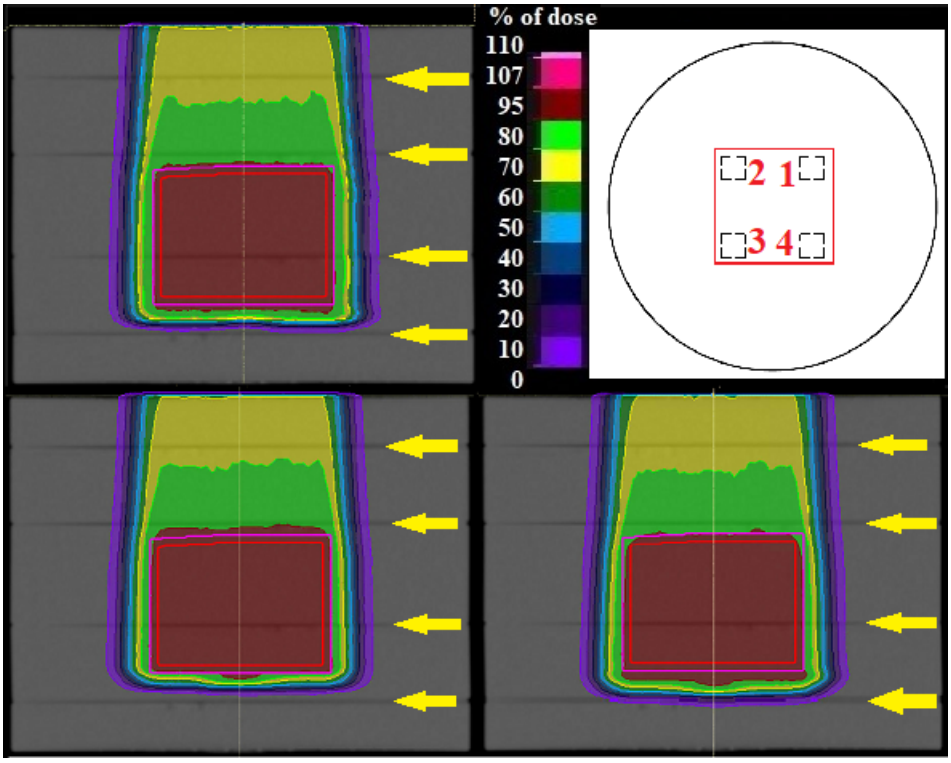

Figure 6.3: Comparison of the dose distribution of the three treatment plans. The initial treatment plan (upper left), the ones shifted to lower ranges (lower left) and to higher ranges (lower right). The initial target volumes (CTV, red and PTV, pink) are shown. The relative isodoses refer to the prescribed dose of 2 Gy(RBE). The slice in the middle of the phantom is shown, the height of the cylinder is the vertical direction of the image. The implants are not visible but placed between the disks of the phantom (yellow arrows). The lateral field orientation is shown on the upper right (red square) with the implant numbers (red numbers).

the treatment field to cover the complete target volume with the prescribed dose. A dose of 2 Gy(RBE) is prescribed as the median dose to the PTV. The treatment plan for the FBTR beam line is optimized with the RayStation Plan Optimization tool as a robust treatment plan against positioning and range uncertainties [95]. The common settings for head irradiations at WPE with a uniform position uncertainty of 2 mm and a density variation of 3.5% is used for the treatment planning. The plan is optimized on the CTV. As a result, the plan fulfills the common criterion for a treatment plan as 95% of the PTV is irradiated with 95% of the prescribed dose [6]. Once, the initial treatment plan is optimized, the PTV and CTV are shifted by 2 mm up- and downstream in the phantom and for each of the shifted target volume, a new treatment plan is optimized with the same settings but optimized on the corresponding shifted volumes. A projection of the corresponding dose distributions is shown in Figure 6.3. Only the initial target volumes are shown in the figure. The shift of the high dose region is visible in the dose distribution. Especially, for the distal implant variations in the activation are expected to result from different irradiations.

The treatment plans on the different shifted target volumes represent the possible over- or undershoot [5]. As all three treatment plans are optimized robustly with the common clinical settings, the dose volume histograms (DVHs) reveal that the coverage of the initial CTV is still achieved by the plans optimized on the shifted target volumes. This is given by the robustness settings in the optimization settings for the three plans which account for the uncertainties simulated by the shifted targets. The virtual uncertainties introduced by the shifted volume should be covered by the settings. The DVHs of targets and implants are visualized in Figure 6.4. From the DVHs can be derived, that the dose deposited in the implant in the high dose region does not change. However, the dose distribution in the entrance plateau and downstream of the virtual target are influenced by the shift of the high dose region.

In addition to the plans optimized on the shifted target volumes, the dose of the initial treatment plans is scaled by 3% to 2.06 Gy(RBE) and 1.94 Gy(RBE), respectively. In summary, five different treatment plans are used for the validation. The five irradiations are performed at the clinical beam line in the FBTR. The phantom is aligned on the treatment table with the isocenter at the planned position. The plans are irradiated and subsequently, the phantom is brought to the PET scanner. During the PET acquisition, a ^{22}Na source is mounted on the downstream circular surface of the phantom which is not activated. With this reference source, it is possible to monitor the reproducibility of the PET scanner over the measurement campaign. To increase the efficiency, the point source is placed in a PMMA absorber.

A Siemens Biograph Vision ToF-PET system (Siemens Healthineers, Erlangen,

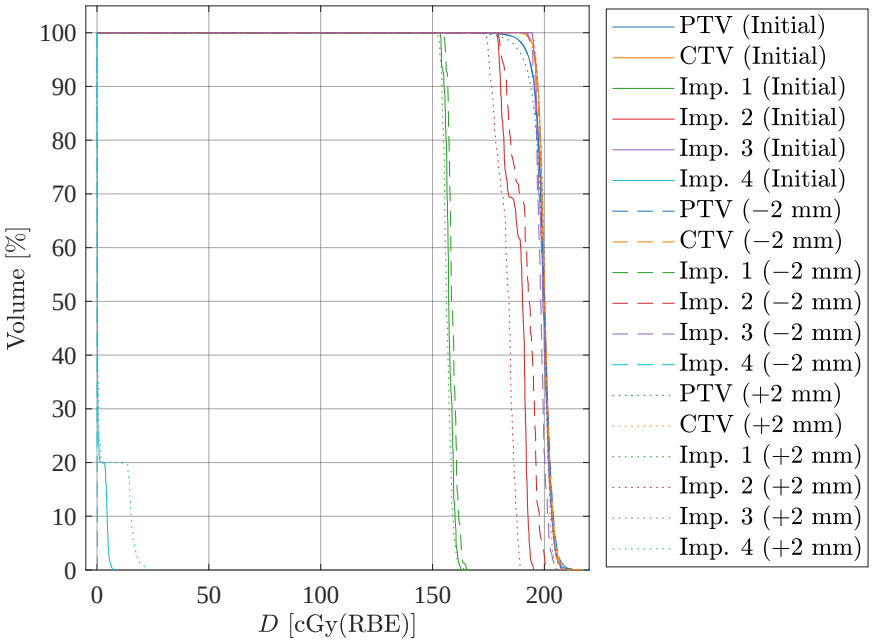

Figure 6.4: Comparison of the DVHs for the target volumes (PTV and CTV) and the four implants in the slice phantom. The initial treatment plan is shown as a line, the plan manipulated by +2 mm range is doted, the one by −2 mm is dashed.

Germany), as in Chapter 4, is used for the measurements. A protocol for ^{22}Na is chosen for the decay correction during the measurements. Because of the half-life of ^{22}Na of 2.6018 a, no correction is applied during the measurement. The emission probability of ^{22}Na is used for the reconstruction instead of the correct one for each radionuclide. In the analysis, the measured activities need to be corrected for the emission probability of ^{22}Na.

The data acquisition time of the PET is 4 h. According to the mentioned reasons in Chapter 2.3.1, an OSEM-based reconstruction with the ToF information is chosen for the image reconstructions. With the results from the pre-studies, the PET images are reconstructed in intervals of 5 min. Additionally, the last three 30 min intervals are reconstructed as complete stacks as well. These 30 min images should be representatives for possible clinically used images. In summary, 48 PET frames with each 5 min and three frames with a measurement of 30 min can be used for the analysis. The CT scan is performed after the PET acquisition which is a basic difference compared to diagnostic PET imaging to keep the time between data

acquisition and irradiation as short as possible.

6.2.2 Simulation study

As the basic concept of treatment verification bases on two steps, the imaging on the one hand, and the comparison of the measured activity with a MC prediction on the other hand, a simulation study is included in the validation. To predict the activities of the implants, the energy spectrum of the protons is scored by the MC simulation and subsequently, the activity is calculated with the cross sections from the EXFOR database [56].

The simulations are performed in TOPAS, an extension for particle therapy physics for the simulation toolkit Geant4 [46]. The TOPAS version 3.6.1 is used for the simulation study [97]. The phantom is set up basic shaped geometries. Based on the treatment plans from RayStation, the TOPAS particle sources are generated with bi-Gaussian spot profiles with their energy-dependent width and positions with the emittance particle source [68]. The simulation includes the RS from the treatment plan with the distance from the phantom as in the treatment plan.

On the upstream surface of the four implants, the proton energy spectrum is scored in 1 MeV bins. The bin width is chosen with the different intervals between the single cross section measurements for the production cross sections listed in the EXFOR database [56]. While some cross sections are measured with relatively low energy steps, sometimes, the data points are several MeV apart. The different energy ranges among the different literature source require an interpolation of the data and introduce a new regular spacing of 1 MeV.

Concerning all pencil beam spots, the simulation covers 10^9 protons. The weights of the different spots in the simulation are chosen with their corresponding spot weights in the different treatment plans. For the simulation study, three simulations are necessary, as the dose increases linear with the number of protons. In result, no additional simulations are necessary for the dose variation and the resulting spectra can be scaled with the same scaling factor. Only for the range variation, the simulations need to be performed. The linearity between the MU and the dose is part of the clinical quality assurance.

For the simulation, the six Geant4/TOPAS physics lists, G4EMStandardPhysics_option4, HadronPhysicsQGSP_BIC_HP, G4DecayPhysics, G4HadronElasticPhysicsHP, G4StoppingPhysics, and G4IonBinaryCascadePhysics, are used as the beam model has been optimized with this parameters and demonstrate a good agreement with other MC predictions [68]. Furthermore, the default production cut of 0.05 mm is sufficient for the application, as the energy threshold for the nuclear interactions

of interest discussed in Chapter 6.3.2 is about 5 MeV [56] and the production cut corresponds to an residual energy of about 2 MeV in titanium [19]. For the other materials in the phantom, PMMA, the energy threshold is lower as the density is lower. A residual energy below the energy threshold for nuclear interactions affects not the activities predicted with the cross sections as they are zero below the energy threshold.

6.2.3 Irradiation of an anthropomorphic phantom

While all irradiations covered in the previous studies [70, 93] feature one single irradiation field, clinical treatment plans mostly make use of a multi-field concept. This should reduce the entrance dose of the different treatment fields further as well as the increasing effectiveness of the irradiation close to end of range induce side effects of the radiation treatment [21, 22].

This part of the validation is to compare a single field with a multi-field irradiation as it is used in clinical scenarios. Therefore, six rods of titanium are placed in an anthropomorphic 5-year child phantom (Computerized Imaging Reference Systems (CIRS) Inc., Norfolk, United States). The rods have the same dimensions as dosimeter rods used for dose verification with the phantoms, a diameter of 3 mm and a length of 25 mm. The rods are placed in the head region of the phantom. Four in one of slices around a virtual target volume and two more in one and two slices below. While the first one is in the lateral gradient of the dose distribution, the second one is not within the irradiation field.

As the procedure for the slice phantom, a CT imaging with a head protocol is performed for treatment planning and the implants and artifacts are contoured and overwritten with the correct density in the treatment planning system. As the chemical composition of the phantom materials representing the soft tissue, brain, and bone is known, they are contoured in the phantom as well and overwritten with their exact material properties. Furthermore, some organs at risk have been contoured for a prior study and are used here. The exact positions of the implants in the head and their positions compared with the target volumes are shown in Figure 6.5.

The virtual target volume is a sphere placed between the four titanium rods in the same slice of the phantom. As for the activation of the slice phantom, a PTV and its corresponding CTV are contoured with a margin of 3 mm. A PBS plan is set up with two treatment fields, a lateral field and one field from posterior. Due to the geometrical limitations of the phantom, the phantom is positioned in supine position and the head sticks out over the table edge. A clinical positioning of this

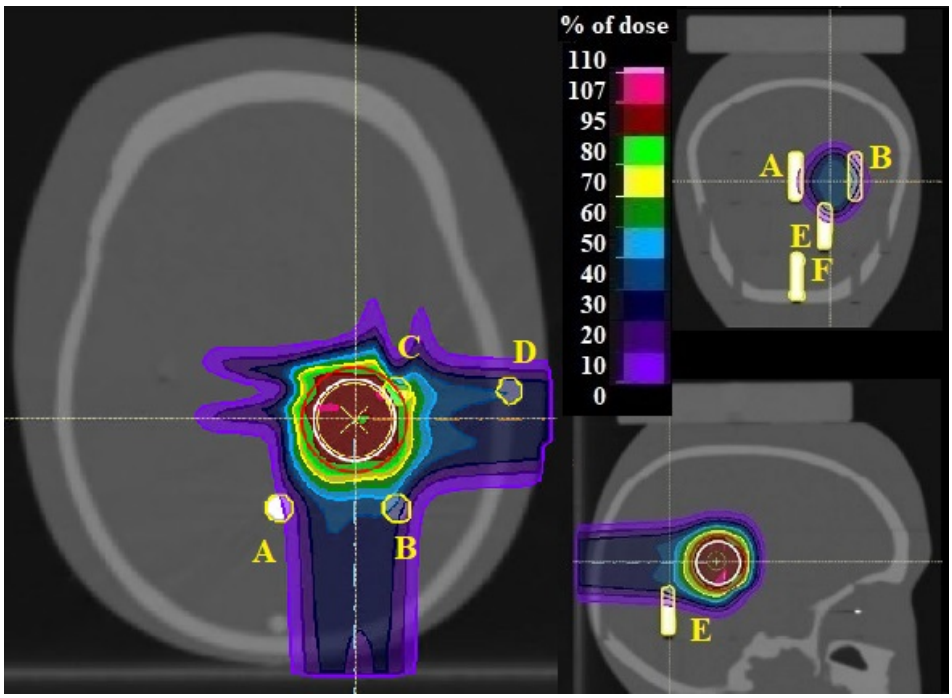

Figure 6.5: Implant positions and PTV (pink circle) and CTV (white circle) with the planned dose distribution for the anthropomorphic phantom in the TPS RayStation. The three different slices are chosen to localize all implants with their relative position to the target volume. The yellow letters indicate the implant numbers for the analysis.

patient would be the prone position. However this is not possible due to the rigid properties of the phantom. Furthermore, in clinical settings, a vertex like field would be planned for the irradiation which is not possible for the phantom due to the fixation screw of the phantom. The limitations of the phantom leads to a beam stopping proximal to the brain stem which is avoided in clinical practice because of the increasing RBE close to end of range of the proton beam [22].

All in all, the treatment plan setup represents the general settings of a two-field geometry which is a possible clinical geometry. As for the slice phantom, the treatment plan is optimized in RayStation 10B with common clinical settings for robustness [95]. The plan is optimized on the CTV and the prescription to the PTV is the median dose of 60 Gy(RBE) in 30 fractions of 2 Gy(RBE). However, only one fraction is delivered to the phantom. With the prescription, it is possible to compare the dose to the organs at risk (OARs) with the clinical used tolerance tables. In contrast to the treatment plan for the slice phantom, the plan is optimized

for the GTR4 clinical beam line and both treatment fields require a RS with a WET of 51 mm. The beam line is chosen by the equipment prerequisites given by the phantom geometry. The dose distribution of the planning process is shown in Figure 6.5.

The positioning of the phantom in the treatment room is verified with the clinical orthogonal x-ray imaging system. The treatment plan is applied in the same procedure as it is used for clinical patient treatment with a short time between both of the fields. Once the second treatment field is delivered, the phantom is brought to the PET system. The PET acquisition time is 4 h and the data are reconstructed with the same settings as for the slice phantom. After the PET acquisition, the CT image is acquired to keep the time between the PET imaging and the irradiation as short as possible. The calibrated ^{22}Na source is not used for this experiment as it would be favorable for a clinical setting to perform the imaging without an additional radiation source.

6.3 Results of the implant activation

6.3.1 Uncertainty estimation

The uncertainties of the measurements need to be estimated to decide on the significance of the results. According to the calibration certificate (Eckert und Ziegler Nuclitec GmbH, Braunschweig, Germany), the activity of the source has been measured as (38.4 ± 1.2) kBq ($k = 2$) on the 1$^{\text{st}}$ November 2009. With the half-life of ^{22}Na of 2.6018 a [37], an activity of (1.69 ± 0.06) kBq ($k = 2$) is expected for the measurements.

The first step is to estimate the accuracy of the PET scanner. The measured activities are compared with the calibration certificate. For the last three intervals of 30 min per measurement the activity of the source is calculated. In summary, 15 different estimations of the activity can be determined from the measurements. All results are collected in Table 6.1 with their relative deviation from the expected value. The deviations range between -4.8% and 5.3% for the single measurements. In a prior study, a deviation of 5% has been obtained for a 2 h measurement [70]. The 5% are within the clinical acceptable deviations for PET scanners [33]. As PET scanners are not used to estimate absolute activities and only compare the uptake in different tissues the absolute calibration is not relevant. Interestingly, the deviations trend to an overestimation of the activity. The mean activity of all 15 measurements is 1.72 kBq which is 1.8% from the calibrated activity apart and within the 95% confidence interval of the activity from the calibration certificate.

Table 6.1: Measured activities A_1, A_2, and A_3 for the last three 30 min intervals in each PET measurement of the slice phantom with their relative deviation from the calibration certificate of the ^{22}Na source.

meas.	A_1 [kBq]	dev. [%]	A_2 [kBq]	dev. [%]	A_3 [kBq]	dev. [%]
1	1.76	4.1	1.77	4.7	1.72	1.8
2	1.69	0.0	1.63	−3.6	1.61	−4.8
3	1.77	4.7	1.78	5.3	1.76	4.1
4	1.70	0.6	1.75	3.6	1.71	1.2
5	1.72	1.8	1.68	−0.6	1.69	0.0

During a measurement at the DLB, a lower activity as in the calibration certificate has been observed [51]. This is in agreement with the calibration of the PET which is used in a previous study [70]. For the further analysis, the measured activities of the implants are corrected by deviation from the calibrated activity.

A second step is the estimation of the statistical uncertainties. In the literature, the true coincidence rate of the two annihilation photons per activity of the PET scanner has been estimated to $15.6 \times 10^3/(\mathrm{s\,MBq})$ [98] which corresponds to an efficiency of 1.5%. With this, the potential statistical uncertainties of measurements can be estimated. From the activity A, the number of decays contributing to the activity reconstruction and subsequently the number of true coincidences T, the so-called trues, can be calculated with the measurement time t

$$T = 0.015 \times A \times t. \tag{6.1}$$

Subsequently, the statistical uncertainty is estimated as $1/\sqrt{T}$. The estimation in the literature has been done with a line source 10 cm lateral of the central axis. The targets used in the experiments are 1.5 cm away from the central axis. The calibrated ^{22}Na source is a point source and placed nearby the central axis. The phantom is placed in the center of the field of view in axial direction. As the point source is placed in an absorber and placed on the central axis, the efficiency might deviate from the value from the literature.

In order to cross check the efficiency of 1.5% from the literature, the activity of the point source is used to estimate efficiency of the PET scanner. From the activity of the source and the emission probability of a positron during the decay of ^{22}Na, 6.84×10^3 true coincidences are expected according to Equation (6.1) which corresponds to a statistical uncertainty of 1.2%. As each of the five measurements is divided in intervals of 5 min, the activity can be estimated with the 48 single frames. The activity over time in the single frames is shown in Figure 6.6. The mean and standard error of mean is calculated as (1.757 ± 0.011) kBq. This is an uncertainty

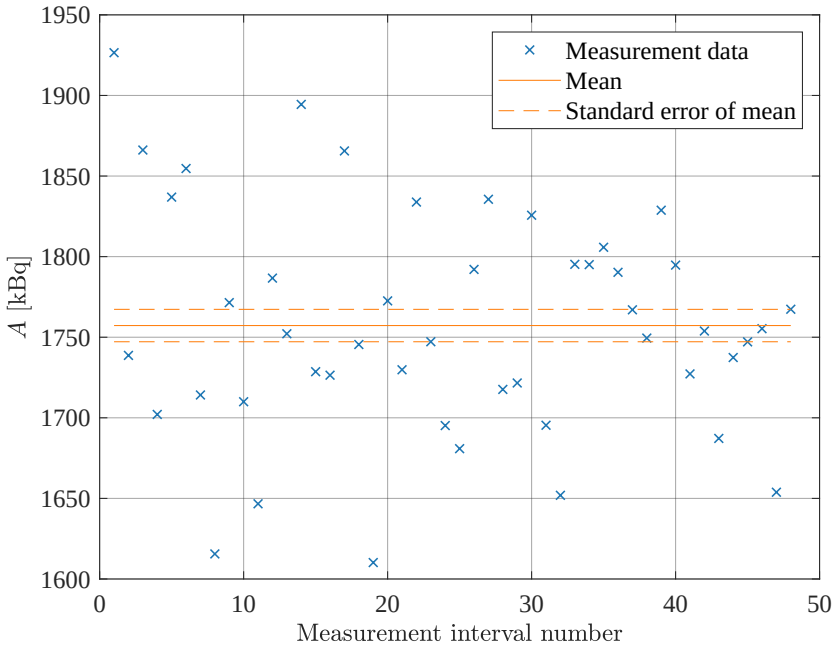

Figure 6.6: Activity of the ^{22}Na source over the 48 measurement intervals in the first of the five measurement. Additionally, the mean and standard error of mean over all 48 intervals are shown.

of 0.6% and deviates by a factor of 2 from the expected uncertainty estimated with the efficiency. The number of true coincidences in the last eight frames is about 12×10^3 and below. The resulting statistical uncertainty with the number of true coincidences is about 1% and in the same order of magnitude as the expected one with the efficiency from the literature. The activity in the last frames stems mainly from the ^{22}Na as the decay of the phantom activation is mainly within the first two hours after the irradiation. The relative standard error of mean is comparable for the other four measurements with the 48 frames of 5 min of the ^{22}Na source which underlines the reproducibility of the measurements.

A potential origin of the deviation between the expected activities and the measured activities is the phantom material. In the clinically used CT calibration of the TPS, PMMA is not correctly represented by the calculation of the stopping power for protons from the CT values [96]. The same impact might cause an error in the reconstruction algorithm for the image reconstruction from the acquired PET data as the scattering and attenuation corrections might be incorrect. Furthermore, the deviations can be caused by the presence of the phantom itself, the scatter

correction during the reconstruction of the PET images or the geometry of the source. The efficiency in the literature has been measured with line source in the PET without a phantom [98]. For a conservative estimation of the statistical uncertainty, the 1.5% efficiency is used in the analysis. While the number of true coincidences in the measurement verify this efficiency, the estimated uncertainty from the measurement is smaller. Taking into account, that the reconstruction algorithm might bias the uncertainty, the number of true coincidences appear to be the more reliable estimation of the uncertainty. For the position of the implants, the efficiency might be lower due to the deviation from the central axis. The implants are closer to the longitudinal center of the field of view of the PET scanner as the line source used in the literature. As the activity distribution within the implant has an impact on the efficiency as well and the absolute activity potentially bias the result of the reconstruction algorithm further, the efficiency of the PET scanner is used for the estimation of the statistical uncertainty.

6.3.2 Activation of the slice phantom

The different time intervals of the PET reconstructions are used for different purposes during the analysis. While the 48 frames of each 5 min are used for the decay observation, the three frames of the last three intervals of 30 min each are used for the analysis of the absolute activity. In Figure 6.7, the activity of the four implants is shown with the planned dose distribution which transferred from the planning CT to the CT from the PET measurement with a rigid image registration in the TPS RayStation 10B. With the help of the CT, a VOI is placed around each implant in the PET to evaluate the activity produced in the implants. In the figure, the activities are visualized as relative activities to peak activity in the PET images. As the ^{22}Na source with its activity of about 1.69 kBq is the highest activity in the PET images 3 h after the irradiation, the implants appear with the low activity at 1% level.

In a first step of the evaluation, the decay of the activity over the 4 h of measurement is investigated. An exemplary analysis is shown in Figure 6.8. For completeness, the further results of the analysis are shown in Chapter A.3.4. For the Implants 1 to 3, two exponential models are fitted to the data as it has been observed for the gamma-ray spectrometry of the activated titanium sample, one for the short-lived component and one for the long-lived component. Especially in the last hour of the measurement, the activity deviates from the prediction for the short-lived component with half-lifes about 20 min. This half-life is comparable to the one from ^{11}C of 20.36 min [37]. As the decay in the last hour of the measurement is low and the activity is associated with increasing statistical fluctuations, the uncertainties of the

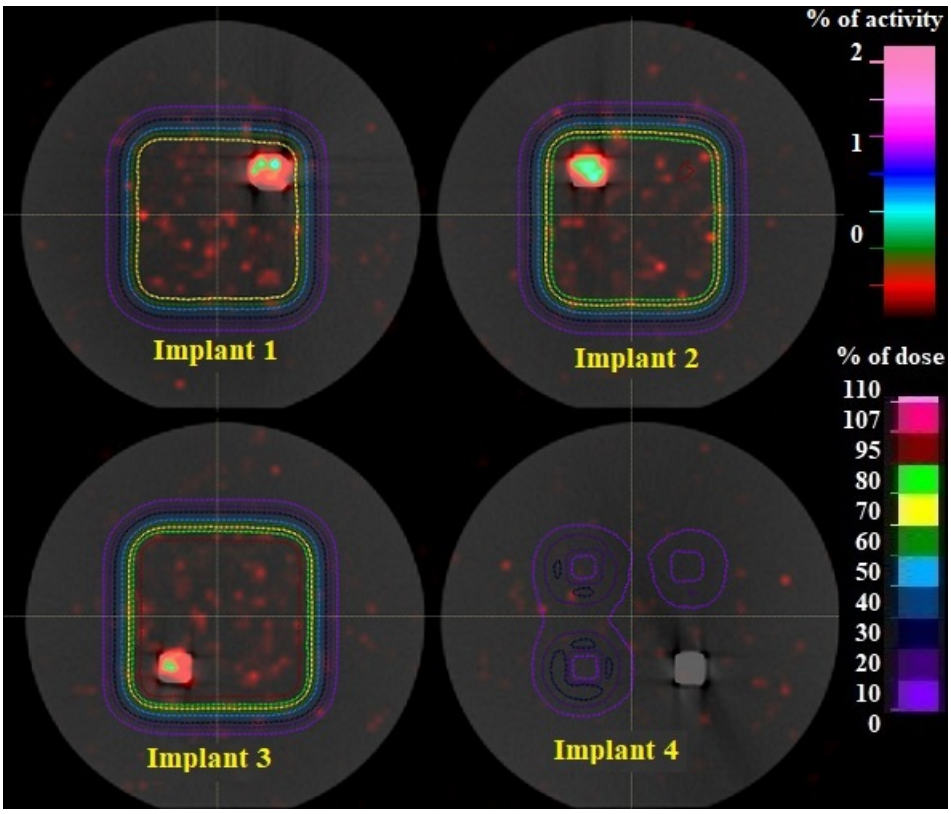

Figure 6.7: PET activity (color wash) of the first 30 min of the fourth hour matched with planned dose distribution (dashed lines) transferred from the planning CT on the CT for the PET reconstruction by a rigid image registration. The activities are comparably low due to the high activity from the ^{22}Na source in the PET image. The implants are sorted from the top left (Implant 1) to the bottom right (Implant 4).

half-life from the fitted model are relatively large. A complete overview of the fit results is summarized in Table 6.2.

Interestingly, the third implant, which is localized in the target volume is associated with the largest uncertainty in the fit. The analysis of the decay rates over time, Figure 6.8 and the figures in Chapter A.3.4, reveal, that the fluctuations of the data points for these implants are relatively large. For the long-lived component, half-lifes between 59 min and 182 min are fitted to the data. It is not possible to assign an individual radionuclide to the fitted half-lifes. However, from the prior studies, different radionuclides are expected to contribute to the activity [70]. Namely, these are ^{43}Sc with a half-life of 3.891 h, ^{44g}Sc with a half-life of 3.97 h, ^{44m}Sc with a

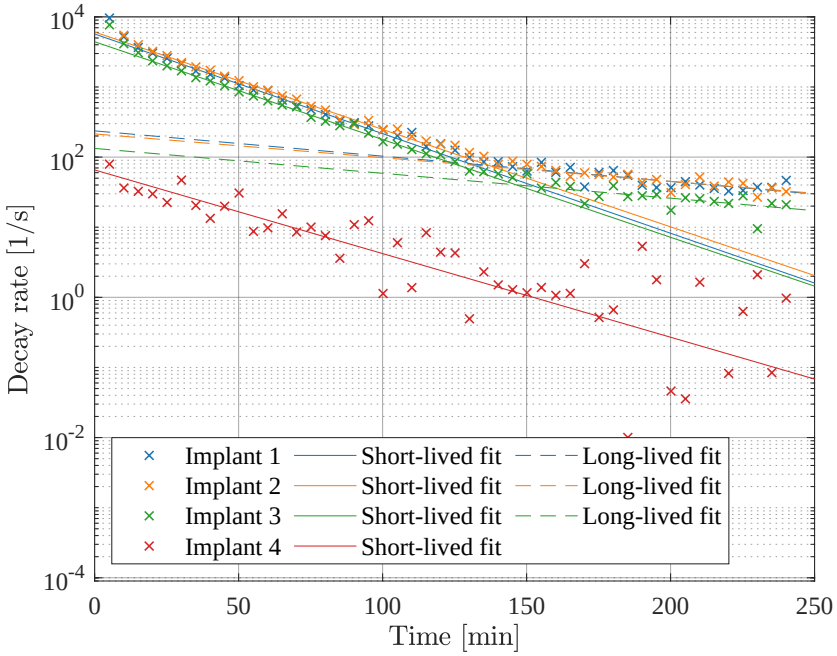

Figure 6.8: Half-life analysis of the four implants in the first measurement (initial plan). A model of two (Implant 1 to 3) and a model of one (Implant 4) exponential decays is fitted to the data. The line represents the short-lived fit and the dashed line the long-lived component for each implant.

half-life of 58.61 h, ^{45}Ti with a half-life of 184.8 min, and ^{48}V of 15.9735 d [37]. The short-lived radionuclide ^{47}V is competing with the decay of the phantom activation, as the half-life of 32.6 min [37] is too close to one from ^{11}C. In result, the decay of ^{47}V cannot be separated from the short-lived component induced by the phantom activation.

Furthermore, the first data points indicate a very short-lived component visible in the decay curves, as the points are above the fitted short-lived component. The time between irradiation and measurement is about 3 min for all five measurements. The short-lived radionuclides like ^{15}O with a half-life of 122.24 s [37] is a candidate which can be produced from the target nuclei in the PMMA phantom. However, it cannot be verified with the half-life. In clinical practice a time window of 3 min between irradiation and PET acquisition is not possible at WPE with a patient due to the distance between the PET and the treatment rooms. As the time stamps can be taken from the accelerator logs for the irradiation or the dose management system for the clinical workflow, a high accuracy of the time stamps of measurement

Table 6.2: Half-lifes fitted to the decay rates obtained in the single time frames of the PET frames. For Implant 4, only one exponential model is fitted to the data, only one half-life is given in the table.

Treatment plan	Implant	$T_{1/2}^{\text{short}}$ [min]	$T_{1/2}^{\text{long}}$ [min]
initial plan	1	20.2 ± 0.5	83 ± 25
	2	21.7 ± 0.4	89 ± 24
	3	21.6 ± 0.4	85 ± 31
	4	25.2 ± 2.8	
+2 mm range	1	21.9 ± 0.3	70 ± 30
	2	20.6 ± 0.3	92 ± 36
	3	21.8 ± 0.3	84 ± 31
	4	22.8 ± 2.4	
+3% dose	1	21.8 ± 0.4	139 ± 51
	2	22.0 ± 0.3	73 ± 14
	3	22.2 ± 0.3	76 ± 52
	4	28.7 ± 2.9	
−2 mm range	1	21.4 ± 0.4	140 ± 107
	2	21.9 ± 0.3	125 ± 75
	3	21.9 ± 0.4	182 ± 206
	4	29.1 ± 3.0	
−3% dose	1	21.1 ± 0.4	114 ± 57
	2	22.5 ± 0.4	110 ± 35
	3	21.9 ± 0.4	59 ± 21
	4	24.1 ± 2.1	

and irradiation is possible to calculate the decay curves for phantom measurements or patient treatment verification.

For Implant 4, only one single decay model can be fitted to the data which is associated with the short-lived component visible in the other implants as well. Interestingly, even for the plan with a PTV shift +2 mm in beam direction, Implant 4 appears not with high activity in the late measurement intervals. This is caused by the low number of protons reaching the target or the residual energies of the protons are below the threshold for the nuclear interaction of about 5 MeV for the expected radionuclides. In summary, only for the Implants 1 to 3 a long-lived component of the activity can be found in the last hour which might be useful for the field verification as it is not competing with the phantom activation.

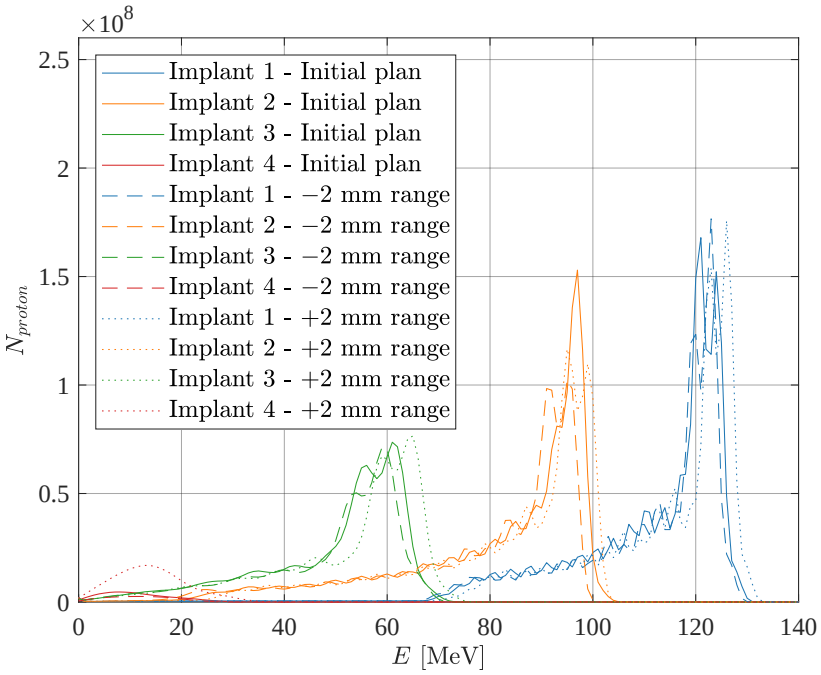

Figure 6.9: Simulated proton energy spectra in the four implants for the three different treatment plans, the initial plan (line), the one manipulated by +2 mm range (doted), and the one by −2 mm (dashed).

In the simulation study, the proton energy spectrum is obtained in the four implants. The four energy spectra per simulation are shown in Figure 6.9. For the three implants in the build-up and upstream region of the target volume, the energy spectra are very similar. The peak energy varies by about 5 MeV and the low energy tail of the spectra are expected because of the several interactions of the protons. For the implant in the distal fall off, Implant 4, the proton energy spectra differ between the different treatment plans. The different ranges of the three treatment plans result in the different proton energy spectra. For the treatment plan optimized on the target shifted by +2 mm in beam direction, the Implant 4 is reached by the treatment field, see Figure 6.3 right dose distribution. As a result, the more protons can reach the implant.

The shapes of the spectra are caused by the setup of the proton field. The sharp peak is caused by the distal layer of the proton field which has the highest weight. The double peak structure stems from two layers with similar weights. The proximal layers with a smaller weight in the treatment field contribute to the low energy tail and the decreasing tail to the low energies is associated with the smaller weight

with decreasing initial energy. The SOBP-like dose distribution delivered with the overlay of the different energies is discussed in Chapter 2.2.2. The last implant is reached only by low energy protons and the decreasing number of protons is caused by the multiple interaction upstream to the implant. The shape of the obtained energy spectra differs from the ones for the upstream implants which can be interpreted as the superposition of the different degraded energy layers. Energy spectra close to end of range of proton beams at the FBTR beam line have been investigated in the literature [99]. Due to the multiple scattering reactions and the statistical fluctuations of the energy transfer per reaction, the shape of the energy spectrum differs from the initial distribution to a wider non-symmetric distribution. In the literature, lower proton energies have been discussed further which are below the energy threshold for the nuclear interaction which are from interest for this study [99].

To calculate the activities from the energy spectra, the activation cross sections from the references collected in the EXFOR database are taken [56]. The six radionuclides ^{43}Sc, ^{44g}Sc, ^{44m}Sc, ^{47}V, ^{48}V, and ^{45}Ti can be produced from titanium and subsequently decay by the emission of a positron. However, the emission probability for the emission of a positron is less than one for the radionuclides [37]. The different half-lifes of the radionuclides result in radionuclides contributing to a fast decay like ^{47}V and long half-lifes of about 4 h of ^{43}Sc and ^{44g}Sc and ^{45}Ti with its half-life of 184.8 min result to slow decay component as described in the introduction of this study. The long half-life of ^{48}V of 16 d results in a low activity. For each reaction, the cross section data are interpolated in steps of 1 MeV which is the energy resolution of the simulated proton spectra. For the different reactions, a different number of literature studies are available in the database. While some energy intervals have been measured with small steps, for some energy regions, no data is available in the database. The most relevant example is the production of ^{45}Ti. The data ends at about 30 MeV, see Figure A.6. For the radionuclide ^{44g}Sc, the different data compete with each other. For the interpolation, the data obtained at the WPE and DLB are assumed to be the most reliable because the estimation of the experimental study is known in detail [13, 92, 93]. All interpolated excitation functions are summarized in Chapter A.3.1. For all six reactions, the displayed interpolation is considered to be the best available approximation with the available data and avoid an oscillation of the interpolated excitation function. This oscillation may occur due to the two distinct trends of cross sections measured in the different studies collected in the database.

The initial activity of the samples is decay corrected with the inverse concept of the decay correction for the DLB measurements described in Chapter 3.3. For the three 30 min intervals of the PET measurement, the expected activity is calculated. The decay during the short time gap between the irradiation and the start of the

measurement is corrected according to the concept. For the decay of ^{44m}Sc, the nuclide decays to the ground state ^{44g}Sc without the emission of the positron at first and a positron might be emitted during the decay of ^{44g}Sc, which has to be considered. In Figure 6.10, the predicted activities are shown with the measured activities in the PET images. The activities in the last three intervals of 30 min of the PET measurement are taken. For the Implants 1 and 2, the predict activity is lower than the measured one. This might be caused by the underlying phantom activation which is competing with the implant activation and visible in the half-life analysis. Only the last two intervals in the fourth hour after the irradiation might be useful for the analysis.

Furthermore, the activities of the implants are corrected by the deviation of the activity for ^{22}Na source from the calibration certificate as presented in Chapter 6.3.1. Compared with the prediction, the Implants 1 and 2 come with highest agreement between measurement and prediction. For the plan −2 mm range, the estimation of the activity of the implant might be systematically biased by the underlying phantom activation. This is shown in the half-life analysis, which is shown in Figure A.10. The half-life fitted to the long-lived component is associated with large uncertainties as listed in Table 6.2.

For Implant 4, the activities are all about 1 Bq and smaller. Even for the plan with an increased range by 2 mm, the activities are not larger, even though the predicted activities range up to 10 Bq. In the images, the implants do not appear with high activities. The proton energies range up to about 20 MeV. Furthermore, the cross sections for the four radionuclides are relatively low except for ^{48}V which has a half-life of 15.9735 d and results in a low activity, but this is included in the calculation of the predicted activity. However, even with the estimation of the statistical uncertainties from the expected number of true coincidences according to Equation (6.1) the agreement of the prediction and measurement is limited to a small number of data points. For completeness, the results of the measurements are summarized in Table A.3.

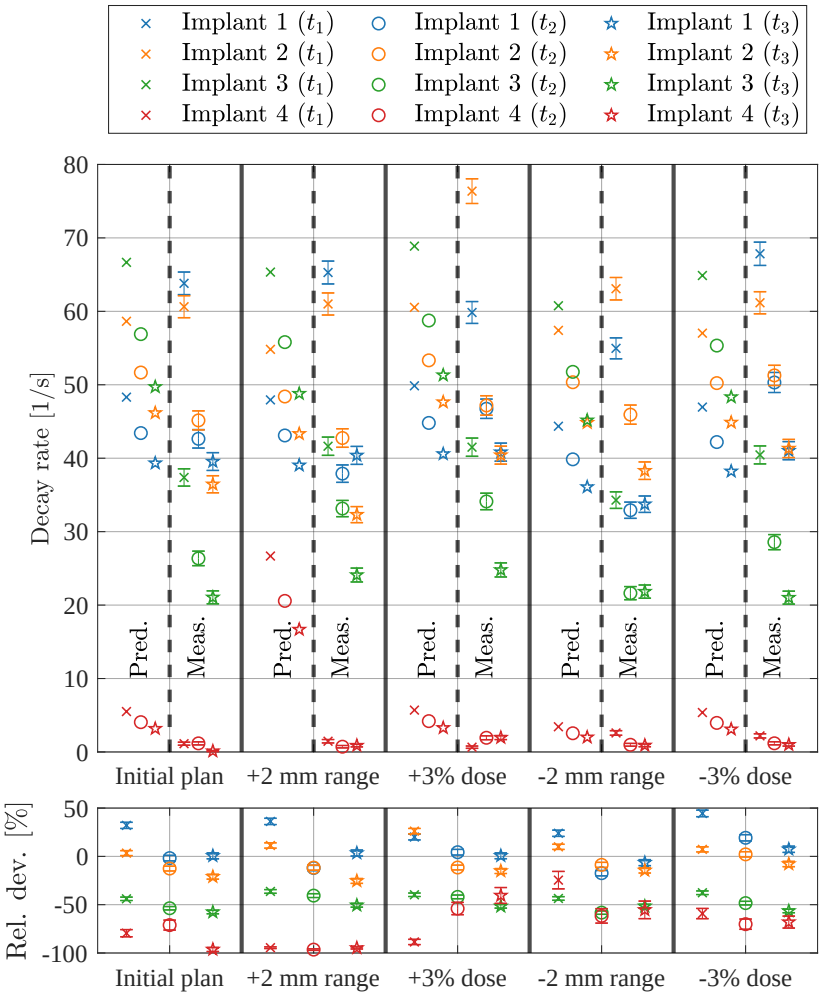

Figure 6.10: From the simulation predicted activities (without error bars) and measured activities (with error bars) for the five PET measurements of the slice phantom after the activation with the different treatment plans. The three different time intervals correspond to the 30 min reconstructions: t_1 is 150 min to 180 min, t_2 is 180 min to 210 min, and t_3 is 210 min to 240 min. The relative deviation from the prediction is shown below.

6.3.3 Clinical representative with an anthropomorphic phantom

The first activity distribution obtained during the first half of the fourth hour of the PET measurement is shown in Figure 6.11. Furthermore, the planned dose distribution is transferred on the CT from the PET measurement with an image registration implemented in RayStation 10B. The Implants B to E appear hyper

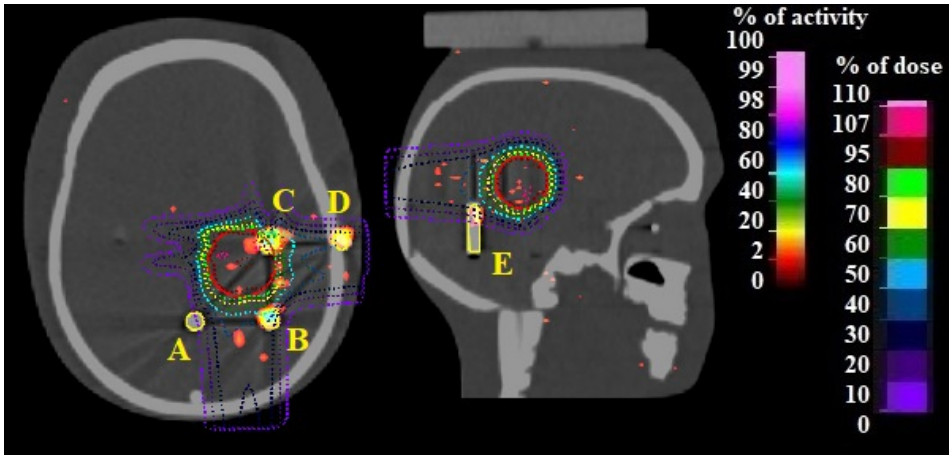

Figure 6.11: PET activity (color wash) of the first 30 min of the fourth hour matched with planned dose distribution (dashed lines) transferred from the planning CT on the CT for the PET reconstruction by a rigid image registration. The red circle is the virtual PTV which is used for the treatment plan. The implants are shown in yellow with their letters.

dense in the PET scan. The Implant A which is in the low dose fall-off is not activated on a visible level during the proton irradiation. Furthermore, only the cranial part of Implant E is in the treatment field. With the position of the Implant E compared to the dose distribution the lateral alignment can be verified.

Based on the CT image, a VOI is placed around each implant. As the diameter of the implant rods is 3 mm but the in-plane voxel size of the PET is approximately 3.3 mm the lateral dimensions of each VOI is larger than the implant itself and overlap with the tissue representing phantom material. However, the range of the positrons prior to the annihilation and emission of the two photons of about 3 mm, described in Chapter 2.3.1, might be covered by the increased VOI compared to the exact geometrical dimensions of the titanium implants.

By help of the VOI, in a first step the half-life of the activity is analyzed for all implants. For the Implants A to E, the result of the half-life analysis is shown in Figure 6.12. The activity in Implant F is smaller by several orders of magnitude and

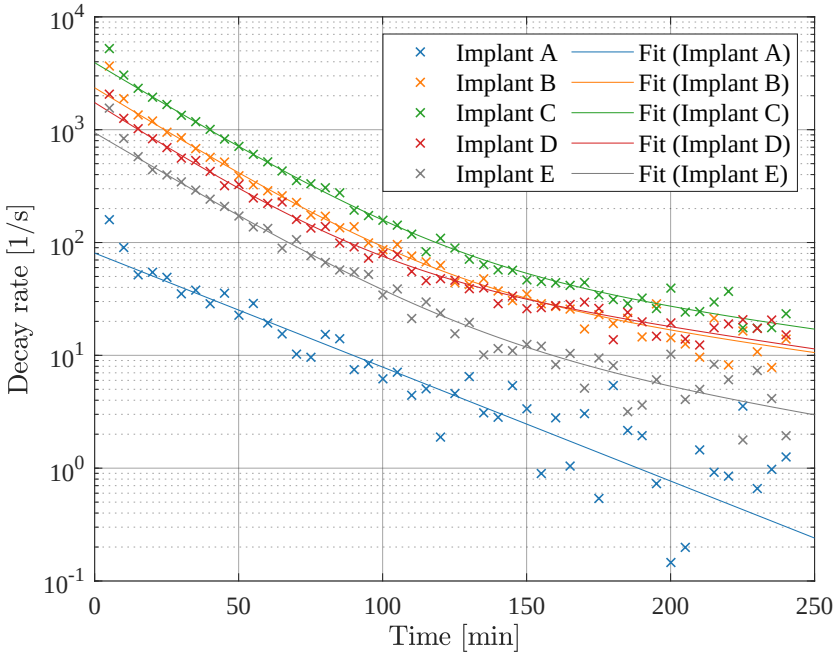

Figure 6.12: Half-life analysis of the five implants in the anthropomorphic phantom. A model of two (Implant B to E) and a model of one (Implant A) exponential decays is fitted to the data (lines). The analysis of Implant F is not shown due to the very low count rate (far away from treatment field).

the fit of an exponential decay model is dominated by the statistical uncertainties. For the Implants B to E, the sum of two exponential models is fitted to the data, for Implant A only one model is used. The results of for all six implants are summarized in Table 6.3. The smaller half-life is about 20 min for the Implants B to E and less than 30 min for the Implants A and F. This decay is associated with the decay of the activity which can be produced from the phantom as well. As the phantom consists of material with a large carbon content, the production of ^{11}C with a half-life of 20.36 min [37] is expected. As a result, these data cannot be used for the estimation of the activity of the implants. The second component of the decay model for the Implants B to E has a half-life between 70 and 90 min. This might be associated with long-lived radionuclides which can only be produced from the titanium and other heavier target nuclei. As a result, the activity obtained in the implants for the end of the measurement is sensitive to the radionuclides produced in titanium. However, the large uncertainty of the fit results for the long-lived component indicates the high statistical fluctuation of the measured activities, which

Table 6.3: Half-lifes fitted to the decay rates obtained in the single time frames of the PET frames. For Implant A and F, only one exponential model is fitted to the data.

Implant	$T_{1/2}^{\text{short}}$ [min]	$T_{1/2}^{\text{long}}$ [min]
A	29.8 ± 1.2	
B	19.0 ± 0.7	88 ± 49
C	19.3 ± 0.5	90 ± 34
D	18.1 ± 1.0	82 ± 35
E	19.6 ± 1.3	73 ± 66
F	26.5 ± 5.6	

is visible in Figure 6.12.

The first two data points are neglected for the fit to increase the stability of the fit result. These two data points have systematically higher activity than predicted by the fit. As well as described in Chapter 6.3.2, this is induced by short-lived radionuclides from the phantom material. The radionuclide ^{15}O with a half-life of 122.24 s is a potential candidate which can be produced from the plastic of the phantom.

Table 6.4: Measured decay rates A_1, A_2, and A_3 for the last three 30 min intervals in each implant in the PET measurement of the anthropomorphic phantom. The relative uncertainty (unc.) is estimated with the efficiency of the PET and the number of decays during the measurement intervals.

Implant	A_1 [1/s]	unc. [%]	A_2 [1/s]	unc. [%]	A_3 [1/s]	unc. [%]
A	1.67	15	1.26	17	1.02	19
B	26.4	3.7	19.7	4.3	15.3	4.9
C	44.7	2.9	31.9	3.4	25.4	3.8
D	27.9	3.6	21.2	4.2	20.6	4.2
E	9.52	6.2	6.03	7.8	4.98	8.6
F	0.60	25	0.64	24	0.04	96

The second part of the analysis is the estimation of the activity in each of the implants for the three measurements of 30 min. The measured activities are summarized in Table 6.4. The statistical uncertainty of the activity is estimated according to Equation (6.1) with the efficiency of the PET system according to the literature. As the ^{22}Na is not measured together with the phantom, the activities are not corrected for the absolute efficiency. For Implant A and F especially, the uncertainties are

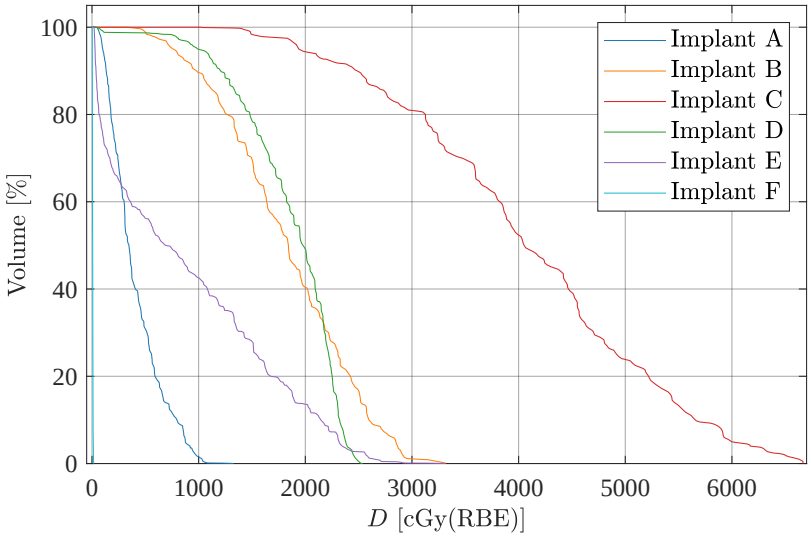

Figure 6.13: DVHs for the six implants in the anthropomorphic phantom. The doses refer to prescribed 30 fractions with each 2 Gy(RBE).

comparably large. For Implant F, no proton induced activity is expected and Implant A is close to the dose gradient.

To compare the activities from Table 6.4, the DVHs of the six implants are summarized in Figure 6.13. The doses refer to the prescribed median dose of 60 Gy(RBE) to the PTV. However, during the irradiation, only one fraction of 2 Gy(RBE) is delivered as it is commonly used in clinical practice. The dose statistics in fact reveals, that Implant F is only covered by some scattered particles which deliver a negligible dose. Furthermore, Implant A is lateral to the dose distribution which can be derived from Figure 6.5 as well. Hence, the absorbed dose in Implant A is less than about 10 Gy(RBE). From the dose distribution in the TPS and DVHs can be derived that Implant E ranges in the median dose region at the cranial end and out of the dose distribution with the caudal part. The uncertainty of up to 8% for the activity might not be useful for an absolute dose verification but the positioning of the implant may enable the verification of the lateral position. While Implant C is placed in the high dose region, up to 66 Gy(RBE) is delivered to the implant, the Implants B and D are in low dose entrance regions of the treatment fields. This results in smaller uncertainties and higher absolute activities produced in the implants, as summarized in Table 6.4 as more protons reach the implants.

From the first 5 min interval of the PET measurement, an additional observation can

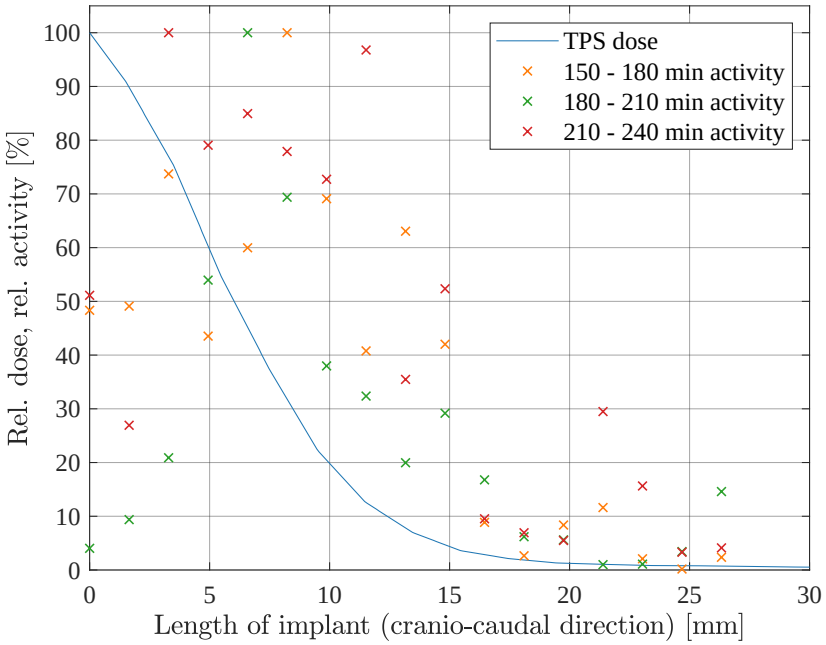

Figure 6.14: Dose distribution and activity per slice of the PET image for Implant E to investigate the lateral position of the phantom during the irradiation.

be derived. The activity distribution seems to be tilted by a shallow angle towards the dose distribution in the TPS. A possible reason might be a small misalignment of the phantom on the treatment couch during the irradiation. The irradiation process of the phantom is similar to a patient treatment. The phantom is aligned by the two orthogonal X-ray images compared with the expected position in the TPS. The position of the phantom is reviewed subsequently to the measurement to investigate the potential misalignment. A minor deviation of the real and expected position is found by the off-line review of the X-ray images. To estimate the impact of the misalignment on the treatment plan, the corrections are applied in the TPS and compared with the initially planned dose distribution. Only minor deviations on the level of 3% are simulated in the dose distribution in the target volume with the TPS. The deviations are supposed to be tolerable.

To investigate the potential for the verification of the lateral position, the dose and activity distribution along the cranio-caudal direction, the height of the cylinder geometry, are shown in Figure 6.14. While the dose fall-off predicted in the TPS is expected to be on the first 1 cm of the 2.5 cm of the implant. The fall-off of the

activity is about 1 cm apart for all three measurement intervals of 30 min. The last interval of the measurement is associated with increasing fluctuations of the activity which is associated with the increasing uncertainty with the decreasing activity over time. Interestingly, the first half of the fourth hour of the PET measurement appears to be associated with smallest lateral deviation of the dose distribution. From the half-life analysis in Figure 6.12 is known, that the long-lived radionuclides become dominant in the fourth hour of the measurement. The verification of the alignment with the activation of Implant E is most probably possible in the fourth hour.

As the lateral dimensions of the field increase due to scattering next to the implant, which can be derived from Figure 6.11, the deviation for the first interval might be caused by the phantom activation. However, the fluctuations make it difficult to determine an exact position of the implant. Furthermore, in the region, where the dose has reached the 1% level, an activity is still observed. As Implant F has an activity which is not zero in the activity analysis, this activity might be caused by background events from the phantom activation or the system-specific background of the PET system.

6.4 Discussion of the results and clinical application

In contrast to other studies in the literature, the presented measurements and simulations investigate the direct use of implants and markers for field verification in proton therapy which are used during surgical resection prior to the radiotherapeutic treatment. The limitation of the tissue activation for the off-line field verification by PET imaging has been found in biological wash-out [8]. In order to overcome this limitation, implanted markers which would be used exclusively for the field verification have been suggested to be used for the field verification [10, 11]. To avoid an additional surgical intervention for the patient, the decision for a proton therapy treatment for the single patient would be needed prior to the tumor resection during a surgical intervention. In contrast, this study investigates the use of implants which would be used during surgical resections. While the potential influence of the implants on the quality of PET imaging of the tissue activation has been investigated in the past [100], the direct use of the implants is investigated further. The two objectives of the study are the verification of the range of the proton beams on the one hand and the verification of the absolute dose on the other hand.

From the estimation of the uncertainties with the ^{22}Na source, the limitation of a PET scanner for absolute activity estimation can be derived. While in nuclear medicine diagnostic, an uncertainty of 5% on the absolute activity is satisfying [33],

for absolute dose verification in radiotherapy, the identification of dose deviation of 3% would be favorable [6]. The deviations of the reconstructed activity of the calibrated point source range between about −5% and +5%. This accuracy is not acceptable, if a deviation of the absolute activity of 3% for the dose needs to be detected. To overcome this limitation for the slice phantom, the activation is scaled by the deviation of the point source. For clinical practice, a calibrated point source would be needed in the clinical scan of the patient and needs to be shielded for patient safety.

The statistical uncertainty is estimated with the efficiency of the used PET scanner from the literature, which is given as 1.5% [98]. However, a different efficiency is estimated with the calibrated point source. This might be caused by several reasons. As the efficiency is estimated with the mean and standard error of mean, the absolute calibration of the PET system reveals a fluctuation of the absolute activity without an influence of the statistical fluctuation from a Poisson statistic. This deviation might be caused by the different methods. The method of the literature differs from the one used in this study. A point source placed in a PMMA phantom on the central axis of the PET scanner is used in this study, while a line source in a metallic tube is used in the literature. The source is placed 10 cm away from the central axis [98]. Due to possible scatter in the phantom during this study, a lower efficiency might be obtained with the calibrated point source.

A lower efficiency induced by the phantom would direct translate to a lower efficiency for any implant in a patient geometry. While all statistical uncertainties in this study are estimated according to Equation (6.1) with an efficiency of 1.5%, they would increase further with a smaller efficiency.

The estimated uncertainties for implants close to the target volume in the anthropomorphic phantom are on the 5% level. To detect deviations of 3%, this uncertainty needs to be reduced by a factor of two. An increased efficiency of a PET system by four would be sufficient to reach this goal. However, the length of the implants is still not comparable to clinical implants. Smaller implants result in lower activities and subsequently in larger statistical uncertainties. This again can potentially be avoided if it is possible to reduce the time gap between irradiation and imaging.

From the activation and simulation study with the slice phantom several conclusions for the clinical applications can be derived. At first, the implant distal to the dose distribution is not useful to monitor the correct stopping of the proton beam, even though the simulation study demonstrates the potential use. This might be caused by several reasons: One possible explanation is the incorrect cross section data. In an IAEA publication on nuclear reaction cross sections, it is mentioned an overestimation of cross section data for many literature sources [101]. However, these data have been introduced in the EXFOR database for nuclear reaction

data. Furthermore, only a limited number of reactions have been reviewed in this publication. The uncertainties of the different literature sources are not taken into account, as the handling of uncertainties has been changed over time and they are not comparable between the single studies, as it is known from the carbon activation [61]. Additionally, the cross section data are sparse for higher energies and thus the interpolation of the data might lead to additional uncertainties for the absolute cross sections. Furthermore, for the production of ^{45}Ti, the cross sections are available in a relatively narrow energy interval compared to the energy range of therapeutic proton beams. At last, the carbon activation study is demonstrated, that the cross section data might be systematically biased by other reactions, so-called monitor reactions. All in all, the presented studies demonstrate the need of further nuclear physics investigations in cross section measurements. The accurate knowledge of the cross section is relevant in case the absolute delivered dose should be verified with PET imaging. By using implants at dedicated positions in the dose distribution, it is not possible to compare produced activity distributions obtained with PET imaging and predicted in MC simulations. Aiming for the absolute activity enforces the knowledge of the absolute cross section for all relevant reactions.

Compared to diagnostic applications of PET imaging, the activity of lower than 100 Bq is comparably low. This may result in limitations of the dynamic range of the PET system especially for the reconstruction algorithms. Therefore, the spatial resolution of the reconstruction is chosen as 3.3 mm. For small implants or implants which partially in the voxel of the image the phantom activation may compete with the implant activation. This becomes more relevant for small implants like clips.

The limitation of the counting statistics for off-line PET has been discussed in the literature in the past [8]. In this aspect, the in-room implementation is superior to any off-line implementation. However, the main contra-point for in-room solutions is described in Chapter 1. The problem of the counting statistics for implants has been described in the literature as well [10]. Interestingly, in a follow-up study, an increasing visibility of the implant in the PET image by decreasing fractional dose has been observed [11]. This is a paradox as the dose and the number of protons should be linear and do not change the energy spectra of the protons at the different positions in a phantom or patient. At last, to overcome the financial costs for multi-room centers, mobile setups like prompt-gamma methods might be superior [7].

Another limitation comes with the energy of the produced positrons during the decay and their direct influence on the spatial resolution of the PET image. While the clinically used radionuclide ^{18}F has a mean positron energy of 249.8 keV [37], the positron energies for the scandium and titanium radionuclides are higher up to 632.0 keV mean energy for ^{44g}Sc [37]. However, for the long-lived ^{48}V, the energy

is comparable to ^{18}F with an energy of 290 keV [37]. With the discussed half-life of ^{48}V a build-up of the activity might limit the application after several fractions. The advantage of metallic implants would be the shorter range of the positrons in the metallic implants but a loss on the surface of the implant is expected. However, the range of the positrons of the radionuclide ^{15}O with a mean energy of 735 keV is expected to be 3.0 mm mean range in human tissue which is comparable to the size of one voxel in the PET image used in this study [31]. This radionuclide is not relevant for field verification in proton therapy due to its half-life of about 2 min [37].

From activation study with the anthropomorphic phantom, further clinically relevant conclusions can be derived. While the lateral dimensions of the implants are at the same size of a voxel in the PET, the length of the implant with 2.5 cm is large compared to clips which are used during surgical resections. From the fluctuations of the activity in the single slices of the PET images which are used to determine the lateral activity fall-off in Chapter 6.3.3 can be derived, that the activity of small implants are dominated by the statistical uncertainty.

Additionally, the activation of the complete phantom which is visible in the first minutes of the PET acquisition demonstrated the limited alignment of the phantom on the treatment couch during the irradiation. Subsequently to the analysis of the data, the alignment of the phantom is reevaluated by a therapist, to identify the shift of the phantom during the irradiation. However, to identify this small shift, the implant activation is not helpful as the shift is only on the 1 mm scale. Furthermore, this displacement cannot explain the deviation of about 1 cm between the dose distribution and the activity distribution in the Implant E. In result, for the lateral alignment, implants like Implant A are superior to detect the displacement as they would be in the high dose region in case of a misalignment of the patient, but the displacement needs to be several cm to be detected.

In general, implants in positions such as Implants B to D have the potential to be useful for a field verification. The implants come with relatively small statistical uncertainties and the absolute activities become more reliable with a parallel scan of a calibrated source. Furthermore, the distance close to the target volume of Implant B and C represent potential position of clips while the Implant D in the skull bone might be a screw used for fixations after surgical interventions.

With the range of positrons in tissue which is about 3 mm which is smaller in dense material like metals a potential application might be implants with dimensions larger than 3 mm. Potentially, screws used in surgery to fix bones might be used for this application. This would come with different advantages: At first, the loss of positrons outside the implant would be reduced. Furthermore, in the center of the implant, a competing decay with the tissue activation would be avoided

as the positrons from the tissue activation would not reach the implant center. Additionally, avoiding the competing decay would allow to use PET acquisition times closer to the treatment which will increase the number of true coincidences and subsequently reduces the statistical uncertainty. Furthermore, the production of ^{47}V becomes more relevant for the activity. From the excitation functions from the literature, summarized in Chapter A.3.1, a smaller energy threshold compared to other reactions enables the use of implants closer to the end of proton beam range and the reduced residual range would increase the sensitivity for potential deviations by this method. However, the spatial resolution up to 6 mm full-width half-maximum would limit this application further [98]. Additionally, the necessity of large implants reduces the number of patients which potentially benefit from this method compared to smaller implants like small clips.

The biological wash-out would have an advantage using the implant activation for the field verification. As the activity distribution is spread over a larger volume with the increasing time, the so-called biological half-life would decrease the time gap after which the implant activation would dominate compared to the tissue activation. As only plastic phantoms without any further transport processes are used in the presented study, these transport processes are not modeled within the phantoms. Decreasing the time between irradiation and PET acquisition would increase the activity and reduce the statistical uncertainties.

Together with the biological wash-out in the tissue activation, this would may result in the opportunity to decrease the time between irradiation and PET acquisition which is sensitive to the decay in the implant. As the current clinical applications are limited, further developments and improvements of PET imaging might increase the potential application. At first, the efficiency of PET scanners is increased over time [98]. An increasing efficiency would reduce the statistical uncertainty and would enable the use of smaller implants with less overall activity. The increasing time resolution of ToF-PET will increase the spatial resolution of the PET further [28]. An increased spatial resolution would reduce the competing effects between tissue and implant activation.

As already mentioned, the shorter time gap would reduce the statistical uncertainty of the method, an increasing spatial resolution would again be helpful for this method. A spatial resolution on the dimensions of the implants, for example 3 mm would allow for decreasing VOIs around the implants and subsequently, the competing effect between tissue and implant activation. In Chapter 2.3.1, the goal of so-called reconstruction-free ToF-PET is mentioned [30]. A spatial resolution on this level would be sufficient for the application. Dealing with higher activities would furthermore allow for smaller voxel sizes in the reconstructed PET images which simplifies the contouring of the VOI for the implants.

While the study on using implants for proton therapy field verification from the literature [10, 11] focused on rare materials in medical application and thus the radionuclides produced are not commonly used in PET imaging, this study focuses on medical used implants. However, the materials are chosen by their large cross section close to the end of the proton beam range and low reaction threshold. In the literature, high doses have been applied to the phantoms and implants in the study. Furthermore, a decreasing dose resulted in a better visibility of the implant in the phantom activation which is kind of a paradox, as the dose should be linear with the number of protons and consequently with the number of produced radionuclides [11, 35]. The studies from the literature furthermore, indicate a different patient group which can potentially benefit from the proposed methods, like patients who undergo so-called stereotactic irradiations with fractional doses of about 10 Gy [10]. The higher dose results in a lower statistical uncertainty. The sparing of the healthy tissue would be more crucial for these patients.

In addition, a further limitation is mentioned in the literature study, which does not apply to the implants used in the presented study. Some of the marker materials from the literature appear to be not bio-compatible [10]. The implant material used in the presented study is already used in surgical applications and this limitation would not apply here. Furthermore, foils as markers have been used in the literature study, while rods are used in the presented study. In comparison, the volume of foils appears to be closer to the one of markers or clips, while the geometric properties of the implants are more similar to parts of the rods.

All in all, the clinical applications of titanium implants for field verification in proton therapy remain limited. While in the first pre-studies a strong dependence between the activity and dose distribution has been observed with a small animal PET [12, 13, 93], the more clinical setups demonstrate the limitations. In the first studies, the implants have been extracted from the phantom and the activation of the titanium has been investigated in the first hour after treatment. The activity in the first hour after the irradiation is associated with the decay of ^{47}V with a half-life of 32.6 min. For the phantom studies, this decay is competing with the decay of the short-lived tissue activation with a half-life of 20.36 min of ^{11}C [37]. This is shown by the half-life analysis of each measurement which demonstrates, that only a long-lived component can be used to determine of implant activation. However, the half-life analysis is difficult due to the increasing statistical uncertainties and fluctuation of the single measurement point. The fourth hour after treatment is sensitive for the implant activation only. The two necessary improvements demonstrate the potential application in the future. The combined improvements in terms of spatial resolution and efficiency would allow for the short time gaps between irradiation and imaging. From the half-life analysis, an increase of the activity by a factor of 100 can be derived. As a result smaller implants compared to the current study can be used.

7 Conclusion and outlook

Nuclear reactions and the activation of matter in the beam path can be used for post-fractional treatment verification of the range of the proton beam and absolute delivered dose [3, 4, 8]. The favorable dose distribution of protons leads to the requirement of high-accuracy treatment to ensure the dose delivery to the target volume and sparing of the OARs to achieve reliable clinical out-come. In order to improve these techniques, three different aspects of nuclear physics in proton therapy have been investigated in the presented studies.

The latest studies of the RBE of proton irradiation reveals an increasing biological effect close to the end of the range, as discribed in Chapter 2.1.2 [22]. Furthermore, an accurate knowledge of the proton range in the patient enables a reduced safety margin surrounding the tumor volume and consequently the irradiated volume can be reduced further. At the WPE, many pediatric patients are treated with brain cancers. Especially for these patients, a reduction of the irradiated brain volume would be favorable.

The presented studies combine basic nuclear physics measurements of a single cross section, a first test for the potential application of radionuclides produced from iodine for field verification in proton therapy, and a clinical validation for the application of implants for field verification in proton therapy. All three aspects represent the different steps which are necessary to implement the nuclear reactions for field verification in proton therapy.

In the first part of this work, in Chapter 4, the production of ^{11}C from natural carbon is investigated in detail. A new reference cross section is derived from several measurements with different targets and setups. A cross section of (68 ± 3) mb at a beam energy of (97 ± 3) MeV is proposed as the new consensus reference cross section from the data. Additionally, thick targets increase the systematic uncertainties of the cross sections and thin target foils are favorable for cross section measurements.

A 3% difference remains for the measurements with the in-beam between the experiments at the WPE and the one performed during the prior study [59]. This difference is caused by the two methods of obtaining the number of incident protons with a FC on the one and an IC on the other hand. A detailed search in the

literature reveals, that this systematic difference is known from several studies at different proton therapy centers and is still under investigations [72, 74]. These studies aim to reduce the experimental uncertainties and coming to a consensus value for the number of protons and the absorbed dose as well.

The second topic is the review of the cross section data in the databases. Many cross sections have been measured relative to the production of ^{11}C on the one hand. On the other hand, the issue of the accurate knowledge of the absolute cross section which has been upraised at the beginning of the presented study, may come up for other excitation functions as well for relative measurements of other cross sections. In general, prior to the use of the cross section data, a review of the data seems to be necessary regarding their spread and the associated experimental method. First measurements aiming to measure the complete excitation function for the production of ^{11}C from natural carbon are ongoing [85].

The second part of this work, Chapter 5, investigates the radio-activation of iodine represented with a CsI target. Iodine is a commonly used contrast agent in diagnostic CT imaging. Many radionuclides and of these several positron emitters are produced from iodine during proton bombardment. This demonstrates the potential application of iodine as a contrast agent which is activated during proton treatment. The several radionuclides and positron emitters are identified in the gamma-ray spectrum of the activated sample. However, the identification is limited to positron emitters with an additional gamma-ray signature in spectrum. The calculation of cross sections is not possible, as the production from caesium and iodine are not separable in the analysis and the large number of radionuclides and options for the reactions would lead to additional uncertainties. For targets with less radionuclides produced from the target nuclei, this method is more successful.

Many different topics need to be investigated regarding the activation of iodine. As already mentioned in Chapter 5.3, the cross sections in the database scatter by up to one order of magnitude. An accurate knowledge would be necessary for clinical applications. Additionally, medical questions are figured out in Chapter 5.3 as well. The targeting of the iodine contrast agent is one of the questions to be answered as well as biological half-life regarding the wash-out and potential uptake of radioactive iodine in the thyroid.

At last, a phantom study on the potential use of titanium implants for treatment verification with PET imaging is discussed in Chapter 6. The experimental phantom study is extended by a MC simulation to predict the measured activities. The analysis of the performance of the PET scanner reveals limitations regarding the reproducibility to reach the 3% detection limit for the absolute dose verification. By correction of the measured activities with a calibrated point source, it is possible to predict the activities with the MC simulation for some of the scenarios. The

deviations between prediction and measurement might be caused by the sparse cross section data. Furthermore, the more clinical example with an anthropomorphic phantom demonstrates the limitation for clinical applications of activated implants. The most relevant point is the statistical uncertainty which is associated to the low activities of several 10 Bq. Some limited cases for application can be derived from the results anyway. Implants which are located lateral to the treatment fields might be used to monitor alignment of the patient. Some dedicated implant positions seem to have the potential to be used in clinical applications. However, only a limited number of patients would benefit from these applications.

Prior to the transfer of the activation of titanium implants to the clinical application for field verification, some further investigation might be necessary. At first, the possibility of the activity prediction for a patient geometry needs to be investigated further. The presented results demonstrate deviations between the predicted and measured activities. Once this has been validated, the expected activity needs to be reviewed regarding the expected statistical uncertainty of the activities and the potential clinical significance of the PET imaging. The simulation of patient-like geometries or simulations with real patient data would be the next steps towards the clinical application. A further simulation study may investigate advantages of the biological wash-out on the hyper dense signal from the implants in the PET image compared to the signal from the tissue. The current investigations on PET imaging may solve the remaining limitations, as the reconstruction-free ToF-PET as well as an increased efficiency of a factor of four already meet the estimated requirements. All in all, patients with small safety margins for the target volume may benefit from this method if useful implants can be found in the patient.

Furthermore, a detailed look on the cross section data and the interpolated excitation functions reveals, that a detailed investigation on the cross section data for the production of positron emitters is necessary. In contrast to an exact estimation of single cross sections, the estimation of a cumulative excitation function and their time dependence might be a different approach towards a more detailed data set. The sparse data for ^{45}Ti demonstrates the necessity anyway.

In addition to the limitations discussed in Chapter 6.4, further applications of PET imaging in proton therapy might provide an additional help to decrease uncertainties of treatment planning. Most recent publications demonstrate the use of the 511 keV photon CT image to estimate the proton stopping power [96]. The complexity of proton therapy might enforce the introduction of several approaches for the improvement of the treatment outcome for only a small number of patients for each technique. In conclusion, not all patients would benefit from one single technique, but all the different techniques and improvements would be beneficial for the patients.

All in all, the three single parts demonstrate the limitations which come with the currently available data and techniques for proton therapy field verification by PET imaging. The basic nuclear physics data, especially the cross section data, are sparse and scatter by up to 15%. Furthermore, the current techniques of PET imaging needs to be improved further for a wide application in clinical settings. As the latest developments in PET imaging aim to increase the efficiency and spatial resolution [28], next generation of PET scanner may feature the required improvements.

A Measurement data for re-calculation

This chapter provides an overview on the original measurement data, to re-calculate most of the calculation presented in the analysis chapters.

A.1 Data for the graphite activation

In Table A.1 only the relevant physical data of the samples are listed. As a result for the samples A to D, no thickness z is listed in the table. In conclusion, for the samples E to L, no mass is given in the table, as it is not necessary for the cross section calculation. For the samples E, F and L, the particle density ${}^{n}/_{V}$ is $4.717 \times 10^{22}/\mathrm{cm}^3$. For the samples G, H, I and K ${}^{n}/_{V} = 9.080 \times 10^{22}/\mathrm{cm}^3$ is used in the calculations. The thickness of the tilted target is 5 mm but because of the 45° tilt, the target thickness in beam directions is increased compared to size of the cuboid.

Table A.1: Measured activities A_{meas} with its statistical uncertainty from the number of counts together with the t_1, the T_{Life} and the number of measurement intervals n_{Int} for the calculation of the initial activities A_0 in Table 4.5. (1) indicates that the result is taken from the prior study. (2) is the irradiation performed during the joint experiment with both experimental studies.

ID	A_{meas} [Bq]	T_{Life} [s]	n_{Int}	T_1 [s]	m [g]	z [mm]
A(1)	396.11 ± 0.97	2569.9	30	3528.2	0.59	
B	287.00 ± 0.86	4317.9	30	3535.2	1.16	
C	164.11 ± 0.59	7146.3	30	3543.4	3.45	
D	178.95 ± 0.63	7917.8	30	3542.4	5.69	
E	43.88 ± 0.32	3537.35	30	3543.3		1.05
F	83.18 ± 0.44	2402.65	30	3542.7		1.05
G	155.23 ± 0.58	2376.9	30	3543.2		1.0
H	155.82 ± 0.59	4270.95	30	3543.1		3.0
I	153.56 ± 0.58	5227.35	30	3543.3		5.0
K(2)	154.17 ± 0.60	6144	30	3542.0		7.1
L	175.33 ± 0.70	6069.1	30	3542.8		15.2

A.2 Data for the CsI activation

Table A.2: Measured activities A_{meas} with its statistical uncertainty from the number of counts together with the t_1, the T_{Life} and the number of measurement intervals n_{Int} for the calculation of the initial activities A_0 in Table 5.2.

radionuclide	A_{meas} [Bq]		T_{Life} [s]	n_{Int}	T_1 [s]
^{128}Ba	0.0305	$\pm$ 0.005	442 345.4	1491	70 469.8
^{131}Ba	0.0064	$\pm$ 0.0004	1 700 020.6	473	508 318.7
^{125}Cs	0.45	$\pm$ 0.05	44 632.6	378	3846.2
^{127}Cs	1.28	$\pm$ 0.01	44 632.6	378	3846.2
^{129}Cs	0.177	$\pm$ 0.011	442 345.4	1491	70 469.8
^{119}I	1.83	$\pm$ 0.14	3542.3	30	3333.85
^{121}I	2.062	$\pm$ 0.022	44 632.6	378	3846.2
^{123}I	3.315	$\pm$ 0.027	44 632.6	378	3846.2
^{124}I	0.0181	$\pm$ 0.0007	1 700 020.6	473	508 318.7
^{126}I	0.0283	$\pm$ 0.0011	1 700 020.6	473	508 318.7
^{116}Sb	2.96	$\pm$ 0.2	3542.3	30	3333.85
^{117}Te	0.597	$\pm$ 0.024	44 632.6	378	3846.2
^{119}Te	0.0937	$\pm$ 0.002	442 345.4	1491	70 469.8
^{121}Te	0.0335	$\pm$ 0.0012	1 700 020.6	473	508 318.7
^{123m}Te	0.002 37	$\pm$ 0.000 21	1 700 020.6	473	508 318.7
^{122}Xe	0.086	$\pm$ 0.009	442 345.4	1491	70 469.8
^{123}Xe	1.03	$\pm$ 0.23	44 632.6	378	3846.2
^{125}Xe	0.16	$\pm$ 0.0021	442 345.4	1491	70 469.8

A.3 Additional data for the titanium activation

A.3.1 Cross section data for the estimation of the predicted activity

The cross section data visualized in this chapter are taken from the EXFOR database [56]. Due to the sparse data at high energies for the production of ^{43}Sc and ^{44g}Sc, the interpolated excitation functions shown in the figures are not adapted from any model. For the production of ^{47}V and ^{45}Ti, it is assumed, that all target isotopes of ^{47}V are equal. Due to the different estimation of uncertainties, no uncertainties are given in the figures.

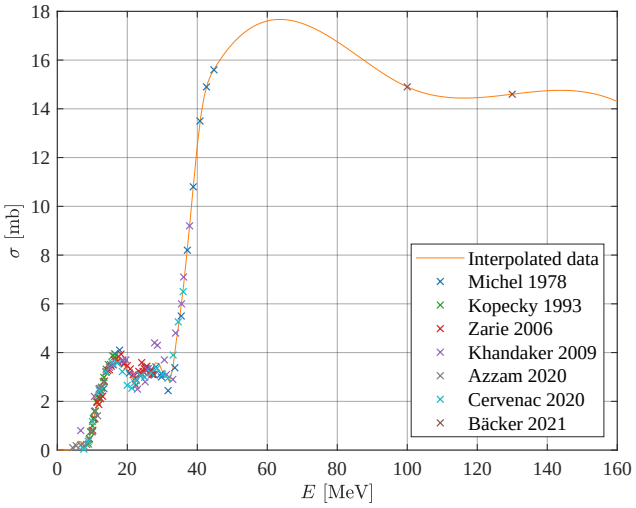

Figure A.1: Excitation function for the production of ^{43}Sc from titanium with the data from the literature and interpolation used for the analysis [13, 102–107].

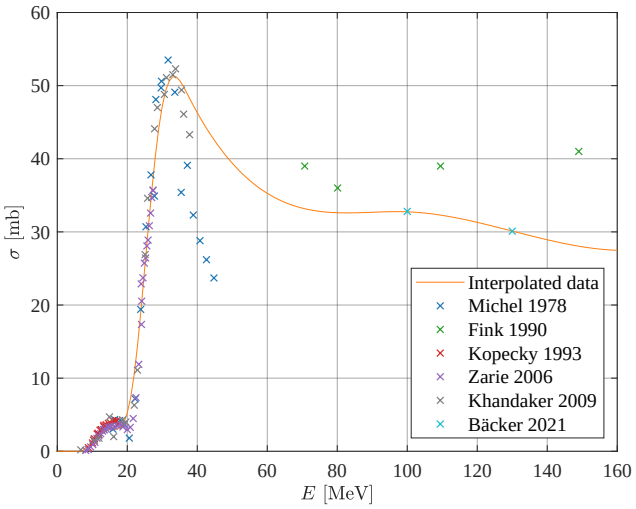

Figure A.2: Excitation function for the production of ^{44g}Sc from titanium with the data from the literature and interpolation used for the analysis [13, 104–108].

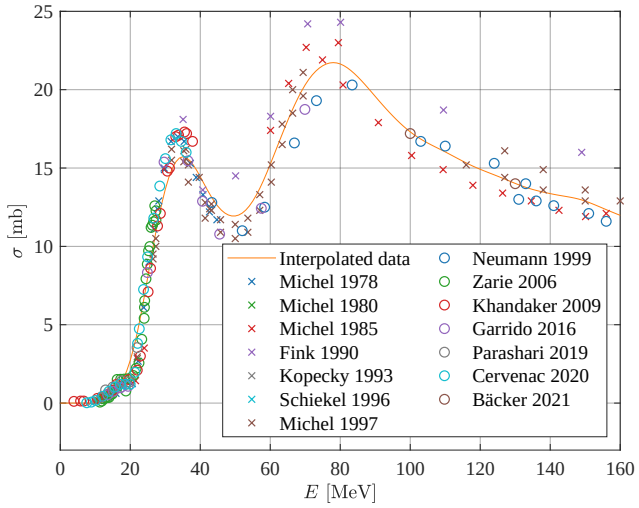

Figure A.3: Excitation function for the production of ^{44m}Sc from titanium with the data from the literature and interpolation used for the analysis [13, 103–115].

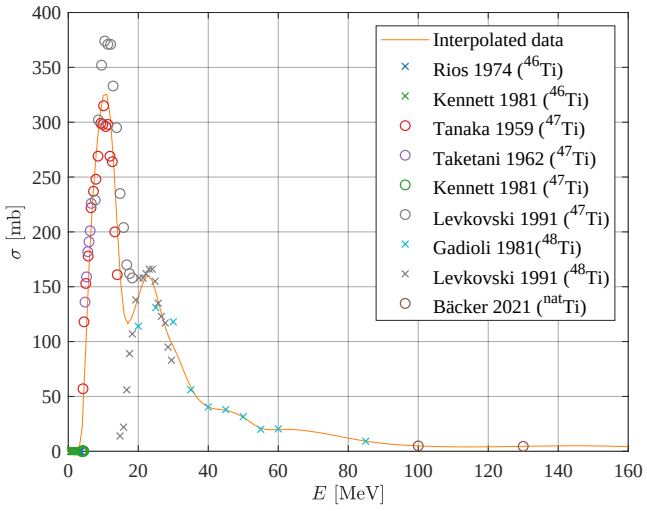

Figure A.4: Excitation function for the production of ^{47}V from titanium with the data from the literature and interpolation used for the analysis [13, 116–121].

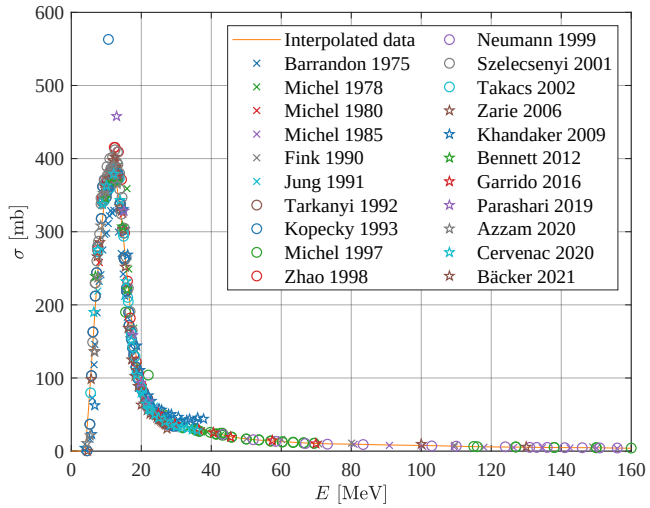

Figure A.5: Excitation function for the production of ^{48}V from titanium with the data from the literature and interpolation used for the analysis [13, 102–110, 112–115, 122–128].

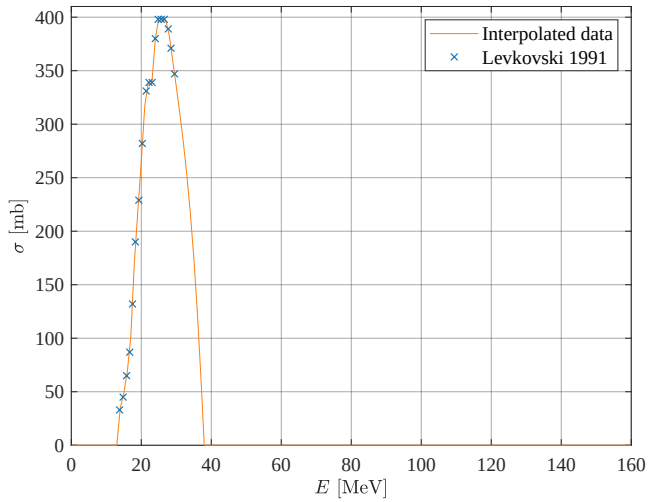

Figure A.6: Excitation function for the production of ^{45}Ti from titanium with the data from the literature and interpolation used for the analysis [121].

A.3.2 Technical drawing of the slice phantom

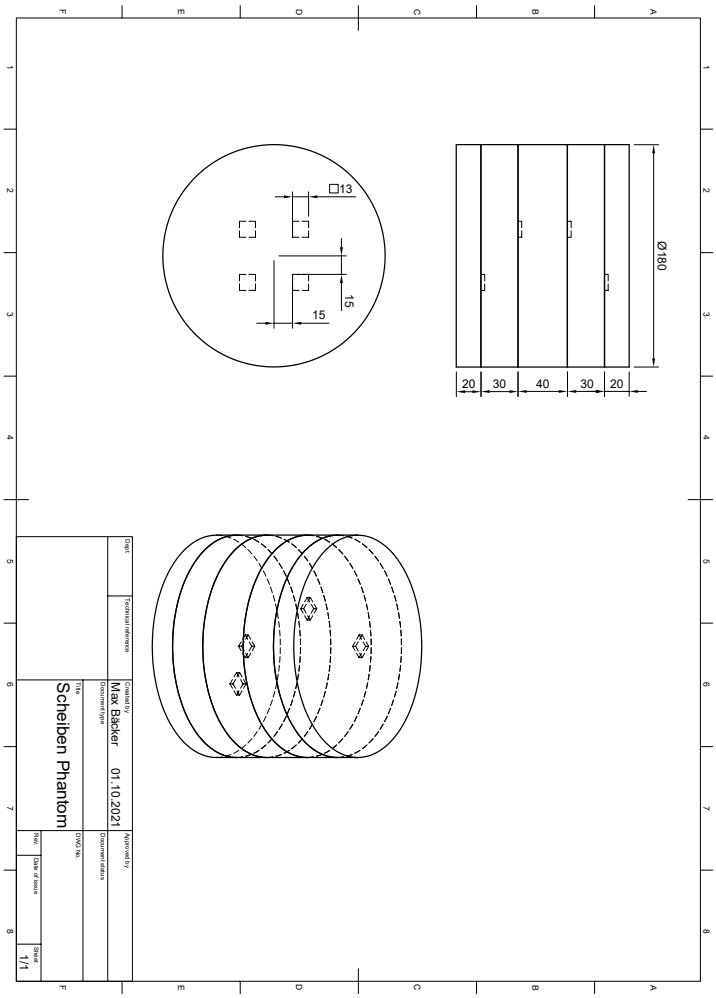

Figure A.7: Technical drawing of the slice phantom with the four inserts for the titanium implants between the five slices.

A.3.3 Measured and predicted activities of the slice phantom measurements

Table A.3: Measured decay rates A_1, A_2, and A_3 for the last three 30 min intervals in each implant in the PET measurement of the slice phantom.

Treatment plan	Implant	A_1 [1/s]	A_2 [1/s]	A_3 [1/s]
initial plan	1	63.8	42.6	39.5
	2	60.6	45.2	36.5
	3	37.4	26.4	21.1
	4	1.13	1.17	0.12
+2 mm range	1	65.3	37.9	40.4
	2	61.0	42.7	32.3
	3	41.6	33.1	24.1
	4	1.46	0.72	0.87
+3% dose	1	59.8	46.7	40.8
	2	76.4	47.2	40.4
	3	41.5	34.1	24.8
	4	0.65	1.93	1.96
−2 mm range	1	55.0	32.9	33.8
	2	63.1	45.9	38.3
	3	34.3	21.6	21.8
	4	2.59	0.98	0.89
−3% dose	1	67.8	50.3	41.0
	2	61.2	51.3	41.3
	3	40.4	28.6	21.0
	4	2.19	1.18	0.99

Table A.4: Predicted decay rates A_1, A_2, and A_3 for the last three 30 min intervals in each implant in the PET measurement of the slice phantom.

Treatment plan	Implant	A_1 [1/s]	A_2 [1/s]	A_3 [1/s]
initial plan	1	48.3	43.4	39.3
	2	58.6	51.7	46.2
	3	66.7	56.9	49.7
	4	5.50	4.06	3.18
+2 mm range	1	47.9	43.1	39.0
	2	54.8	48.4	43.3
	3	65.3	55.8	48.8
	4	26.7	20.6	16.7
+3% dose	1	49.9	44.8	40.6
	2	60.5	53.3	47.6
	3	68.9	58.8	51.3
	4	5.70	4.20	3.29
−2 mm range	1	44.4	39.8	36.1
	2	57.4	50.3	44.8
	3	60.8	51.8	45.2
	4	3.43	2.55	2.00
−3% dose	1	47.0	42.2	38.2
	2	57.0	50.2	44.9
	3	64.9	55.3	48.3
	4	5.37	3.96	3.09

A.3.4 Half-life analysis of the slice phantom measurements

To follow the description in Chapter 6.3.2 about the half-life analysis, the activities over time in the four implants are shown in the figures. For the Implants 1 to 3 to different models are fitted for the long- and the short-lived component. For Implant 4, only the short-lived model can be applied.

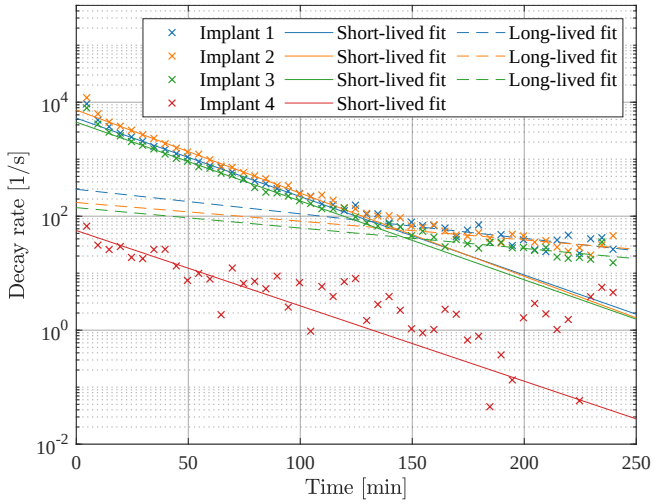

Figure A.8: Half-life analysis of the four implants in the second measurement (shifted by +2 mm range). A model of two (Implant 1 to 3) and a model of one (Implant 4) exponential decays is fitted to the data.

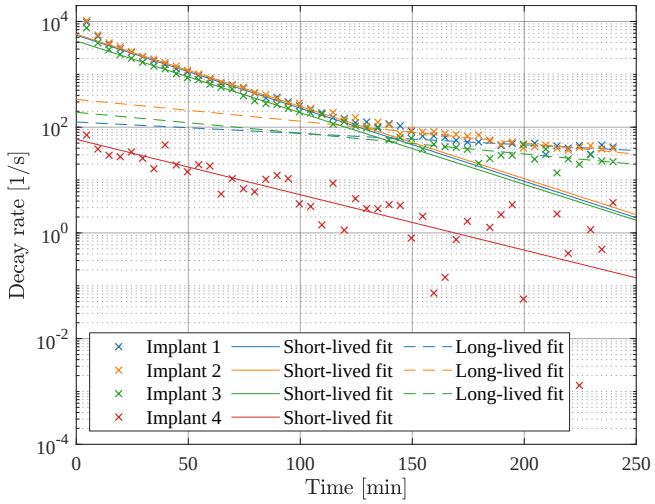

Figure A.9: Half-life analysis of the four implants in the third measurement (+3% delivered dose). A model of two (Implant 1 to 3) and a model of one (Implant 4) exponential decays is fitted to the data.

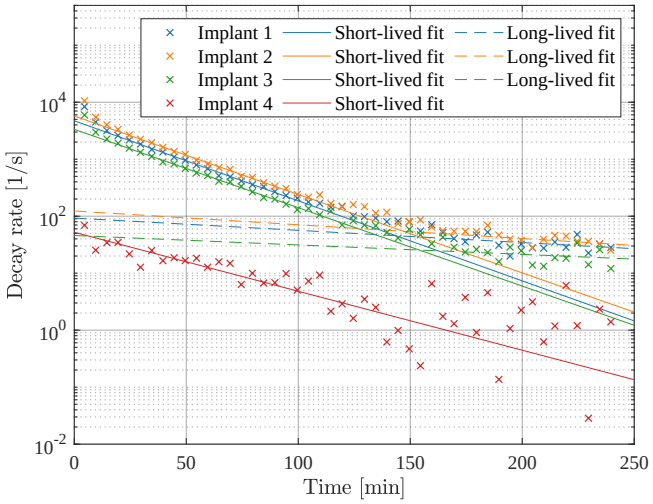

Figure A.10: Half-life analysis of the four implants in the fourth measurement (shifted by −2 mm range). A model of two (Implant 1 to 3) and a model of one (Implant 4) exponential decays is fitted to the data.

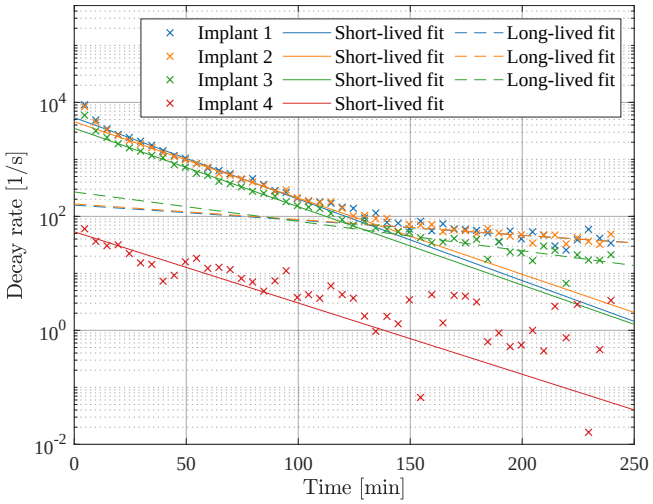

Figure A.11: Half-life analysis of the four implants in the fifth measurement (−3% delivered dose). A model of two (Implant 1 to 3) and a model of one (Implant 4) exponential decays is fitted to the data.

B List of Publications

B.1 Journal articles and conference contributions

Journal articles

C. M. Bäcker et al. "Evaluation of the activation of brass apertures in proton therapy using gamma-ray spectrometry and Monte Carlo simulations". In: *Journal of Radiological Protection*40 (2020), p. 848, doi:10.1088/1361-6498/ab9f42

S. España, ... , C. M. Bäcker, et al. "Direct proton range verification using oxygen-18 enriched water as a contrast agent". In: *Radiation Physics and Chemistry* 182 (2021) p. 109385, doi:10.1016/j.radphyschem.2021.109385

C. M. Bäcker et al. "Towards using secondary gamma-rays from proton-induced radioactivation of titanium implants for off-line field verification". In: *Nuclear Instruments and Methods in Physics Research B* 492 (2021), pp. 56 – 63, doi:10.1016/j.nimb.2021.02.006

C. M. Bäcker et al. "Experimental consolidation and absolute measurement of the $^{nat}C(p,x)^{11}C$ nuclear activation cross section at 100 MeV for particle therapy physics". In: *European Physical Journal A* 57 (2021), doi:10.1140/epja/s10050-021-00557-x

C. Bäumer, C. M. Bäcker, et al. "Can a TOF-PET photon attenuation reconstruction test stopping power estimations in proton therapy? A phantom study". In: *Physics in Medicine and Biology* 66 (2021), p. 215010, doi:10.1088/1361-6560/ac27b5

M. T. Rodriguez Gonzales, ..., C. M. Bäcker et al. "Measurement of the production cross section of β^+ emitters for range verification in proton therapy". *Applied Nuclear Physics Conference*, Prague, Czech 2021 (Talk). Proceedings submitted to EPJ Web of Conferences.

Conference contributions

C. M. Bäcker et al. "Activation of Titanium Samples in Proton Therapy". *DPG Spring Meeting*, Regensburg 2019 (Talk).

C. M. Bäcker et al. “Proton Beam Range Verification with Secondary Radiation from Titanium Implants”, Manchester 2019 (Poster). doi:10.1109/NSS/MIC42101.2019.9059997

C. M. Bäcker et al. “Development of proton range verification by use of titanium implants and PET”. *International Conference on Advances in Radiation Oncology (ICARO3)*, Vienna, Austria (virtual) 2021 (Poster).

C. M. Bäcker et al. “Consolidation and absolute measurement of the ^{12}C(p,pn)^{11}C-cross section for particle therapy”. *virtual DPG Spring Meeting*, Dortmund 2021 (Talk).

C. M. Bäcker “Masterclass: Hadronentherapie”. *Forschung trifft Schule: CERN Summer School, Lehrerfortbildung*, CERN (online) 2021 (Talk/Hands-on Session).

B.2 Supervised and co-supervised theses

A. Bley. “Bestimmung von Aktivierungswirkungsquerschnitten einer Titanprobe mittels Gammaspektrometrie nach Aktivierung in der Protonenstrahltherapie”. Bachelor Thesis. Dortmund: TU Dortmund University, 2019.

F. A. Spiecker. “Entwicklung von Phantomen und Untersuchung der Aktivierung von Titanimplantaten in der Protonentherapie zur Bestrahlungsplanverifikation mittels PET Bildgebung”. Master Thesis. Dortmund: TU Dortmund University, 2021.

E. N. Sacan. “Simulation der Neutronendosis durch Rückstreuung von der Gantry-Mechanik bei Protonentherapie”. Bachelor Thesis. Dortmund: TU Dortmund University, 2021.

Acronyms

ADC	analog digital converter
AP	annihilation peak
BPE	boron-loaded polyethylene
CCD	charge-coupled device
COBRA	Cadmium Zinc Telluride 0-Neutrino Double-Beta Research Apparatus
CT	X-ray computed tomography
CTV	clinical target volume
DEP	double escape peak
DLB	Dortmund Low Background Facility
DNA	deoxyribonucleic acid
DS	double scattering
DVH	dose volume histogram
EXFOR	EXchange FORmat for experimental numerical nuclear reaction data
FBTR	fixed-beam treatment room
FC	Faraday cup
FDG	fluorodeoxyglucose
FEP	full energy peak
GDML	Geometry Description Markup Language
GTR	gantry treatment room
HPGe	high-purity germanium
IAEA	International Atomic Energy Agency
IC	ionization chamber

LET linear energy transfer

LOR line of response

MC Monte-Carlo

MCA multi-channel analyzer

MLEM maximum likelihood expectation maximization

MRI magnetic resonance imaging

MU monitor unit

OAR organ at risk

OSEM ordered subset expectation maximization

PBS pencil beam scanning

PET positron emission tomography

PMMA polymethyl methacrylate

PSF point spread function

PTV planning target volume

PUR pile-up rejection

RBE relative biological effectiveness

RF radio-frequency

RS range shifter

SEP single escape peak

SiPM silicon photomultiplier

SOBP spread-out Bragg peak

ToF time of flight

TPS treatment planning system

US uniform scanning

VOI volume of interest

WET water equivalent thickness

WPE West German Proton Therapy Centre Essen

Bibliography

[1] C. A. Tobias et al. “Pituitary Irradiation with High-Energy Proton Beams A Preliminary Report”. In: *Cancer Research* 18.2 (1958), pp. 121–134. URL: https://cancerres.aacrjournals.org/content/18/2/121.

[2] M. Jermann. “Particle Therapy Statistics in 2014”. In: *International Journal of Particle Therapy* 2.1 (2015), pp. 50–54. DOI: 10.14338/IJPT-15-00013.

[3] M. Monteabbed, S. Espana, and H. Paganetti. “Monte Carlo patient study on te comparison of prompt gamma and PET imaging for range verification in proton therapy”. In: *Physics in Medicine & Biology* 56 (2011), pp. 1063–1082. DOI: 10.1088/0031-9155/56/4/012.

[4] A.-C. Knopf and A. Lomax. “In vivo proton range verification: a review”. In: *Physics in Medicine & Biology* 58.15 (2013), R131–R160. DOI: 10.1088/0031-9155/58/15/R131.

[5] H.-M. Lu. “A point dose method for in vivo range verification in proton therapy”. In: *Physics in Medicine & Biology* 53.23 (2008), N415–N422. DOI: 10.1088/0031-9155/53/23/n01.

[6] *ICRU Report 78: Prescribing, Recording, and Reporting Proton-Beam Therapy.* Oxford University Press, 2007. DOI: 10.1093/jicru/ndn001.

[7] C. Richter et al. “First clinical application of prompt gamma based in vivo proton range verification system”. In: *Radiotherapy and Oncology* 118 (2016), pp. 232–237. DOI: 10.1016/j.radonc.2016.01.004.

[8] K. Parodi, T. Bortfeld, and T. Haberer. “Comparison between in-beam and offline positron emission tomography imaging of proton and carbon ion therapeutic irradiation at synchrotron- and cyclotron-based facilities”. In: *International Journal of Radiation Oncology * Biology * Physics* 71.3 (2008), pp. 945–956. DOI: 10.1016/j.ijrobp.2008.02.033.

[9] C. H. Min et al. “Clinical Applications of In-Room Positron Emission Tomography for In Vivo Treatment Monitoring in Proton Radiation Therapy”. In: *International Journal of Radiation Oncology * Biology * Physics* 86.1 (2013), pp. 183–189. DOI: 10.1016/j.ijrobp.2012.12.010.

[10] J. Cho et al. “Feasibility of proton-activated implantable markers for proton range verification using PET”. In: *Physics in Medicine & Biology* 58 (2013), pp. 7497–7512. DOI: 10.1088/0031-9155/58/21/7497.

[11] J. Cho et al. “Characterizing proton activated materials to develop PET-mediated proton range verification markers”. In: *Physics in Medicine & Biology* 61 (2016), N291–N310. DOI: 10.1088/0031-9155/61/11/N291.

[12] C. M. Bäcker et al. “Proton Beam Range Verification with Secondary Radiation from Titanium Implants”. In: *2019 IEEE Nuclear Science Symposium and Medical Imaging Conference (NSS/MIC)*. 2019. DOI: 10.1109/NSS/MIC42101.2019.9059997.

[13] C. M. Bäcker et al. “Towards using secondary gamma-rays from proton-induced radioactivation of titanium implants for off-line field verification”. In: *Nuclear Instruments and Methods in Physics Research Section B: Beam Interactions with Materials and Atoms* 492 (2021), pp. 56–63. DOI: j.nimb.2021.02.006.

[14] H. Paganetti. *Proton Therapy Physics*. Boca Raton: CRC Press, 2012.

[15] G. Battistoni, I. Mattei, and S. Muraro. “Nuclear physics and particle therapy”. In: *Advances in Physics: X* 1.4 (2016), pp. 661–686. DOI: 10.1080/23746149.2016.1237310.

[16] H. Bethe. “Zur Theorie des Durchgangs schneller Korpuskularstrahlen durch Materie”. In: *Annalen der Physik* 397.3 (1930), pp. 325–400. DOI: 10.1002/andp.19303970303.

[17] F. Bloch. “Zur Bremsung rasch bewegter Teilchen beim Durchgang durch Materie”. In: *Annalen der Physik* 408.3 (1933), pp. 285–320. DOI: 10.1002/andp.19334080303.

[18] H. Kolanoski and N. Wermes. *Teilchendetektoren*. 1. Auflage. Berlin: Springer-Verlag, 2016.

[19] M. J. Berger et al. *ESTAR, PSTAR, and ASTAR: Computer Programs for Calculating Stopping-Power and Range Tables for Electrons, Protons, and Helium Ions*. National Institute of Standards and Technology, Gaithersburg, MD. (version 1.2.3) accessed 7th November 2021. 2005. URL: https://physics.nist.gov/Star.

[20] K. Parodi et al. “Patient study of in vivo verification of beam delivery and range, using proton emission tomography and computed tomography imaging after proton therapy”. In: *International Journal of Radiation Oncology * Biology * Physics* 68.3 (2007), pp. 920–934. DOI: 10.1016/j.ijrobp.2007.01.063.

[21] H. Paganetti et al. "Report of the AAPM TG-256 on the relative biological effectiveness of proton beams in radiation therapy". In: *Medical Physics* 46.3 (2019), e53–e78. DOI: 10.1002/mp.13390.

[22] Y. Zhang et al. "Brain-specific RBE of Protons Based on Long-term Outcome of Patients with Nasopharyngeal Carcinoma". In: *International Journal of Radiation Oncology*Biology*Physics* 110 (2021). DOI: 10.1016/j.ijrobp.2021.02.018.

[23] P. Andreo et al. *Absorbed Dose Determination in External Beam Radiotherapy Technical Reports Series No. 398*. V.12. Vienna: INTERNATIONAL ATOMIC ENERGY AGENCY, 2006.

[24] C. M. Bäcker. "Untersuchung der $^{nat}C(p,x)^{11}C$-Anregungsfunktion für Protonenenergien von 100 bis 230 MeV mittels Gammaspektrometrie". Masterarbeit. Dortmund: Technische Universität Dortmund, 2018.

[25] J. Wullf. "Matlab Skript zur Erzeugung eines SOBP". Mit freundlicher Genehmigung.

[26] E. Pedroni et al. "The 200-MeV proton therapy project at the Paul Scherrer Institute: Conceptual design and practical realization". In: *Medical Physics* 22.1 (1995), pp. 37–53. DOI: 10.1118/1.597522.

[27] C. Bäumer et al. "Clinical Implementation of Proton Therapy Using Pencil-Beam Scanning Delivery Combined With Static Apertures". In: *Frontiers in Oncology* 11 (2021), p. 1377. DOI: 10.3389/fonc.2021.599018.

[28] M. Conti and B. Bendriem. "The new opportunities for high time resolution clinical TOF PET". In: *Clinical and Translational Imaging* 7.2 (2019), pp. 139–147. DOI: 10.1007/s40336-019-00316-5.

[29] S. Surti and J. S. Karp. "Update on latest advances in time-of-flight PET". In: *Physica Medica* 80 (2020), pp. 251–258. DOI: 10.1016/j.ejmp.2020.10.031.

[30] P. Lecoq et al. "Roadmap toward the 10 ps time-of-flight PET challenge". In: *Physics in Medicine & Biology* 65.21 (2020), 21RM01. DOI: 10.1088/1361-6560/ab9500.

[31] M. Conti and L. Eriksson. "Physics of pure and non-pure positron emitters for PET: a review and a discussion". In: *EJNMMI physics* 3.1 (2016), pp. 1–17. DOI: 10.1186/s40658-016-0144-5.

[32] C. Gianoli et al. "Regional MLEM reconstruction strategy for PET-based treatment verification in ion beam radiotherapy". In: *Physics in Medicine & Biology* 59.22 (2014), pp. 6979–6995. DOI: 10.1088/0031-9155/59/22/6979.

[33] S. H. Keller et al. “Cross-calibration of the Siemens mMR: easily acquired accurate PET phantom measurements, long-term stability and reproducibility”. In: *European Journal of Nuclear Medicine and Molecular Imaging Physics* 3.11 (2016). DOI: 10.1186/s40658-016-0146-3.

[34] C. Bäumer et al. “Measurement of absolute activation cross sections from carbon and aluminum for proton therapy”. In: *Nuclear Instruments and Methods in Physics Research B* 440 (2019), pp. 75–81. DOI: 10.1016/j.nimb.2018.11.020.

[35] N. Verbeek. “Umsetzung Faraday Cup-basierter Dosimetrie im Nadelstrahlverfahren in der Protonentherapie”. Masterarbeit. Düsseldorf: Heinrich-Heine-Universität Düsseldorf, 2017.

[36] W. Demtröder. *Experimentalphysik 4 Kern-, Teilchen- und Astrophysik*. 4. Auflage. Berlin: Springer-Verlag, 2014.

[37] National Nuclear Data Center. *information extracted from the NuDat 2 Database*. URL: http://www.nndc.bnl.gov/nudat2/.

[38] G. R. Gilmore. *Practical Gamma-ray Spectrometry*. 2. Edition. Chichester: John Wiley & Sons, Ltd, 2008.

[39] M. J. Berger et al. *XCOM: Photon Cross Sections Database*. National Institute of Standards and Technology, Gaithersburg, MD. (version 1.5) accessed 7th November 2021. 2005. URL: https://physics.nist.gov/xcom.

[40] H. Gastrich et al. “The Dortmund Low Background Facility – Low-Background gamma ray spectrometry with an artificial overburden”. In: *Applied Radiation and Isotopes* 112 (2016), pp. 165–176. DOI: 10.1016/j.apradiso.2016.03.025.

[41] A. Einstein. “Über einen die Erzeugung und Verwandlung des Lichtes betreffenden heuristischen Gesichtspunkt”. In: *Annalen der Physik* 322.6 (1905), pp. 132–148. DOI: 10.1002/andp.19053220607.

[42] A. H. Compton. “A Quantum Theory of the Scattering of X-rays by Light Elements”. In: *Physical Review* 21 (5 1923), pp. 483–502. DOI: 10.1103/PhysRev.21.483.

[43] T. Neddermann. “Material Screening by means of Low-level Gamma Ray Spectrometry with the Dortmund Low Background HPGe Facility”. Dissertation. Dortmund: Technische Universität Dortmund, 2014. DOI: 10.17877/DE290R-14449.

[44] C. Nitsch. “Completion of the Muon Veto for the Dortmund Low Background Facility and Proton Activation Measurements on Irradiated Metals from Proton Beam Therapy”. Dissertation. Dortmund: Technische Universität Dortmund, 2018. DOI: 10.17877/DE290R-19990.

[45] *The Venom Simulation Framework for COBRA*. Dresden, Dortmund, Prag, La Plata, 2006.

[46] S. Agostinelli et al. "Geant4 – a simulation toolkit". In: *Nuclear Instruments and Methods in Physics Research A* 506.3 (2003), pp. 250–303. DOI: 10.1016/S0168-9002(03)01368-8.

[47] *DIN ISO 11929 Januar 2011: Bestimmung der charakteristischen Grenzen (Erkennungsgrenze, Nachweisgrenze und Grenzen des Vertrauensbereichs) bei Messungen ionisierender Strahlung – Grundlagen und Anwendungen*. Deutsches Institut für Normung. Berlin, 2011.

[48] C. Nitsch et al. "Improvements to the muon veto of the Dortmund Low Background Facility". In: *Applied Radiation and Isotopes* 126 (2017), pp. 201–203. DOI: 10.1016/j.apradiso.2017.02.041.

[49] G. Duplâtre et al. "Inhibition and enhancement of positronium formation in aqueous solutions from the Doppler broadening of annihilation peaks". In: *The Journal of Chemical Physics* 72.1 (1980), pp. 89–98. DOI: 10.1063/1.438958.

[50] K. Shizuma. "Analyses of monochromatic gamma-ray and annihilation radiation spectra obtained with Ge(Li) detectors". In: *Nuclear Instruments and Methods* 150.3 (1978), pp. 447–458. DOI: 10.1016/0029-554X(78)90112-X.

[51] H. Rullkötter. "Gammaspektroskopische Vermessung einer Na-22-Probe und Monte Carlo Simulationsstudien zur Abschirmung eines Germaniumdetektors". Masterarbeit. Dortmund: Technische Universität Dortmund, 2018.

[52] R. Chytracek et al. "Geometry Description Markup Language for Physics Simulation and Analysis Applications". In: *IEEE Transactions on Nuclear Science* 53.5 (2006), pp. 2892–2896. DOI: 10.1109/TNS.2006.881062.

[53] R. L. Aamodt, V. Peterson, and R. Phillips. "C^{12}(p,pn)C^{11} cross section from threshold to 340 MeV". In: *Physical Review* 88.4 (1952), pp. 739–744. DOI: 10.1103/PhysRev.88.739.

[54] N. M. Hintz and N. F. Ramsey. "Excitation Functions to 100 MeV". In: *Physical Review* 88.1 (1952), pp. 19–27. DOI: 10.1103/PhysRev.88.19.

[55] C. Brun, M. Lefort, and X. Tarrago. "Détermination des intensités de faisceaux de protons de 40 à 150 MeV". In: *Journal de Physique et le Radium* 23.6 (1962), pp. 371–376. DOI: 10.1051/jphysrad:01962002306037100.

[56] N. Otuka et al. "Towards a More Complete and Accurate Experimental Nuclear Reaction Data Library (EXFOR): International Collaboration Between Nuclear Reaction Data Centres (NRDC)". In: *Nuclear Data Sheets* 120 (2014), pp. 272–276. DOI: 10.1016/j.nds.2014.07.065.

[57] K. Kettern et al. “Formation of short-lived positron emitters in reactions of protons of energies up to 200 MeV with the target elements carbon, nitrogen and oxygen”. In: *Applied Radiation and Isotopes* 60.6 (2004), pp. 939–945. DOI: 10.1016/j.apradiso.2004.02.007.

[58] C. M. Bäcker et al. “Measurement of nuclear activation cross section of protons on natural carbon for proton beam energies between 100 and 220 MeV”. In: *Nuclear Instruments and Methods in Physics Research B* 454 (2019), pp. 50–55. DOI: 10.1016/j.nimb.2019.06.011.

[59] F. Horst et al. “Measurement of PET isotope production cross sections for protons and carbon ions on carbon and oxygen targets for applications in particle therapy range verification”. In: *Physics in Medicine & Biology* 64 (2019). DOI: 10.1088/1361-6560/ab4511.

[60] D. Nichiporov. “Verification of absolute ionization chamber dosimetry in a proton beam using carbon activation measurements”. In: *Medical Physics* 30.5 (2003), pp. 972–978. DOI: 10.1118/1.1568591.

[61] C. M. Bäcker et al. “Experimental consolidation and absolute measurement of the $^{nat}C(p,x)^{11}C$ nuclear activation cross section at 100 MeV for particle therapy physics”. In: *The European Physical Journal A* 57.8 (2021), pp. 1–11. DOI: 10.1140/epja/s10050-021-00557-x.

[62] F. Kugel. “Dosimetrie kleiner Protonen-Bestrahlungsfelder”. Masterarbeit. Düsseldorf: Heinrich-Heine-Universität Düsseldorf, 2021.

[63] G. O. Sawakuchi et al. “Experimental characterization of the low-dose envelope of spot scanning proton beams”. In: *Physics in Medicine & Biology* 55.12 (2010), pp. 3467–3478. DOI: 10.1088/0031-9155/55/12/013.

[64] E. Pedroni et al. “Experimental characterization and physical modelling of the dose distribution of scanned proton pencil beams”. In: *Physics in Medicine & Biology* 50.3 (2005), pp. 541–561. DOI: 10.1088/0031-9155/50/3/011.

[65] L. Placidi et al. “Range resolution and reproducibility of a dedicated phantom for proton PBS daily quality assurance”. In: *Zeitschrift für Medizinische Physik* 28.4 (2018), pp. 310–317. DOI: 10.1016/j.zemedi.2018.02.001.

[66] L. Lin, C. G. Ainsley, and J. E. McDonough. “Experimental characterization of two-dimensional pencil beam scanning proton spot profiles”. In: *Physics in Medicine & Biology* 58 (2013), p. 6193. DOI: 10.1088/0031-9155/59/2/493.

[67] L. Lin et al. “A novel technique for measuring the low-dose envelope of pencil-beam scanning spot profiles”. In: *Physics in Medicine & Biology* 58 (2013), N171. DOI: 10.1088/0031-9155/58/12/N171.

[68] N. Verbeek et al. “Single pencil beam benchmark of a module for Monte Carlo simulation of proton transport in the PENELOPE code”. In: *Medical Physics* 48.1 (2021), pp. 456–476. DOI: https://doi.org/10.1002/mp.14598.

[69] SGL Carbon SE. “Analyseergebnis”. Persönliche Mitteilung. 2018.

[70] F. A. Spiecker. “Entwicklung von Phantomen und Untersuchung der Aktivierung von Titanimplantaten in der Protonentherapie zur Bestrahlungsplanverifikation mittels PET Bildgebung”. Masterarbeit. Dortmund: Technische Universität Dortmund, 2021.

[71] G. K. Schenter and P. Vogel. “A Simple Approximation of the Fermi Function in Nuclear Beta Decay”. In: *Nuclear Science and Engineering* 83.3 (1983), pp. 393–396. DOI: 10.13182/NSE83-A17574.

[72] C. Winterhalter et al. “Faraday cup for commissioning and quality assurance for proton pencil beam scanning beams at conventional and ultra-high dose rates”. In: *Physics in Medicine & Biology* 66.12 (2021), p. 124001. DOI: 10.1088/1361-6560/abfbf2. URL: https://doi.org/10.1088/1361-6560/abfbf2.

[73] R. Cambria et al. “Proton beam dosimetry: A comparison between the Faraday cup and an ionization chamber”. In: *Physics in Medicine & Biology* 42.6 (June 1997), pp. 1185–1196. DOI: 10.1088/0031-9155/42/6/014.

[74] C. Gomà et al. “Proton beam monitor chamber calibration”. In: *Physics in Medicine & Biology* 59 (2014), pp. 4961–4971. DOI: 10.1088/0031-9155/59/17/4961.

[75] B. Clasie et al. “Golden beam data for proton pencil-beam scanning”. In: *Physics in Medicine & Biology* 57.5 (2012), pp. 1147–1158. DOI: 10.1088/0031-9155/57/5/1147.

[76] F. Luoni et al. “Beam Monitor Calibration for Radiobiological Experiments With Scanned High Energy Heavy Ion Beams at FAIR”. In: *Frontiers in Physics* 8 (2020), p. 397. DOI: 10.3389/fphy.2020.568145.

[77] J. Osorio et al. “Beam monitor calibration of a synchrotron-based scanned light-ion beam delivery system”. In: *Zeitschrift für Medizinische Physik* (2020). DOI: 10.1016/j.zemedi.2020.06.005.

[78] J. Kretschmer et al. “Monte Carlo simulated beam quality and perturbation correction factors for ionization chambers in monoenergetic proton beams”. In: *Medical Physics* 47.11 (2020), pp. 5890–5905. DOI: 10.1002/mp.14499.

[79] G. Aricò et al. “Benchmarking of FLUKA production cross sections of positron emission tomography isotopes for in-vivo range verification in hadron therapy”. In: *EPJ Web Conf.* 239 (2020), p. 24001. DOI: 10.1051/epjconf/202023924001.

[80] E. Grusell et al. “Faraday cup dosimetry in a proton therapy beam without collimation”. In: *Physics in Medicine & Biology* 40.11 (1995), pp. 1831–1840. DOI: 10.1088/0031-9155/40/11/005.

[81] T. M. Kavanagh, J. K. P. Lee, and W. T. Link. “A precise measurement of the C^{11} production cross section for 98-MeV protons on carbon”. In: *Canadian Journal of Physics* 42.8 (1964), pp. 1429–1436. DOI: 10.1139/p64-130.

[82] D. F. Measday. “The ^{12}C(p,pn)^{11}C Reaction from 50 to 160 MeV”. In: *Nuclear Physics* 78.2 (1966), pp. 476–480. DOI: 10.1016/0029-5582(66)90621-3.

[83] H. Gauvin, M. Lefort, and X. Tarrago. “Émission d’hélions dans les réactions de spallation”. In: *Nuclear Physics* 39 (1962), pp. 447–463. DOI: 10.1016/0029-5582(62)90403-0.

[84] V. Kostjuchenko and D. Nichiporov. “Measurement of the ^{12}C(p,pn)^{11}C Reaction from 95 to 200 MeV”. In: *Applied Radiation and Isotopes* 44.9 (1993), pp. 1173–1175. DOI: 10.1016/0969-8043(93)90060-N.

[85] T. Rodriguez-Gonzales et al. “Preliminary results of the experimental cross sections of the long-lived β^+ emitters of interest in PET range verification in proton therapy at clinical energie.” In: *Applied Nuclear Physics Conference 2021*. 2021.

[86] K. T. Bae. “Intravenous Contrast Medium Administration and Scan Timing at CT: Considerations and Approaches”. In: *Radiology* 256.1 (2010), pp. 32–61. DOI: 10.1148/radiol.10090908.

[87] D. Sánchez-Percerisa and other. “Proposal for Experiment at WPE”. Persönliche Mitteilung. 2018.

[88] V. Vedia et al. “Performance evaluation of novel $LaBr_3$(Ce) scintillator geometries for fast-timing applications”. In: *Nuclear Instruments and Methods in Physics Research Section A* 857 (2017), pp. 98–105. DOI: 10.1016/j.nima.2017.03.030.

[89] L. J. Degroot. “Kinetic Analysis of Iodine Metabolism1”. In: *The Journal of Clinical Endocrinology & Metabolism* 26.2 (Feb. 1966), pp. 149–173. DOI: 10.1210/jcem-26-2-149.

[90] *Verwendung von Jodtabletten zur Jodblockade der Schilddrüse bei einem Notfall mit Freisetzung von radioaktivem Jod*. Strahlenschutzkommission. Bonn, 2019. URL: https://www.ssk.de/SharedDocs/Beratungsergebnisse/2018/2018-04-26Jodmerk.html.

[91] M. Gerhardt. “Laufendes Promotionsprojekt”. Technische Universität Dortmund.

[92] A. Bley. "Bestimmung von Aktivierungswirkungsquerschnitten einer Titanprobe mittels Gammaspektrometrie nach Aktivierung in der Protonenstrahltherapie". Bachelorarbeit. Dortmund: Technische Universität Dortmund, 2019.

[93] S. Kauer. "Gammaspektrometrische Untersuchung der Aktivierung von Titanproben in der Protonentherapie in Hinblick auf klinische Anwendungen und Berechnung der Aktivierungswirkungsquerschnitte". Masterarbeit. Dortmund: Technische Universität Dortmund, 2018.

[94] C. M. Bäcker et al. "Development of proton range verification by use of titanium implants and PET". In: *International Conference on Advances in Radiation Oncology (ICARO-3)*. INTERNATIONAL ATOMIC ENERGY AGENCY, 2021.

[95] C. Bäumer et al. "Comprehensive clinical commissioning and validation of the RayStation treatment planning system for proton therapy with active scanning and passive treatment techniques". In: *Physica Medica* 43 (2017), pp. 15–24. DOI: 10.1016/j.ejmp.2017.09.136.

[96] C. Bäumer et al. "Can a ToF-PET photon attenuation reconstruction test stopping power estimations in proton therapy? a phantom study". In: *Physics in Medicine & Biology* 66 (2021), p. 215010. DOI: 10.1088/1361-6560/ac27b5.

[97] J. Perl et al. "TOPAS: An innovative proton Monte Carlo platform for research and clinical applications". In: *Medical Physics* 39.11 (2012), pp. 6818–6837. DOI: 10.1118/1.4758060.

[98] J. S. Reddin et al. "Performance Evaluation of the SiPM-based Siemens Biograph Vision PET/CT System". In: *2018 IEEE Nuclear Science Symposium and Medical Imaging Conference Proceedings (NSS/MIC)*. 2018, pp. 1–5. DOI: 10.1109/NSSMIC.2018.8824710.

[99] C. Behrends et al. "Providing proton fields down to the few-MeV level at clinical pencil beam scanning facilities for radiobiological experiments". In: *Medical Physics* (2021). DOI: 10.1002/mp.15388.

[100] K. Parodi et al. "PET/CT imaging for treatment verification after proton therapy: A study with plastic phantoms and metallic implants". In: *Medical Physics* 34.2 (2007), pp. 419–435. DOI: 10.1118/1.2401042.

[101] *Charged particle cross-section database for medical radioisotope production: diagnostic radioisotopes and monitor reactions*. IAEA-TECDOC-1211. INTERNATIONAL ATOMIC ENERGY AGENCY. Vienna, 2001. URL: https://www-pub.iaea.org/MTCD/Publications/PDF/te_1211_prn.pdf.

[102] A. Azzam et al. "Excitation functions for proton-induced reactions on Te and ^{nat}Ti targets: Measurements and model calculations special relevant to the ^{128}Te(p,n)^{128}I reaction". In: *Nuclear Physics A* 999 (2020), p. 121790. DOI: 10.1016/j.nuclphysa.2020.121790.

[103] J. Červenák and O. Lebeda. "New cross-section data for proton-induced reactions on ^{nat}Ti and ^{nat}Cu with special regard to the beam monitoring". In: *Nuclear Instruments and Methods in Physics Research Section B* 480 (2020), pp. 78–97. DOI: 10.1016/j.nimb.2020.08.006.

[104] K. Zarie, N. Al-Hammad, and A. Azzam. "Experimental study of excitation functions of some proton induced reactions on ^{nat}Ti for beam monitoring purposes". In: *Radiochimica Acta* 94.12 (2006), pp. 795–799. DOI: 10.1524/ract.2006.94.12.795.

[105] P. Kopecky et al. "Excitation functions of (p, xn) reactions on ^{nat}Ti: Monitoring of bombarding proton beams". In: *Applied Radiation and Isotopes* 44.4 (1993), pp. 687–692. DOI: 10.1016/0969-8043(93)90133-U.

[106] M. U. Khandaker et al. "Investigations of the ^{nat}Ti(p,x)^{43,44m,44g,46,47,48}Sc, ^{48}V nuclear processes up to 40 MeV". In: *Applied Radiation and Isotopes* 67.7 (2009). 6th International Conference on Isotopes, pp. 1348–1354. DOI: 10.1016/j.apradiso.2009.02.030.

[107] R. Michel et al. "Proton-induced reactions on titanium with energies between 13 and 45 MeV". In: *Journal of Inorganic and Nuclear Chemistry* 40.11 (1978), pp. 1845–1851. DOI: 10.1016/0022-1902(78)80241-3.

[108] D. Fink et al. "Production of ^{41}Ca and K, Sc and V short-lived isotopes by the irradiation of Ti with 35 to 150 MeV protons: applications to solar cosmic ray studies". In: *Nuclear Instruments and Methods in Physics Research Section B* 52.3 (1990), pp. 601–607. DOI: 10.1016/0168-583X(90)90483-B.

[109] S. Parashari et al. "Excitation function of the ^{nat}Ti(p,x)^{48}V,^{47,46,44m}Sc reactions within the energy range of 10-22 MeV". In: *Nuclear Physics A* 987 (2019), pp. 128–143. DOI: 10.1016/j.nuclphysa.2019.04.009.

[110] E. Garrido et al. "New excitation functions for proton induced reactions on natural titanium, nickel and copper up to 70 MeV". In: *Nuclear Instruments and Methods in Physics Research Section B* 383 (2016), pp. 191–212. DOI: 10.1016/j.nimb.2016.07.011.

[111] T. Schiekel et al. "Nuclide production by proton-induced reactions on elements ($6 \leq Z \leq 29$) in the energy range from 200 MeV to 400 MeV". In: *Nuclear Instruments and Methods in Physics Research Section B: Beam Interactions with Materials and Atoms* 114.1 (1996), pp. 91–119. DOI: 10.1016/0168-583X(96)00145-0.

[112] R. Michel et al. "Cross sections for the production of residual nuclides by low- and medium-energy protons from the target elements C, N, O, Mg, Al, Si, Ca, Ti, V, Mn, Fe, Co, Ni, Cu, Sr, Y, Zr, Nb, Ba and Au". In: *Nuclear Instruments and Methods in Physics Research Section B: Beam Interactions with Materials and Atoms* 129.2 (1997), pp. 153–193. DOI: 10.1016/S0168-583X(97)00213-9.

[113] R. Michel and G. Brinkmann. "On the depth-dependent production of radionuclides (44 A 59) by solar protons in extraterrestrial matter". In: *Journal of Radioanalytical and Nuclear Chemistry* 59.2 (1980), pp. 467–510. DOI: 10.1007/BF02517298.

[114] R. Michel, F. Peiffer, and R. Stück. "Measurement and hybrid model analysis of integral excitation functions for proton-induced reactions on vanadium, manganese and cobalt up to 200 MeV". In: *Nuclear Physics A* 441.4 (1985), pp. 617–639. DOI: 10.1016/0375-9474(85)90441-5.

[115] S. Neumann. "Aktivierungsexperimente mit Neutronen mittlerer Energien und die Produktion kosmogener Nuklide in extraterrestrischer Materie". Dissertation. Hanover: Universität Hannover, 1999. URL: https://edocs.tib.eu/files/e002/267375484.pdf.

[116] S. R. Kennett et al. "Cross-section measurements and thermonuclear reaction rates for ^{46}Ti(p,γ)^{47}V, ^{47}Ti(p,γ)^{48}V, ^{47}Ti(p,n)^{47}V and ^{48}Ti(p,γ)^{49}V". In: *Nuclear Physics A* 368.2 (1981), pp. 337–351. DOI: 10.1016/0375-9474(81)90689-8.

[117] H. Taketani and W. P. Alford. "(p, n) Cross Sections on Ti^{47}, V^{51}, Cr^{52}, Co^{59}, and Cu^{63} from 4 to 6.5 Mev". In: *Physical Review* 125 (1 1962), pp. 291–294. DOI: 10.1103/PhysRev.125.291.

[118] S. Tanaka and M. Furukawa. "Excitation Functions for (p, n) Reactions with Titanium, Vanadium, Chromium, Iron and Nickel up to Ep=14 MeV". In: *Journal of the Physical Society of Japan* 14.10 (1959), pp. 1269–1275. DOI: 10.1143/JPSJ.14.1269.

[119] E. Gadioli et al. "Emission of alpha particles in the interaction of 10–85 MeV protons with ^{48,50}Ti". In: *Zeitschrift für Physik A Atoms and Nuclei* 301.4 (1981), pp. 289–300. DOI: 10.1007/BF01421692.

[120] M. Rios, B. D. Anderson, and J. S. Schweitzer. "The ^{46}Ti(p,γ)^{47}V, ^{50}Cr(p,γ)^{51}Mn, ^{58}Ni(α,γ)^{62}Zn and ^{58}Ni(α,p)^{61}Cu cross sections". In: *Nuclear Physics A* 236.2 (1974), pp. 523–532. DOI: 10.1016/0375-9474(74)90271-1.

[121] V. N. Levkovski. *Middle mass nuclides (A=40-100) activation cross-sections by medium energy (E=10-50 MeV) protons and a particles (experiments and systematics)*. Moscow: Inter-Vesi, 1991.

[122] M. E. Bennett et al. "Measurement of the ^{nat}Lu(p,x)^{175}Hf excitation function". In: *Nuclear Instruments and Methods in Physics Research Section B: Beam Interactions with Materials and Atoms* 276 (2012), pp. 62–65. DOI: 10.1016/j.nimb.2012.01.039.

[123] S. Takács et al. "New cross-sections and intercomparison of proton monitor reactions on Ti, Ni and Cu". In: *Nuclear Instruments and Methods in Physics Research Section B: Beam Interactions with Materials and Atoms* 188.1 (2002), pp. 106–111. DOI: 10.1016/S0168-583X(01)01032-1.

[124] P. Jung. "Cross Sections for the Production of Helium and Long-Living Radioactive Isotopes by Protons and Deuterons". In: *Nuclear Data for Science and Technology*. Ed. by Syed M. Qaim. Berlin, Heidelberg: Springer, 1992, pp. 352–354. ISBN: 978-3-642-58113-7.

[125] F. Tárkányi, F. Szelecsényi, and P. Kopecký. "Cross Section Data for Proton, ^{3}He and α-Particle Induced Reactions on ^{nat}Ni, ^{nat}Cu and ^{nat}Ti for Monitoring Beam Performance". In: *Nuclear Data for Science and Technology*. Ed. by Syed M. Qaim. Berlin, Heidelberg: Springer, 1992, pp. 529–532. ISBN: 978-3-642-58113-7.

[126] J. N. Barrandon et al. "Étude du dosage de Ti, V, Cr, Fe, Ni, Cu et Zn par activation avec des protons d'énergie limitée a 20 MeV". In: *Nuclear Instruments and Methods* 127.2 (1975), pp. 269–278. DOI: 10.1016/0029-554X(75)90499-1.

[127] F. Szelecsényi et al. "Excitation function for the natTi(p,x)48V nuclear process: Evaluation and new measurements for practical applications". In: *Nuclear Instruments and Methods in Physics Research Section B: Beam Interactions with Materials and Atoms* 174.1 (2001), pp. 47–64. DOI: 10.1016/S0168-583X(00)00516-4.

[128] W. Zhao et al. *Excitation functions of reactions from d + Ti, d + Mo, p + Ti and p + Mo (CNIC–01266)*. International Atomic Energy Agency. CNIC–01266, INIS Report No. 30031247. 1998. URL: https://inis.iaea.org/search/search.aspx?orig_q=RN:30031247.

Danksagung

An dieser Stelle möchte ich mich bei allen bedanken, die mich bei der Erstellung dieser Arbeit und während meines gesamten Studiums unterstützt haben oder die letzten 3 Jahre zu einer spannenden und abwechslungsreichen Zeit haben werden lassen.

Zuerst geht mein Dank an Prof. Dr. Kevin Kröninger und PD Dr. Christian Bäumer für die Betreuung dieser Arbeit und die Möglichkeit im Rahmen der gemeinsamen Kooperation diese Arbeiten durchführen zu können. Ferner haben sie mir die Beteiligung am Mercur-Graduiertenkolleg „Präzisionsprotonentherapie — Praxisbezogene Physik und Chemie an der Schnittstelle zur Medizin“ ermöglicht, sodass ich von dem interdisziplinären Austausch dort profitieren konnte und in Bereiche abseits der Physik Einblicke bekommen habe.

Mein Dank geht an Dr. Jörg Wulff und Carina Behrends für die vielen kritischen Anmerkungen zu meinen Auswertungen, wie man schöne Abbildungen erstellt und die vielen kritischen Anmerkungen zu dieser Arbeit. Bei den TOPAS Simulationen war Nico Verbeek ein kompetenter Ansprechpartner, der auf Basis seines Promotionsprojekts die TOPAS Quelle erstellen konnte und ich von seinen Messungen für präzise Ergebnisse profitieren konnte. Vielen Dank an Dr. Jens Weingarten, Florian Mentzel und Marius Hötting für die vielen hilfreichen Anmerkungen und Kritik. Mit Marcel Gerhardt habe ich die Messungen an der DLB durchgeführt. Vielen Dank, dass Du die Abende geopfert hast, und auf mich mit meinen Proben gewartet hast. Meine Masterstudentin Fleur Spiecker und mein Bachelorstudent Aaron Bley haben mit ihren individuellen Ergebnisse erheblich zum Gesamtfortschritt des Titanprojekts beigetragen. Vielen Dank, dass Ihr mir die Betreuung so einfach gemacht habt.

Bei Dr. Felix Horst, Dr. Christoph Schuy und Wihan Adi möchte ich mich für die Kooperation zur Konsolidierung des ^{11}C Wirkungsquerschnitt bedanken. Gemeinsam konnten wir hoffentlich einen Wert finden, der lange Bestand haben wird.

Further thanks to Andrija Matic, Ben Liu, Ryan Swanson, and Erik den Boer from iba PT Physics Team Essen for searching in the accelerator logs, whenever I performed experiments and needed some decay corrections.

Additionally, thanks to Dr. Daniel Sánchez Parcerisa and Teresa Rodríguez González for the nice contact during their experiments at WPE. With Daniel's team I performed the activation of CsI which then became part of my Ph.D. project.

Vielen Dank an die Klinik für Nuklearmedizin und insbesondere an Prof. Dr. Dr. Walter Jentzen und Sandra Kazek für die Unterstützung bei den Messungen am PET/CT

System im WPE. Many thanks to Mohammadreza Teimoorisichani (Siemens Healthineers) for his support with the analysis of the PET data.

Danke an das MTRA-Team am WPE und insbesondere an Sebastian Weise und Ina Rasch für die Unterstützung bei diversen klinischen Fragestellungen, seien es die passenden CT Parameter für meine Planungs-CT oder die korrekte Phantompositionierung auf dem Bestrahlungstisch.

Nicht zu vergessen sind Manuel Beck und Julian Kinne aus der mechanischen Werkstatt des WPE. Sie haben nicht nur die Phantome produziert und professionelle CAD Zeichnungen erstellt, sondern haben mich in der Werkstatt auch selbst machen lassen.

Abseits der Arbeit haben der Lehrstuhl E4 und insbesondere die gesamte Abteilung für Physik am WPE die letzten Jahre zu einer angenehmen Zeit gemacht und, auch wenn der Abend mal lang wurde, hatten wir am WPE immer viel Spaß.

Ein ganz besonderer Dank geht an Anna-Lisa Glitz („Wer ist...?“ – „Neeein!“) für die virtuelle Begleitung durch die letzten 2 Jahre Corona, für die mehr oder weniger tiefgründigen Chatverläufe und die (viel) zu langen Siedlerabende. Weiterhin möchte ich mich bei Lena Mertens für die vielen Gespräche über die Unterschiede und Gemeinsamkeiten zwischen der Protonen- und Photonentherapie bedanken.

Zuletzt möchte ich mich bei meiner Familie und insbesondere bei meinen Eltern bedanken, die mir das Studium nicht nur finanziell ermöglicht haben, sondern auch jede Menge Tippfehler und unvollständige Sätze gefunden haben. Außerdem konnte ich mir, wann immer nötig, mal ein Auto ausleihen, um zu allen Tages- und Nachtzeiten nach Essen kommen zu können.